Titre: Title:	Electromagnetic Device Modeling by Circuit-Based Methods
Auteur: Author:	Sadegh Rahimi Pordanjani
Date:	2022
Type:	Mémoire ou thèse / Dissertation or Thesis
Référence: Citation:	Rahimi Pordanjani, S. (2022). Electromagnetic Device Modeling by Circuit-Based Methods [Ph.D. thesis, Polytechnique Montréal]. PolyPublie. https://publications.polymtl.ca/10456/

URL de PolyPublie: PolyPublie URL:	https://publications.polymtl.ca/10456/
Directeurs de recherche: Advisors:	Jean Mahseredjian, Nicolas Bracikowski, & Afshin Rezaei-Zare
Programme: Program:	Génie électrique

POLYTECHNIQUE MONTRÉAL

affiliée à l’Université de Montréal

Electromagnetic device modeling by circuit-based methods

SADEGH RAHIMI PORDANJANI

Département de génie électrique

Thèse présentée en vue de l’obtention du diplôme de *Philosophiæ Doctor*

Génie électrique

Août 2022

POLYTECHNIQUE MONTRÉAL

affiliée à l’Université de Montréal

Cette thèse intitulée :

Electromagnetic device modeling by circuit-based methods

présentée par **Sadegh RAHIMI PORDANJANI**

en vue de l’obtention du diplôme de *Philosophiæ Doctor*

a été dûment acceptée par le jury d’examen constitué de :

Jérôme LE NY, président
Jean MAHSEREDJIAN, membre et directeur de recherche
Nicolas BRACIKOWSKI, membre et codirecteur de recherche
Afshin REZAEI-ZARE, membre et codirecteur de recherche
Antoine LESAGE-LANDRY, membre
Mathieu ROSSI, membre externe

DEDICATION

To my parents, my niece Negar, and my nephew Parsa.

ACKNOWLEDGEMENTS

My delight is to show my appreciation to all of the people with whom I had the privilege of working and communicating during this project:

First and foremost, I would want to convey my heartfelt gratitude to my supervisor, Prof. Jean Mahseredjian, for his support and insightful discussions.

To my co-supervisor Prof. Afshin Rezaei-Zare for his advice.

To Prof. Nicolas Bracikowski for his collaborations and knowledge, he was a great help for me.

To Mohammed Naïdjate cooperation and expertise; he was a tremendous assistance to me.

To Mircea Fratila, for the ideas and guidance he provided.

To Tarek Ould-Bachir for his meaningful discussions.

My colleagues at the department for their friendship and support. To those who already left: Hossein Chalangar, Reza Hassani, Danial Jafarigiv, Amir Sadati, Maryam Torabi, Nasim Rashidirad, Younes Seyedi, and Aboutaleb Haddadi. To those who will continue: Javad Gholinezhad, Hossein Zamani, Renan Morais Furlaneto, and others. My friends outside the department for their friendship and support: Hamid Reza Shahhosseini, Mohammad Reza Malek, Omid Salari, Mohsen Rezaei, and Sajjad Rastegar.

RÉSUMÉ

De nouvelles approches basées sur les circuits équivalents sont proposées dans cette étude pour la modélisation électromagnétique de dispositifs magnétiques, tels que les inductances et les transformateurs, dans un logiciel de type EMT (transitoire électromagnétique), comme EMTP. Les méthodes proposées présentent les avantages des méthodes basées sur les circuits électromagnétiques, et peuvent également fournir une représentation détaillée des dispositifs magnétiques comparable à celle de la méthode par éléments finis (MEF).

Les approches proposées dans cette thèse permettent une modélisation géométrique détaillée, ainsi que la visualisation de la distribution du flux magnétique et la prise en compte de la saturation du noyau de fer. Les méthodes proposées dans cette thèse peuvent être implémentées dans un logiciel de type EMT en utilisant des éléments standards. Ils peuvent servir dans un logiciel de type EMT pour voir l'effet des réseaux électriques sur les dispositifs magnétiques et inversement. Étant donné que la MEF 2D est préférée à la MEF 3D pour la plupart des applications de systèmes électriques, en raison de sa simplicité, les modèles de dispositifs magnétiques basés sur des circuits équivalents sont d’abord présentés en mode 2D. Ensuite, ils sont améliorés pour prendre en compte les effets tridimensionnels, notamment dans les cas où les flux de fuite dans la troisième dimension sont cruciaux pour la précision du modèle.

Des modèles pour des inductances et des transformateurs avec des structures à plusieurs enroulements peuvent être générés à l'aide de la méthode proposée. En outre, la méthode proposée peut représenter les défauts internes des inductances et des transformateurs. Afin de vérifier l'approche proposée, les résultats des modèles obtenus sont comparés aux résultats des modèles MEF 2D et 3D. Une précision comparable est obtenue pour les modèles 2D et 3D.

Les méthodes proposées dans cette thèse peuvent être utilisées pour intégrer la modélisation MEF dans des outils de type EMT, notamment la représentation précise de la géométrie, la prise en compte de la saturation du noyau de fer et la prise en compte de tous les chemins de flux magnétique, y compris les chemins de flux de fuite à travers l'air.

ABSTRACT

New circuit-based approaches are proposed in this study for the electromagnetic modelling of magnetic devices, such as inductors and transformers, in electromagnetic transient (EMT)-type software (EMTP, for example). The proposed methods have the advantages of circuit-based methods, and they can also provide a detailed representation of magnetic devices comparable to that of the finite element method (FEM).

The proposed approaches enable detailed geometrical modelling, as well as visualisation of magnetic flux distribution and consideration of iron core saturation. The methods proposed in this thesis can be implemented in EMT-type software using standard elements. They can be implemented in EMT-type software to see the effect of power networks on magnetic devices and vice-versa. Given the difficulty of 3D FEM and the fact that 2D FEM is preferred over 3D FEM for most power system applications, due to its simplicity, circuit-based magnetic device models are first presented in 2D. Afterwards, they are improved to take into account three-dimensional effects, particularly in cases where the leakage fluxes in the third dimension are crucial to model's accuracy.

Models for inductors and transformers with multi-winding structures can be generated using the proposed method. In addition, the proposed method can represent internal faults in inductors and transformers. In order to verify the proposed approach, the findings of the resulting 2D and 3D circuit-based models are compared to the results of the 2D and 3D FEM models, respectively. High accuracy is achieved for both 2D and 3D models. Finally, it can be stated that the methods proposed in this thesis can be used to integrate features of 2D and 3D FEM modelling into EMT-type software, including accurate geometry modelling, consideration of iron core saturation, and consideration of all magnetic flux paths, including leakage flux paths through air during saturated operation.

TABLE OF CONTENTS

DEDICATION III

ACKNOWLEDGEMENTS IV

RÉSUMÉ V

ABSTRACT VI

TABLE OF CONTENTS VII

LIST OF TABLES X

LIST OF FIGURES XI

CHAPTER 1 INTRODUCTION 1

- 1.1 Connection between magnetic and electric circuits 1
  - 1.1.1 Hopkinson Analogy 1
  - 1.1.2 Buntenbach Analogy 4
  - 1.1.3 Duality principle 6
  - 1.1.4 Derivation duality circuit from Hopkinson and Buntenbach analogies 8
- 1.2 Literature review 11
  - 1.2.1 Coupled problems for modelling magnetic devices in power systems 11
  - 1.2.2 Existing lumped circuit-based models for modeling magnetic devices 12
- 1.3 Dissertation statement 26
  - 1.3.1 Problem definition 26
  - 1.3.2 Objectives 26
- 1.4 Dissertation outline 27

CHAPTER 2 INDUCTOR MODEL BY DISTRIBUTED CIRCUIT-BASED METHODS . 29

- 2.1 Methodology 30
  - 2.1.1 Electromagnetic modeling by Hopkinson Analogy 30

2.1.2 Electromagnetic modeling by Buntenbach Analogy....34

2.1.3 Electromagnetic modeling by duality principle....35

2.2 Validation....38

2.3 Conclusion....51

CHAPTER 3 TRANSFORMER MODEL BY DISTRIBUTED CIRCUIT-BASED METHODS…… 53

3.1 Methodology....55

3.1.1 Hopkinson Analogy....57

3.1.2 Buntenbach Analogy....59

3.1.3 Duality principle....60

3.2 Distributed reluctance network model for a three-phase transformer....61

3.2.1 Meshing and indexing....62

3.2.2 Determination of circuit parameters....66

3.2.3 Connection of model elements....66

3.3 Study of internal faults using HBD-circuits....69

3.3.1 Element definition....70

3.3.2 Determination of circuit parameters....76

3.3.3 Connection of model elements....77

3.4 Results and validation....78

3.5 Conclusion....91

CHAPTER 4 DOUBLE-2D DISTRIBUTED CIRCUIT-BASED METHODS....93

4.1 Introduction to 3D methods....93

4.1.1 Motivation....93

4.1.2 Double-2D concept....94

4.2 Explanation of the double 2D methodology 95

4.2.1 Meshing 97

4.2.2 Determination of circuit parameters 100

4.2.3 Connection of model elements 103

4.3 Leakage inductance calculation by double-2D circuit-based method 109

4.3.1 Comparison of analytical and double-2D circuit-based models of transformer leakage inductance 110

4.4 Double-2D circuit-based model for three phase transformers 121

4.4.1 Division of 3D structure into 2D sections 121

4.4.2 Connection of 2D models 122

4.4.3 Validation 123

4.5 Conclusion 125

CHAPTER 5 CONCLUSION 127

5.1 Summary 127

5.2 Future works 129

REFERENCES 130

LIST OF TABLES

Table 1.1 Summary of transformer models..25

Table 2.1 Piecewise-linear curve (first quadrant) presenting soft iron. 42

Table 2.2 Accuracy analysis for HBD-circuits (FEM results are reference.) 49

Table 3.1 Specifications of transformer 79

Table 3.2 Design and geometrical parameters of transformer 79

Table 3.3 Accuracy Analysis for HBD-circuits for open-circuit condition in both linear and saturated operating points, FEM is the reference. 81

Table 3.4 Accuracy analysis for HBD-circuits for short-circuit condition, FEM is the reference 83

Table 3.5 Accuracy analysis for HBD-circuits for local point representation, FEM is the reference 85

Table 3.6 Accuracy analysis for HBD-circuits in representing energization transients, FEM is the reference. 88

Table 3.7 Accuracy Analysis for HBD-circuits for representing faults, FEM is the reference. ...91

Table 4.1 Comparison of the accuracy of the proposed model to that of analytical and FEM models 119

Table 4.2 Parameters of considered transformers, see Figure 4.13 for parameter definitions [78] 119

Table 4.3 Error derived by Hopkinson Single-2D, FEM 2D, and Hopkinson Double-2D for open-circuit and short-circuit conditions...125

LIST OF FIGURES

Figure 1.1 Hopkinsons' analog of the iron core inductor 2

Figure 1.2 Type-2 L-R mutator 3

Figure 1.3 Buntenbach's analog of the iron core inductor 5

Figure 1.4 Type 1 L-C mutator 5

Figure 1.5 Derivation of a dual circuit for an iron core inductor using duality transformation 8

Figure 1.6 Simple circuit based on Buntenbach analogy 9

Figure 1.7 Equivalent circuits demonstrating the conversion of a permeance into an inductor by adding an L-C mutator 9

Figure 1.8 The circuit equivalent to Figure 1.6 resulted from replacing the permeance with its dual circuit 10

Figure 1.9 Conversion of two series-connected mutators into an ideal transformer 10

Figure 1.10 Duality-derived circuit equivalent to the circuit in Figure 1.6 11

Figure 1.11 STC representation of single-phase two-winding transformer [35] 14

Figure 1.12 STC representation of single-phase N-winding transformer [35] 14

Figure 1.13 Representation of two-winding transformer with an externally attached core, based on the BCTRAN model 16

Figure 1.14 Magnetic flux paths assumed by UMEC for the three-legged two-winding transformer 17

Figure 1.15 Magnetic circuit of UMEC model for the two-winding three-legged transformer shown in Figure 1.14 18

Figure 1.16 Magnetic flux paths assumed by TOPMAG for the three-legged two-winding transformer with concentric windings 19

Figure 1.17 Magnetic equivalent circuit of TOPMAG model for the two-winding three-legged transformer shown in Figure 1.16 20

Figure 1.18 Duality derived transformer model based on the TOPMAG model for the transformer shown in Figure 1.16 20

Figure 1.19 Magnetic flux paths assumed by hybrid model for the three-legged two-winding transformer with concentric windings 22

Figure 1.20 Magnetic equivalent circuit of hybrid model for the two-winding three-legged transformer shown in Figure 1.19 22

Figure 1.21 Hybrid transformer model for a three-legged transformer 22

Figure 2.1 (a) Distributed magnetic circuit with magnetomotive forces, (b) schematic of inductor winding turns and external circuit 32

Figure 2.2 Circuit of the elementary cell in Hopkinson analogy 33

Figure 2.3 Distributed inductor model using Hopkinson analogy (including both magnetic and electric circuits and coupling between them) 34

Figure 2.4 Distributed inductor model using Buntenbach analogy (including both magnetic and electric circuits and coupling between them) 35

Figure 2.5 Graphical derivation of the dual circuit of the magnetic circuit for three types of cells, excluding coupling elements 36

Figure 2.6 Graphical derivation of the dual circuit of the magnetic circuit for one type of cell, including coupling elements 37

Figure 2.7 Distributed duality-based inductor model, including both magnetic and electric circuits and coupling between them 38

Figure 2.8 Cross-section of the gapped inductor 39

Figure 2.9 Cross-section of left half of the inductor 40

Figure 2.10 Distributed resistive, capacitive, and inductive circuits regarding three sample cells of the meshed inductor model shown in Figure 2.9 41

Figure 2.11 Nonuniform cell 43

Figure 2.12 Gapless core inductor current i for HBD-circuits (1152 meshes) and FEM (3778 elements), during the nonlinear condition 44

Figure 2.13 Gapped core inductor current i for HBD-circuits (1152 meshes) and FEM (3778 meshes) during the nonlinear condition 45

Figure 2.14 Magnetic field intensity H regarding a point of the gapless core with coordinates $0.02m, 0.06m$ during magnetic local saturation 46

Figure 2.15 Magnetic field intensity H regarding a point of gapped core with coordinates $0.02m, 0.06m$ during magnetic local saturation 46

Figure 2.16 Voltage-current characteristics viewed from the terminals of the gapless core inductor (HBD-circuits with 72 meshes)..47

Figure 2.17 Voltage-current characteristics viewed from the terminals of the gapless core inductor (HBD-circuits with 1152)..47

Figure 2.18 Voltage-current characteristics viewed from the terminals of the gapped core inductor (HBD-circuits with 72 meshes)..48

Figure 2.19 Voltage-current characteristics viewed from the terminals of the gapped core inductor (HBD-circuits with 1152 meshes)...48

Figure 2.20 HBD-circuits vs. FEM in terms of computation time..50

Figure 2.21 Inductor Current modeled by HBD-circuits and FEM during ferroresonance 51

Figure 3.1 (a) Distributed magnetic circuit with magnetomotive forces, (b) schematic of transformer winding turns and external circuit 56

Figure 3.2 DRNM for a transformer (magnetic and electric circuits, as well as their coupling)...57

Figure 3.3 Distributed transformer model using Buntenbach analogy, including both magnetic and electric circuits and coupling between them 60

Figure 3.4 Distributed duality-based transformer model, including both magnetic and electric circuits and coupling between them 61

Figure 3.5 Schematic of a three-phase three-legged core-type transformer 62

Figure 3.6 Cross-section of left half of the core 64

Figure 3.7 Circuits based on Hopkinson Analogy for four cell types (A, B, C, and D) 64

Figure 3.8 Circuits based on Hopkinson Analogy for four cell types (A, B, C, and D) 65

Figure 3.9 Circuits based on Duality principle for four cell types (A, B, C, and D) 65

Figure 3.10 Meshes generated for a portion of a faulty transformer with a fault in the middle column's HV winding, (a) Turn to earth fault, (b) Turn to turn fault 70

Figure 3.11 Circuits based on Hopkinson Analogy for three cell types (B_1, B_2 C_1) related to the mesh generated in Figure 3.10(a) 71

Figure 3.12 Circuits based on Buntenbach Analogy for three cell types (B1, B2, and C1) related to the mesh generated in Figure 3.10(a) 72

Figure 3.13 Circuits based on Duality principle for three cell types (B_1, B_2 C_1) related to the mesh generated in Figure 3.10(a) 73

Figure 3.14 Circuits based on Hopkinson Analogy for four cell types (B_1, B_2 B_3, C_2) related to the mesh generated in Figure 3.10(b) 74

Figure 3.15 Circuits based on Buntenbach Analogy for four cell types (B_1, B_2 B_3, C_2) related to the mesh generated in Figure 3.10(b) 75

Figure 3.16 Circuits based on Duality principle for four cell types (B_1, B_2 B_3, C_2) related to the mesh generated in Figure 3.10(b) 76

Figure 3.17 Convergence of a global metric (blue) and a local metric (red) 80

Figure 3.18 Circuit for open-circuit test, transformer with Y-Delta connection 80

Figure 3.19 V-I characteristic for open-circuit test 80

Figure 3.20 Primary winding current of phase-a, open-circuit 81

Figure 3.21 Primary winding current of phase-b, open-circuit 82

Figure 3.22 Primary winding current of phase-c, open-circuit 82

Figure 3.23 Circuit for short-circuit test, transformer with Y-Delta connection 83

Figure 3.24 V-I characteristic while short-circuiting the secondary side 83

Figure 3.25 Primary winding current in phase-a, during short-circuit..84

Figure 3.26 Primary winding current in phase-b, during short-circuit..84

Figure 3.27 Primary winding current in phase-c, during short-circuit..84

Figure 3.28 Magnetic flux B regarding a point of gap between the windings of phase A............85

Figure 3.29 Flux distribution for short-circuit condition derived by Hopkinson Analogy 86

Figure 3.30 Flux distribution for short-circuit condition derived by Buntenbach Analogy 86

Figure 3.31 Flux distribution for short-circuit condition derived by Duality principle 87

Figure 3.32 Circuit for transformer energization, Y-Delta connection...87

Figure 3.33 Inrush currents, solved with HBD-circuits and FEM 88

Figure 3.34 Current of healthy part of HV winding during an inter-turn fault 89

Figure 3.35 Current of faulty part of HV winding during an inter-turn fault 89

Figure 3.36 Current of secondary winding during an inter-turn fault...90

Figure 3.37 Per unit current of the affected winding for different fault resistances 90

Figure 3.38 HBD-circuits vs. FEM in terms of computation time..91

Figure 4.1 V-I characteristic for open-circuit achieved by Hopkinson 2D model, FEM 2D, and FEM 3D...94

Figure 4.2 V-I characteristic while short-circuiting the secondary side achieved by Hopkinson 2D model, FEM 2D, and FEM 3D 94

Figure 4.3 Study of transformer with 3D EE structure by means of double 2D. (a) 3D EE structure, (b) Division of the windings, (c) 2D simulations related to the divided parts 96

Figure 4.4 Cross sections of “Double-2D” model for a single-phase transformer (a) Inside window (IW). (b) Outside window (OW)...97

Figure 4.5 Cross-section of left half of the core on IW plane...97

Figure 4.6 Cross-section of left half of the core on OW plane (y-z)...98

Figure 4.7 Circuits based on Hopkinson Analogy for four cell types (A, B, C, and D) related to mesh of IW cross section shown in Figure 4.5 99

Figure 4.8 Circuits based on Hopkinson Analogy for four cell types (A, B, C, and D) related to mesh of OW cross section shown in Figure 4.6 100

Figure 4.9 The depths of the magnetic flux paths for IW and OW models ($depthijIW$, $depthijOW$) 102

Figure 4.10 Diagram of double 2D model, electrical connections...109

Figure 4.11 Diagram of double 2D model to calculate leakage inductance observed from HV side 110

Figure 4.12 Definition of geometrical parameters of single-phase transformer [78]..................111

Figure 4.13 Definition of geometrical parameters of single-phase transformer 113

Figure 4.14 Transformer window with two winding layers: the original and an image one 116

Figure 4.15 The method of image applied to the OW cross section. (a) Actual OW cross-section that isn't suited the method of images. (b) Assumed OW cross-section that is suited the method of images. (c) Mathematical equivalent of (b) using the method of images 118

Figure 4.16 Division of a three-phase three-legged transformer into four 2D sections...............122

Figure 4.17 Diagram of double 2D model for three phase transformer with star-delta connection 123

Figure 4.18 V-I characteristic for open-circuit achieved by Hopkinson Single-2D model, FEM 2D, Hopkinson Double-2D model, and FEM 3D 124

Figure 4.19 V-I characteristic while short-circuiting the secondary side achieved by Hopkinson Single-2D model, FEM 2D, Hopkinson Double-2D model, and FEM 3D 125

LIST OF SYMBOLS AND ABBREVIATIONS

DC	Direct Current
EMF	Electromotive Force
EMT	Electromagnetic Transients
EMTP	ElectroMagnetic Transients Program
ES	ElectroStatics
FEM	Finite Element Method
HV	High Voltage
LV	Low Voltage
MEC	Magnetic Equivalent Circuit
MMF	Magnetomotive Force
MQS	MagnetoQuasiStatics
MS	MagnetoStatics
RNM	Reluctance Network Model
RMS	Root Mean Square
RMSE	Root Mean Square Error
STC	Saturable Transformer Component
UMEC	Unified Magnetic Equivalent Circuit
IW	Inside Window
OW	Outside Window
MTL	Mean Turn Length

CHAPTER 1 INTRODUCTION

Power system transients can be significantly influenced by the nonlinear and frequency-dependent behaviour of magnetic devices, such as inductors, transformers, electric machines, which are widely used in transmission and distribution grids. Accurate models of magnetic device are necessary to conduct an effective risk assessment and network optimization. Magnetic device manufacturers require realistic models that not only accurately describe magnetic devices but also allow them to observe the different effects of network on the internal behaviour of magnetic devices.

The use of circuit-based models for the accurate modelling of transformers and inductors in EMT-type software tools is the primary focus of this thesis. The first thing that will be covered in this chapter is an explanation of all of the methods that may be used to represent magnetic devices using equivalent electric circuit.

1.1 Connection between magnetic and electric circuits

The lumped circuit-based models used in this thesis derive equivalent circuits based on three different approaches: Hopkinson analogy [1, 2], Buntenbach analogy [3], and the duality principle [4-7] named hereinafter, HBD-circuits. The Hopkinson analogy, often known as the resistance-reluctance analogy, is the oldest and most widely used approach. However, in some cases, this method has limitations, and the Buntenbach analogy and duality principle are favored. For example, the duality principle, which employs electric elements to implement magnetic devices, is the method of choice in topological transformer models [6], [7] used in EMT-type software. Also, the Buntenbach analogy, or permeance-capacitance analogy, has lately been utilized to model magnetic devices in power electronic circuits [8], [9]. In this part, their advantages and disadvantages, as well as their modelling applications for magnetic devices, are reviewed in great detail.

1.1.1 Hopkinson Analogy

Hopkinson’s analogy [1, 2] is the earliest method for establishing a link between magnetic and electric circuits. The magnetic scalar law, which is equivalent to Ohm's law in electric circuits, is the basis of this analogy.

$$\mathcal{F} = R\,\phi \tag{1.1}$$

where $\mathcal{F}$, R, and ϕ are, respectively, the magnetomotive force MMF, the reluctance, and the magnetic flux. In this method, resistors are used to represent the reluctances. And voltage sources and current sources in equivalent circuit are used to represent magnetomotive forces sources and magnetic fluxes sources in magnetic circuit, respectively [1, 2]. To illustrate this analogy, Figure 1.1 illustrates the Hopkinsons' analog circuit for the case of an inductor.

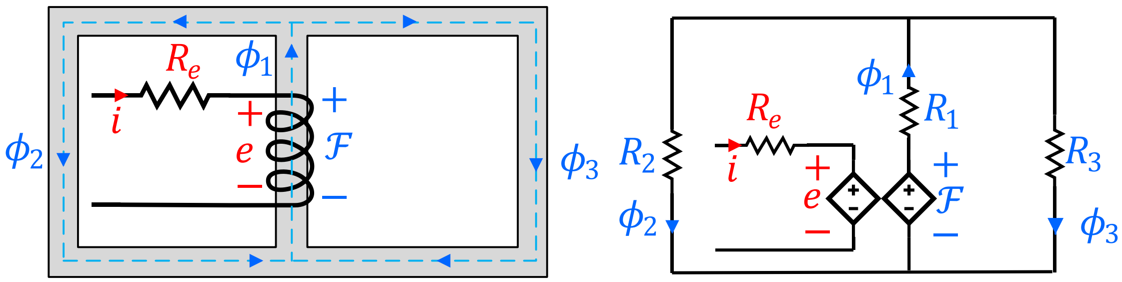

Figure 1.1 Hopkinsons' analog of the iron core inductor

The reluctances of the side columns R_2 and R_3 are parallel, and the total of their magnetic fluxes equals the magnetic flux of the reluctance of the centre column R_1. Each reluctance is determined by

$$R = \frac{l}{\mu\, A} \tag{1.2}$$

where l and A are the mean lengths and cross-sections of flux tubes associated with each reluctance, respectively. And μ is the magnetic permeability of the core. The magnetic fluxes are generated by the magnetomotive force of the winding which is calculated using Ampère's law as

$$\mathcal{F} = \oint_{\partial S} \vec{H} \cdot \vec{\mathrm{d}l} = Ni \tag{1.3}$$

where, $\mathcal{F}$ is the magnetomotive force of the winding, N denotes the number of turns in the winding, i denotes the current flowing through the winding, and $\vec{H}$ denotes magnetic filed. As a result, it makes sense to represent the magnetomotive force in the analogue circuit using a voltage source. The winding's time-varying magnetic flux induces a voltage on the circuit's electric side, the value of which is governed by Faraday's law, as

$$e = \oint_{\partial S} \vec{E} \cdot \vec{\mathrm{d}l} = -N\frac{d\phi}{dt} \tag{1.4}$$

where ϕ is the magnetic flux and e is the induced electromotive force. Thus, the electric side considers the winding as a controlled voltage source whose value is determined by the time derivative of the current, which in Hopkinsons' analogy represents the magnetic flux.

In the Hopkinson analogy, a type of mutator called Type-2 L-R mutator is employed to link the magnetic and electric parts of the circuit. This type of mutator is illustrated in Figure 1.2, with the left side (blue circuit) representing the electrical part and the right side (black circuit) representing the magnetic part. The relationships employed to derive the values of the voltage sources in both the electric and magnetic of this mutator, which are functions of the currents in the magnetic and electric sides, are defined by

$$v_1 = -N\frac{di_2}{dt} \Leftrightarrow e = -N\,\frac{d\phi}{dt} \tag{1.5}$$

$$v_2 = Ni_1 \Leftrightarrow \mathcal{F} = Ni \tag{1.6}$$

where v_1 and i_1 are the voltage and current related to the mutator's electric side, which reflect the electromotive force voltage induced in the electric circuit e and the electric current flowing into the winding i, respectively. And v_2 and i_2 are the voltage and current related to the mutator's magnetic side, which represent the magnetomotive force in the magnetic circuit $\mathcal{F}$ and the magnetic flux flowing into the core ϕ, respectively. Thus, (1.5) and (1.6) are equivalent to (1.4) and (1.3), respectively.

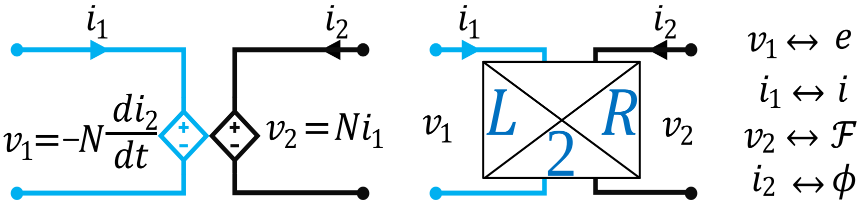

Figure 1.2 Type-2 L-R mutator

Despite its widespread use, the Hopkinson analogy has several limitations in representing the physical behaviours of magnetic devices. The limitations are primarily energy related.

The first energy-related disadvantage is that, although the product of electromotive force and current provides power, the product of their analogous equivalents, magnetomotive force and magnetic flux, yields energy [8, 10, 11]. The second disadvantage in terms of energy is that electric resistance is a component that dissipates energy and is not a real substitute for magnetic reluctance, which stores energy [5]. Another energy-related drawback is that magnetic inductors, which are energy-storing components, are employed to simulate the core's energy dissipation. In fact, from an energy viewpoint, using a magnetic inductor, also known as a magnetic loss element [5, 9] or transference [12, 13], as an energy dissipating element is meaningless.

Hopkinson's analogy has a significant disadvantage when it comes to implementation in circuit simulators. Indeed, because initial current conditions for resistance cannot be defined, this approach does not allow for the implementation of initial current conditions for an inductor using resistance. However, based on (1.3), because the initial condition of the inductor current is reflected in the magnetomotive force, the initial condition of the inductor current can be considered by introducing DC voltage sources in series with the reluctances in the magnetic circuit. However, the added DC source must be connected only at time t=0 and disconnected at time t>0, which complicates simulations [10, 11].

1.1.2 Buntenbach Analogy

The Buntenbach analogy [3, 12] was proposed to address the issues raised by the Hopkinson analogy. The resistors in the Hopkinson analogy are replaced by capacitances in the Buntenbach analogy. If, in (1.1), magnetic flux ϕ is stated in terms of magnetomotive force $\mathcal{F}$, the new equation is derived

$$\phi = \Lambda\,\mathcal{F} \tag{1.7}$$

where Λ is the permeance, the reciprocal of reluctance R, and its unit is H. Also, looking to the capacitance C definition which relates the electric flux stored ψ with its voltage e,

$$\psi = C\,e \tag{1.8}$$

As can be seen from the comparison of (1.7) and (1.8), it is evident that in the Buntenbach analogy, capacitance C is analogous to permeance Λ, electromotive force e is analogous to magnetomotive force $\mathcal{F}$, and electric flux ψ is analogous to magnetic flux ϕ.

Figure 1.3 illustrates the analog circuit for an iron core inductor derived by this analogy.

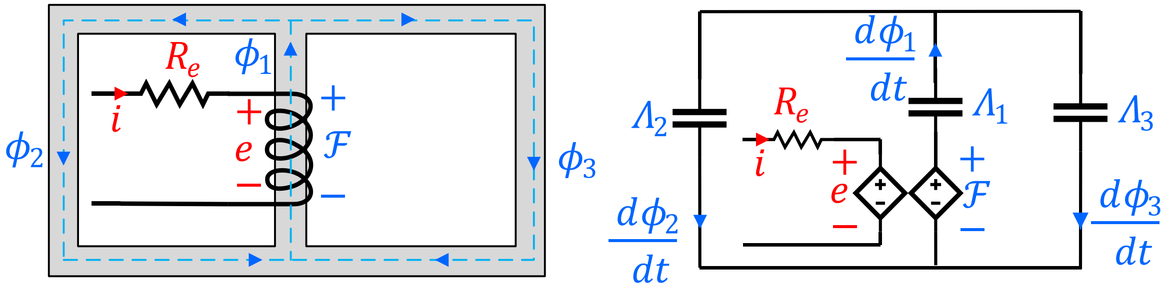

Figure 1.3 Buntenbach's analog of the iron core inductor

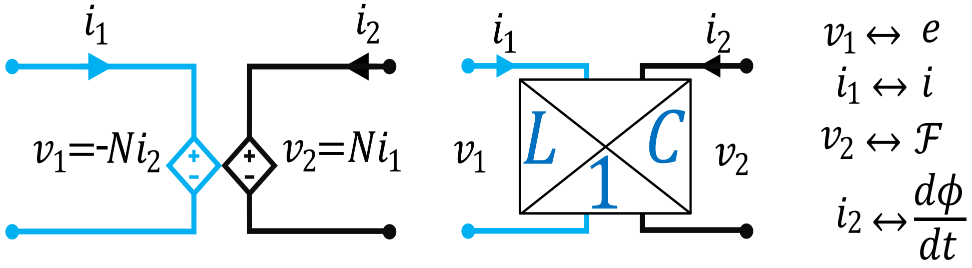

Figure 1.4 Type 1 L-C mutator

In contrast to the Hopkinson analogy, the Buntenbach analogy uses a different type of mutator, the Type 1 L-C mutator [14-16], to connect the magnetic and electric parts of the circuit. This type of mutator is represented in Figure 1.4 with the electrical part on the left (blue circuit) and the magnetic part on the right (black circuit). Here is a set of the relationships associated with this mutator

$$v_1 = -Ni_2 \Leftrightarrow e = -N\,\frac{d\phi}{dt} \tag{1.9}$$

$$v_2 = Ni_1 \Leftrightarrow \mathcal{F} = Ni \tag{1.10}$$

where v_1 and i_1 are the voltage and current related to the mutator's electric side, which reflect the electromotive force voltage induced in the electric circuit e and the electric current flowing into the winding i, respectively. And v_2 and i_2 are the voltage and current related to the mutator's magnetic side, which represent the magnetomotive force in the magnetic circuit $\mathcal{F}$ and time-derivative of magnetic flux flowing into the core $d\varphi/dt$, respectively. Similar to Hopkinson analogy, it can be observed that, (1.5) and (1.6) are equivalent to (1.4) and (1.3), respectively.

The Buntenbach analogy overcomes all the Hopkinson analogy's energy-related drawbacks. First, just as the product of electromotive force and conduction current results in power, so does the product of their analogous equivalents, magnetomotive force and the time derivative of magnetic flux. In this analogy, as opposed to the Hopkinson analogy, the capacitor, which is energy storing element, is employed to represent permeance. In fact, by looking at the electric energy stored in the capacitor E_c and the magnetic energy stored in the permeance E_Λ which have been derived in (1.11) and (1.12), respectively, it can be concluded that they are analogous to each other.

When the electric energy stored in the capacitor E_C and the magnetic energy stored in permeance E_Λ as calculated in (1.11) and (1.12), respectively, are compared, it can be shown that the two parameters are analogous.

$$E_C = \frac{1}{2} C e^2 = \frac{1}{2} \psi\, e = \frac{1}{2} \frac{\psi^2}{C} \tag{1.11}$$

$$E_\Lambda = \frac{1}{2} \Lambda\, \mathcal{F}^2 = \frac{1}{2}\, \phi\, \mathcal{F} = \frac{1}{2} \frac{\phi^2}{\Lambda} \tag{1.12}$$

Also, the Buntenbach analogy overcomes the Hopkinson analogy's difficulty in expressing the current initial condition, because initial voltage (or initial electric charge) for the capacitors can be defined. Because of the aforementioned reasons, the Buntenbach analogy is now occasionally favoured over Hopkinson in modelling transformers and inductors in some power system [17] or power electronic [18, 19] applications. In addition, the fact that both $i(= dq/dt)$ and $d\varphi/dt$ are time rate of change variables with units of Webers/second (Wb/s) and Coulombs/second (C/s), respectively, is further evidence that this analogy beats the Hopkinson analogy in terms of expressing physical behavior.

1.1.3 Duality principle

Another strategy for linking magnetic and electric circuits is the duality principle, which is used in electric circuit theory to try to find reciprocal circuits with identical behaviour patterns [4, 6, 7].

In electric circuit theory, the duality principle includes reciprocal circuit elements and the exchange of dual parameters. In electrical circuits, this principle results in the voltage becoming the current, the series elements becoming parallel, the resistance becoming conductance, the capacitance becoming inductance, the reactance becoming susceptance, the short-circuit becoming an open-circuit, the star circuits becoming mesh circuits, Kirchhoff's current law becoming Kirchhoff's voltage law, and so on.

Cherry [5] used the original principle of duality to identify a reciprocal electric circuit for the magnetic circuit equations, and Slemon [20] added nonlinear effects to incorporate the magnetic circuit's nonlinear equations. The duality principle is applied on the magnetic circuits based on the relationship between the inductance L and reluctance R

$$L = \frac{N^2}{R} \tag{1.13}$$

where N is the number of winding turns. The reciprocal relationship between R and L provides more evidence for the existence of a reciprocal electric circuit for each given magnetic circuit. Additionally, by employing duality, the magnetomotive force $\mathcal{F}$ is transformed into current i, the time derivative of magnetic flux $(d\phi/dt)$ is transformed into voltage v, the magnetic circuit nodes are transformed into electric circuit loops, and the electric circuit loops are transformed into magnetic circuit nodes. Additionally, ideal transformers are employed to connect the section of the circuit that represents the external electric circuit with the section that represents the magnetic circuit's dual. This concept will be discussed in further detail in 2.1.3.

To demonstrate how [5] used a topological technique to graphically build a dual circuit, see Figure 1.5, which depicts dual transformation for an iron core inductor. First, the iron core inductor is discretized and represented as a magnetic circuit in Figure 1.5. Then, in the center of each mesh of the magnetic circuit, a knot is defined and assigned a number; in this example, as seen in Figure 1.5, the magnetic circuit consists of two meshes, each with its own defined and numbered knot. A knot is also considered and assigned the number 0 for the exterior mesh. The topology of the electric circuit is then established by drawing lines between the defined knots using a few simple criteria given in [20, 21]. The drawn lines are indicated in Figure 1.5 by purple dashed lines. Following the drawing of the electric circuit's topology, the dual circuit is produced by replacing the magnetic components with their electric analogues.

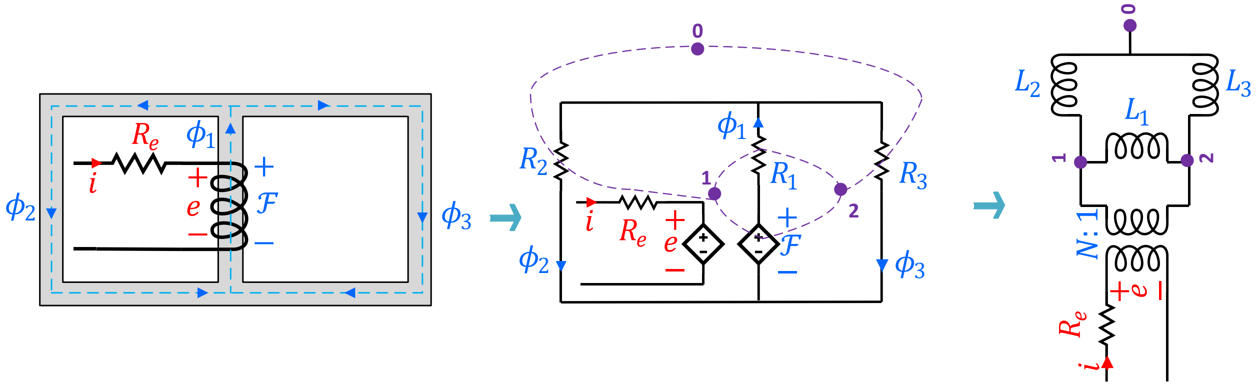

Figure 1.5 Derivation of a dual circuit for an iron core inductor using duality transformation

This approach has the advantage of Buntenbach analogy for supporting a physically correct model. First, the reluctance is represented by an inductor, which is a storing element. Second, the power in the dual circuit is equivalent to the power in the magnetic circuit, as is the energy in the dual circuit to the energy in the magnetic circuit. Thirdly, since the inductor's initial condition is defined, there is no need to connect a voltage source in series with the inductors, as was done in the Hopkinson analogy. Apart from these reasons, this method was chosen for modelling transformers [5] because it links the magnetic circuit's electric dual with the external circuit via ideal transformers, that are seen more often in circuit simulation tools.

1.1.4 Derivation duality circuit from Hopkinson and Buntenbach analogies

There is an interesting relationship between the Hopkinson and Buntenbach analogies and the duality principle, which allows for a transition from Hopkinson or Buntenbach analogy to duality. This relationship and its related transition were mentioned briefly in [22], but they are elaborated on in this section. Actually, the transition from the Buntenbach or Hopkinson analogy to duality is accomplished by the fact that a mutator enables the transition from one element to its dual by passing it from the magnetic side to the electric side of the electromagnetic circuit.

This section provides an explanation of the transition from the Buntenbach analogy to the duality principle; nevertheless, the transition from the Hopkinson analogy to the duality principle follows the same procedure. To do so, Figure 1.6 depicts a simple circuit with its magnetic portion represented using the Buntenbach analogy.

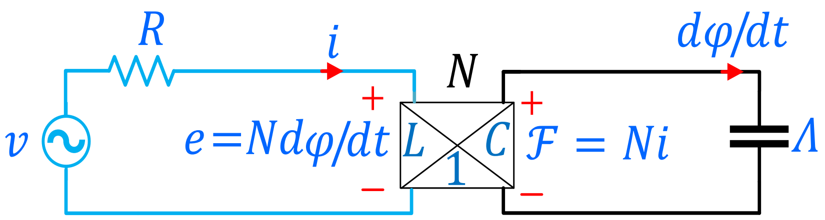

Figure 1.6 Simple circuit based on Buntenbach analogy

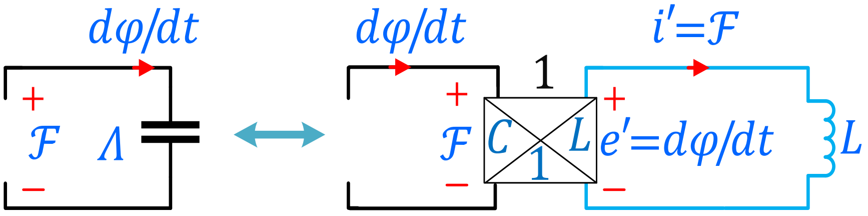

Figure 1.7 Equivalent circuits demonstrating the conversion of a permeance into an inductor by adding an L-C mutator

Analytically, it can be shown that shifting the magnetic capacitor (permeance) to the electric side of an L-C mutator converts it to its dual (inductor). Figure 1.7 demonstrates these two equivalent circuits. The left circuit depicts the magnetic capacitor (permeance), while the right circuit represents its dual circuit consisting of an inductor and a type-LC mutator. The type-LC mutator used has a coupling factor of 1. To establish the relation between permeance and its dual inductor, we compare the ruling relations of both circuits depicted in Figure 1.7. For the magnetic permeance in the left circuit,

$$\frac{d\phi}{dt} = \Lambda \frac{d\mathcal{F}}{dt} \leftrightarrow \; i = c\frac{dv}{dt} \tag{1.14}$$

where $\frac{d\phi}{dt}$, $\mathcal{F}$, and Λ represent the time durative of magnetic flux, magnetomotive force source and permeance in the magnetic circuit.

And for the inductor in the right circuit,

$$e' = L\frac{di'}{dt} \leftrightarrow \frac{d\phi}{dt} = L\frac{d\mathcal{F}}{dt} \tag{1.15}$$

where e', i', and L indicate the electromotive force, the electric current, and the inductor, which in the duality analogy represent the time derivative of the magnetic flux $\frac{d\phi}{dt}$, the magnetomotive force $\mathcal{F}$, and the dual of the permeance Λ, respectively.

By comparing (1.14) and (1.15), we can see that $L = \Lambda$. As a result, the permeance in Figure 1.6 can be replaced by its equivalent circuit, the right circuit in Figure 1.7, which transitions the circuit in Figure 1.6 to the new circuit in Figure 1.8. It can be proved in the derived circuit that two mutators in series are equivalent to one ideal transformer, the relationships of which are illustrated in (1.16) and (1.17). Figure 1.9 displays this equivalence based on these relations. Finally, it is concluded that the circuit derived from the Buntenbach analogy shown in Figure 1.6 can be turned into the duality derived circuit displayed in Figure 1.10.

$$\frac{e}{e'} = \frac{-N\frac{d\varphi}{dt}}{-\frac{d\varphi}{dt}} = N \tag{1.16}$$

$$\frac{i}{i'} = \frac{\frac{\mathcal{F}}{N}}{\mathcal{F}} = \frac{1}{N} \tag{1.17}$$

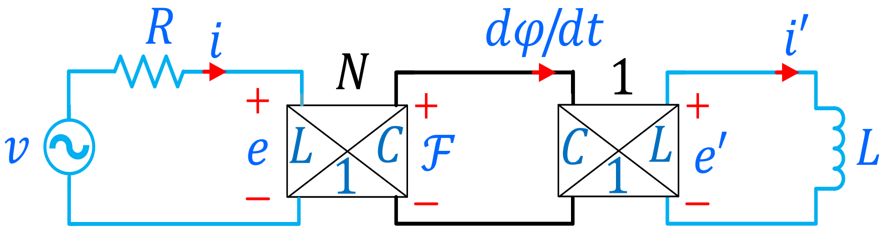

Figure 1.8 The circuit equivalent to Figure 1.6 resulted from replacing the permeance with its dual circuit

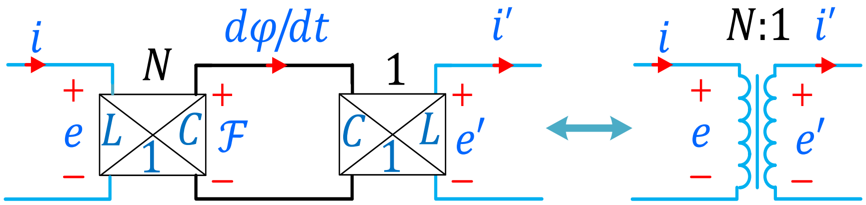

Figure 1.9 Conversion of two series-connected mutators into an ideal transformer

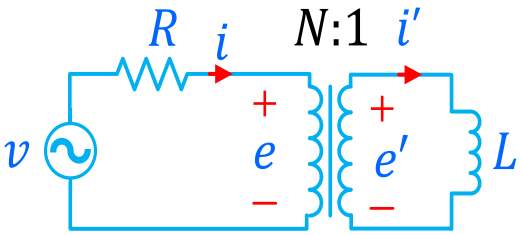

Figure 1.10 Duality-derived circuit equivalent to the circuit in Figure 1.6

1.2 Literature review

1.2.1 Coupled problems for modelling magnetic devices in power systems

Magnetic devices, such as inductors, transformers, and rotating electrical machines, play a vital role in power systems. As a result, accurate simulation of many phenomena in power systems, such as electromagnetic transient events, requires accurate electromagnetic modelling of magnetic devices. Designers must also take into account how the external network affects the internal behavior of magnetic devices, including magnetic flux distribution, iron losses, and identification of hot spots. Circuit simulators and field solvers are two popular tools for performing these types of analysis.

When it comes to magnetic devices, FEM [23] can represent them in great detail, taking into account nonlinear behavior as well as geometrical complexities. However, because FEMs lack power system components such as transmission lines and circuit breakers, they are unable to be utilized to analyze a magnetic device in a large power system network. To overcome this issue, the coupling of magnetic field equations and circuit equations is established. There are two typical methods for providing coupling: direct (or strong) coupling and indirect (or sequential, or weak) coupling [24]. In both, field domains are discretized spatially using a variety of techniques, including the Finite Element Method, the Finite Difference Method, the Finite Integration Technique, and the Boundary Element Method. Additionally, various discretization methods may be applied to the physical parts. A time-dependent system of ordinary differential equations (ODE) or differential algebraic equations (DAE) is generated as a result of spatial discretization.

The direct technique simultaneously employs a single system of equations that contains all of the degrees of freedom required. To solve the magnetic equations, a formulation involving the magnetic potential vector is used. The conductor current is expressed in terms of current density, and the flux linkage is determined from the potential vector to establish coupling. Step-by-step numerical integration is used to solve the time-dependent differential system that results from coupling. A Newton–Raphson iterative approach is utilized to account for the magnetic and electric nonlinearities. This method, however, is not appropriate for large power networks because it lacks sufficient power component models.

The indirect method solves the field and circuit equations separately, but keeps them connected through coupling coefficients, like in [25]. Given the ability to use circuit simulators, indirect techniques may take into account the impact of huge networks with a diverse range of power components on the magnetic device, which is not achievable with direct methods. However, since indirect techniques need numerous iterations between the field and circuit equations, they are computationally expensive and result in major numerical delays.

Despite the fact that both coupling-based systems are highly accurate, they have severe implementation limitations, including lengthy computation times and a number of numerical issues. Additionally, when examining magnetic devices in power systems, analysts favor lumped models that are compatible with circuit modelling software such as EMT-type tools over distributed field models. However, as stated in this thesis, existing lumped parameter models (or circuit-based models) are not as accurate as FEM, and although a few lumped models with appropriate accuracy exist, they cannot be easily implemented in EMT-type tools.

1.2.2 Existing lumped circuit-based models for modeling magnetic devices

Circuit simulation software currently uses lumped models, which have a limited number of circuit elements to account for the flux paths of magnetic devices. The magnetic equivalent circuit (MEC) approach is the most extensively used and earliest lumped method for modelling magnetic devices. [12, 13]. The ability of the MEC to convert a complicated magnetic circuit into a relatively simple, resistive electrical circuit makes it appealing for both the design and study of magnetic devices [26]. When detailed modelling of magnetic flux paths and internal behavior is not required, lumped parameter models, such as MEC, provide sufficient accuracy. In these models, the equivalent elements corresponding to the magnetic flux paths are estimated using analytical equations with the design data as input. Although these analytical equations are sufficiently accurate in estimating the reluctance of flux paths in the core, they are not good enough in estimating the reluctances of flux paths in the air. Consequently, they are incapable of adequately accounting for leakage fluxes between winding turns or fluxes that flow beyond the core during saturation or fringing fluxes in cases where there are air gaps in the core.

Two distinct approaches have been used to increase the accuracy of flux path representations in the literature. First, various studies have improved analytical formulas by estimating the overall image of flux paths and identifying extra elements that can be used to depict these additional estimated fluxes more accurately. MEC, for example, has been improved in [27] to account for fringing and leakage fluxes for a special case of an inductor. While these types of studies improve accuracy for certain cases, they are not generic and are based on assumptions that are valid only in those specific cases. In addition, they can accurately represent the external behavior of magnetic devices, but not their internal behavior. Second, in some magnetic device modelling approaches, test data is employed to estimate the equivalent elements associated with difficult-to-define flux paths. Topological transformer models [28-33] illustrate one sort of such model in which leakage inductances are computed using short-circuit test data. However, access to test data for devices with many windings is difficult and such data is not suitable for specific studies, such as internal winding faults. Additionally, similar to the first technique, this approach cannot represent an internal flux path view. These models, however, are in great demand since detailed design data for new magnetic devices is typically considered confidential by their manufacturing factories and is seldom available for older magnetic devices. To emphasize the limitations of existing lumped parameter models and partly since this thesis is primarily concerned with transformers, the next section reviews the existing transformer models used in EMT-type tools such as EMTP [34].

1.2.2.1 Saturable Transformer Component (STC) model

The Saturable Transformer Component (STC) is the most extensively used transformer model, which is still utilized in EMT-type software. STC [35], also known as the star equivalent circuit, is limited to modelling single-phase transformers or three-phase transformers composed of three similar single-phase transformers. Figure 1.11 illustrates the STC model for a single-phase two-winding transformer. To adapt extra windings, the parallel branch is not modified; instead, additional windings in the form of series impedances to the star point are inserted [35], see Figure 1.12.

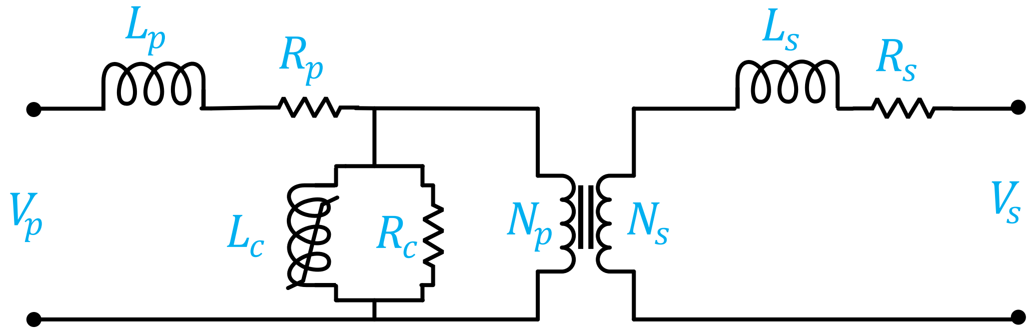

Figure 1.11 STC representation of single-phase two-winding transformer [35]

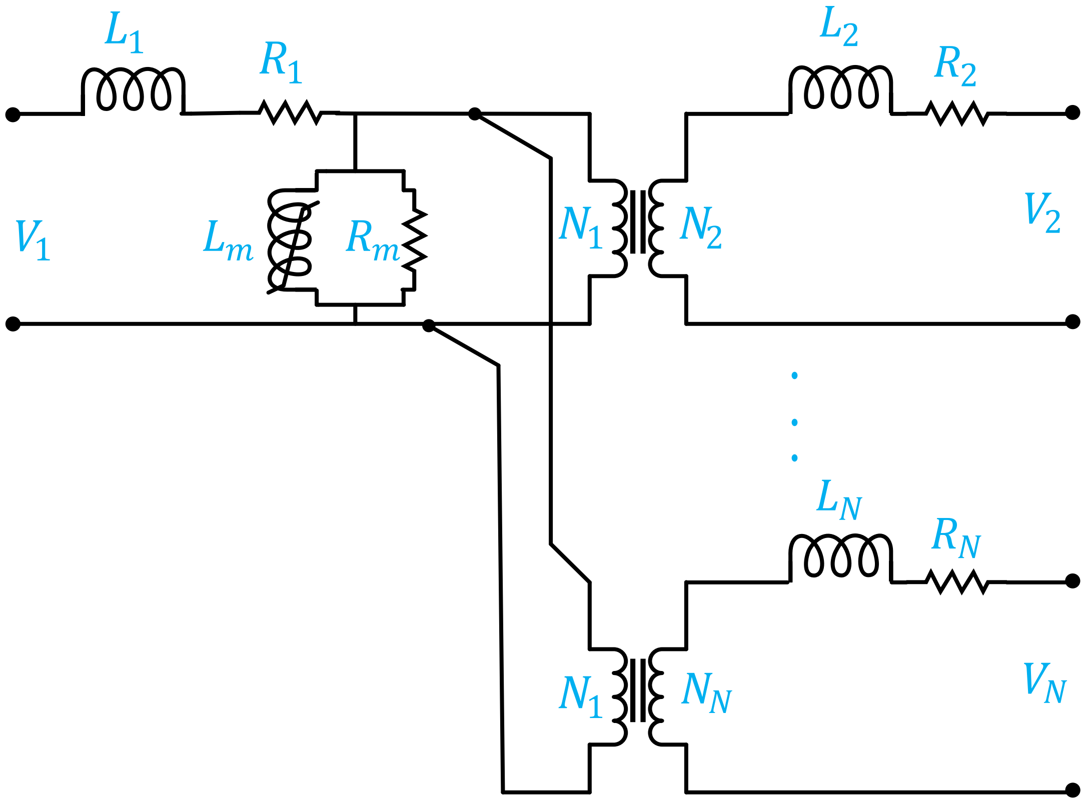

Figure 1.12 STC representation of single-phase N-winding transformer [35]

Although the STC model is simple to use, it has some important drawbacks: first, it is incapable of simulating phase coupling due to its inability to include limb interactions; second, despite attempts to represent the zero-sequence phase in this model, the positive- and zero-sequence phases are identical; and third, a negative inductance is observed in the STC-based three-winding transformer model. Not only is this negative inductance physically meaningless, it may contribute to numerical instability [36-38].

1.2.2.2 BCTRAN transformer model

The BCTRAN transformer model [39], is an experimentally obtained model. Transformers are modelled using BCTRAN or matrix representation in the form of impedance or admittance matrices. In this method, the branch impedance matrix $[Z]$ is used to present the steady-state equations of a multiphase multiwinding transformer

$$[V] = [Z][I] \tag{1.18}$$

In order to use (1.18) for transient calculations, it needs to be rewritten as

$$[v] = [R][i] + [L][di/dt] \tag{1.19}$$

where $[R]$ and $j\omega[L]$ represent, respectively, the real and imaginary parts of $[Z]$ whose elements are derived using excitation tests (short- and open-circuit tests). This model is applicable to both single-phase and three-phase transformers, and there is no limitation on the number of windings. It can also consider all couplings between phases, but not differences in core topologies or winding configurations.

When applying (1.18) or (1.19), there is a possibility that some accuracy issues will occur due to the fact that the branch impedance might be ill-conditioned for very small exciting currents. To address the accuracy issues caused by the impedance matrix representation, an admittance matrix representation is used

$$[I] = [Y][V] \tag{1.20}$$

where $[Y]$, the admittance matrix, can be derived directly from standard short circuit measurements.

Alternate representation of the transformer using BCTRAN is as following formula

$$[di/dt] = [L]^{-1}[v] - [L]^{-1}[R][i] \tag{1.21}$$

Since these equations are linear, they cannot account for core saturation and other nonlinearities related to the core, such as hysteresis. To consider the core nonlinearities using BCTRAN, two strategies are applied. First strategy attempts to linearize core nonlinearities and incorporate them into matrix representation; nevertheless, this approach can result in simulation errors during nonlinear transformer operating conditions. The second strategy is to omit all excitation equations from the matrix formulation and model them as nonlinear elements externally attached to the transformer terminals, as shown in Figure 1.13. Despite the fact that it does not cause the simulation errors introduced by the first approach, the nonlinear branch was not attached in a topologically correct way to the model, preventing this method from being applicable to all operating conditions [35].

Compared to the STC model, the BCTRAN model has a significant advantage in that it can differentiate between positive and zero-sequence transformer models, enabling it to represent unbalanced events. However, similar to the STC model, the BCTRAN has a critical limitation: it does not provide an accurate topological representation of the transformer [37].

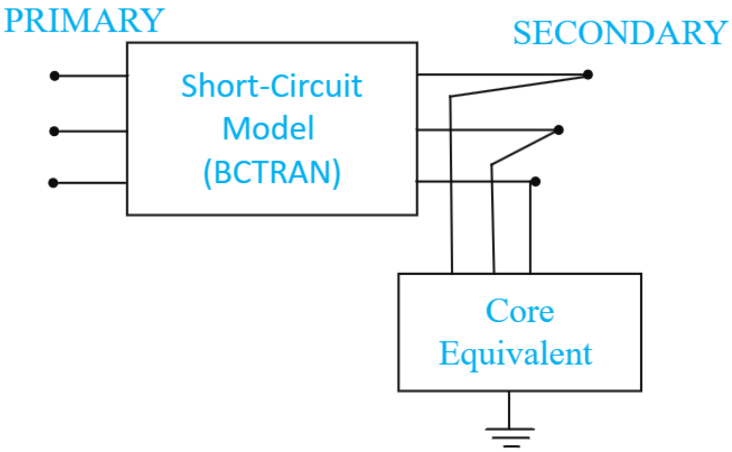

Figure 1.13 Representation of two-winding transformer with an externally attached core, based on the BCTRAN model

1.2.2.3 Topological transformer models

Topological models, which claim to be physically correct, were proposed to overcome the limits of BCTRAN and STC for transient studies. Topological transformer models represent transformers in the form of flux paths and can be used to simulate various types of cores and winding topologies, taking into account their differences. The topological models are UMEC, TOPMAG, and the Hybrid transformer [10, 37].

1.2.2.3.1 Unified Magnetic Equivalent Circuit (UMEC) model

The Unified Magnetic Equivalent Circuit (UMEC) model was proposed [40-42] as a topological substitute for classic transformer models. UMEC was implemented in EMTDC. For a three-legged, two-winding transformer, Figure 1.14 depicts all of the flux paths (ϕ_1, ϕ_2, …, ϕ_{14}) that are treated as distinct flux tubes in the model that is derived by UMEC. This will allow us to demonstrate how UMEC defines the magnetic equivalent circuit. The UMEC model for the transformer depicted in Figure 1.14 is illustrated in Figure 1.15.

In this circuit, reluctances R_{Y_1} and R_{Y_2} represent the left and right yokes through which fluxes ϕ_{13} and ϕ_{14} pass, respectively. Reluctances $R_{A_{L_1}}$, $R_{B_{L_1}}$, and $R_{C_{L_1}}$ represent the top half of each phase's wound leg, where fluxes ϕ_1, ϕ_3, and ϕ_5 pass through, respectively, and reluctances $R_{A_{L_2}}$, $R_{B_{L_2}}$, and $R_{C_{L_2}}$ represent the down half of each phase's wound leg, through which fluxes ϕ_2, ϕ_4, and ϕ_6, respectively, pass. Reluctances $R_{A_{l_1}}$, $R_{B_{l_1}}$, and $R_{C_{l_1}}$ represent leakages for phases a, b, and c of the top winding, respectively, through which fluxes ϕ_7, ϕ_9, and ϕ_{11} flow. And reluctances $R_{A_{l_2}}$, $R_{B_{l_2}}$, and $R_{C_{l_2}}$ represent leakages for phases a, b, and c of the down winding, respectively, through which fluxes ϕ_8, ϕ_{10}, and ϕ_{12} flow. To represent the out-of-core fluxes, Figure 1.14 depicts three flux tubes, one for each phase, through which fluxes ϕ_{15}, ϕ_{16}, and ϕ_{17} flow. In the magnetic equivalent circuit depicted in Figure 1.15, these three out-of-core flux tubes are represented by the reluctances R_{A_0}, R_{B_0}, and R_{C_0}. To show the difference between this model and others, Figure 1.15 shows the magnetic circuit derived by UMEC, but since EMTDC lacks mutators, magnetic circuit equations are directly inserted into the admittance matrix using a multi-port Norton equivalent circuit.

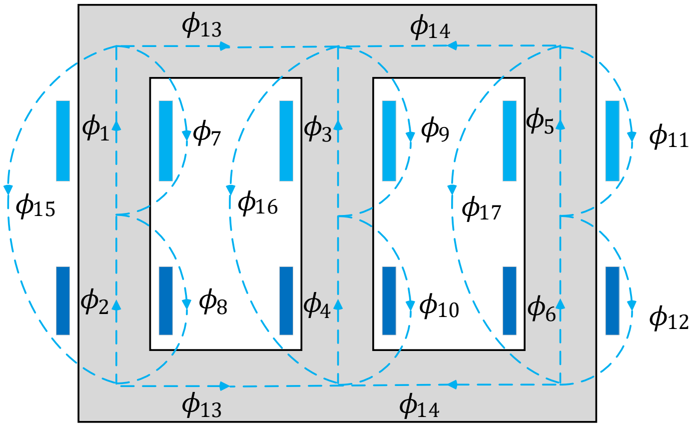

Figure 1.14 Magnetic flux paths assumed by UMEC for the three-legged two-winding transformer

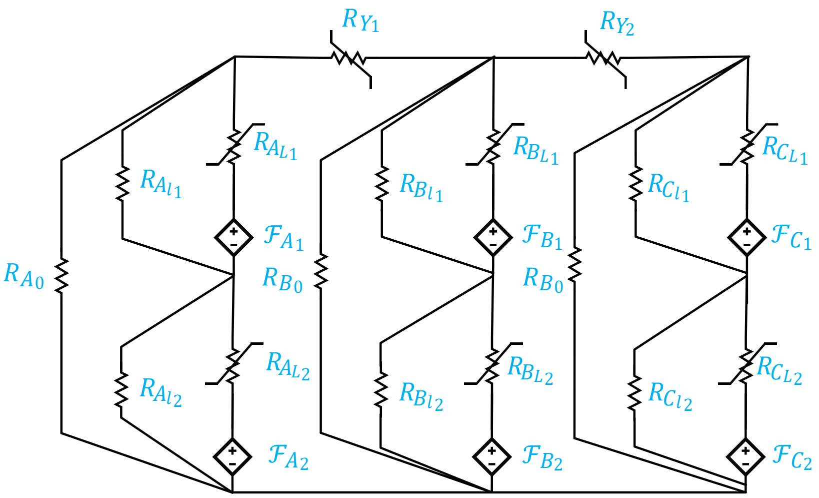

Figure 1.15 Magnetic circuit of UMEC model for the two-winding three-legged transformer shown in Figure 1.14

1.2.2.3.2 TOPMAG model

In 1994, the TOPMAG model was improved and included into the DCG/EPRI EMTP version 3. The objective was to improve the core-type transformer model with concentric windings by incorporating core nonlinearities so that it can simulate the imbalance between the centre leg and the outer legs of three-phase transformers.

This model is considered to be a duality-derived model, but to illustrate the distinction between this model and other topological transformer models, Figure 1.16 and Figure 1.17 show, for a three-legged transformer, the magnetic flux paths defined by this model and the magnetic equivalent circuit, respectively. As shown in Figure 1.16, the definitions of magnetic flux paths include both leakage paths for each winding and leakage paths between windings. In Figure 1.16, the leakage flux paths of the primary winding for three phases are depicted by ϕ_4, ϕ_6, and ϕ_8, which are represented by reluctances $R_{A_{l_1}}$, $R_{B_{l_1}}$, and $R_{C_{l_1}}$ in the magnetic equivalent circuit of Figure 1.17. Also, in Figure 1.16, ϕ_5, ϕ_7, and ϕ_9 depict the leakage flux paths of three phases of the secondary winding, which are represented in the magnetic equivalent circuit by the reluctances $R_{A_{l_2}}$, $R_{B_{l_2}}$, and $R_{C_{l_2}}$ respectively. In addition, one flux tube is assumed for each phase to represent the leakage between the primary and secondary windings of that phase, as shown in Figure 1.16, fluxes ϕ_{10}, ϕ_{11}, and ϕ_{12} pass through them. In the magnetic equivalent circuit, these three leakage flux tubes are represented by the reluctances $R_{A_{l_{12}}}$, $R_{B_{l_{12}}}$, and $R_{C_{l_{12}}}$. Since this model was developed for a transformer with concentric windings, only one flux tube is considered for each column, as shown in Figure 1.16. Fluxes ϕ_1, ϕ_2, and ϕ_3 pass through these three flux tubes, and as shown in Figure 1.17, these flux tubes are represented by three reluctances R_{A_L}, R_{B_L}, and R_{C_L}, respectively. Similar to the UMEC model for representing the yokes for both the up and down portions of yokes located on the left side of the middle column, only one flux tube through which ϕ_{13} passes is taken into account. Similarly, for both the up and down portions of yokes located on the right side of the middle column, only one flux tube through which ϕ_{14} passes is considered. In the magnetic equivalent circuit depicted in Figure 1.17, these two flux tubes of the yoke portions are represented by horizontally positioned reluctances R_{Y_1} and R_{Y_2}. Like UMEC, three out-of-core flux tubes are defined in the TOPMAG model, as illustrated in Figure 1.16, through which fluxes ϕ_{15}, ϕ_{16}, and ϕ_{17} pass. These three out-of-core flux tubes are represented by the reluctances R_{A_0}, R_{B_0}, and R_{C_0} in the magnetic equivalent circuit shown in Figure 1.17.

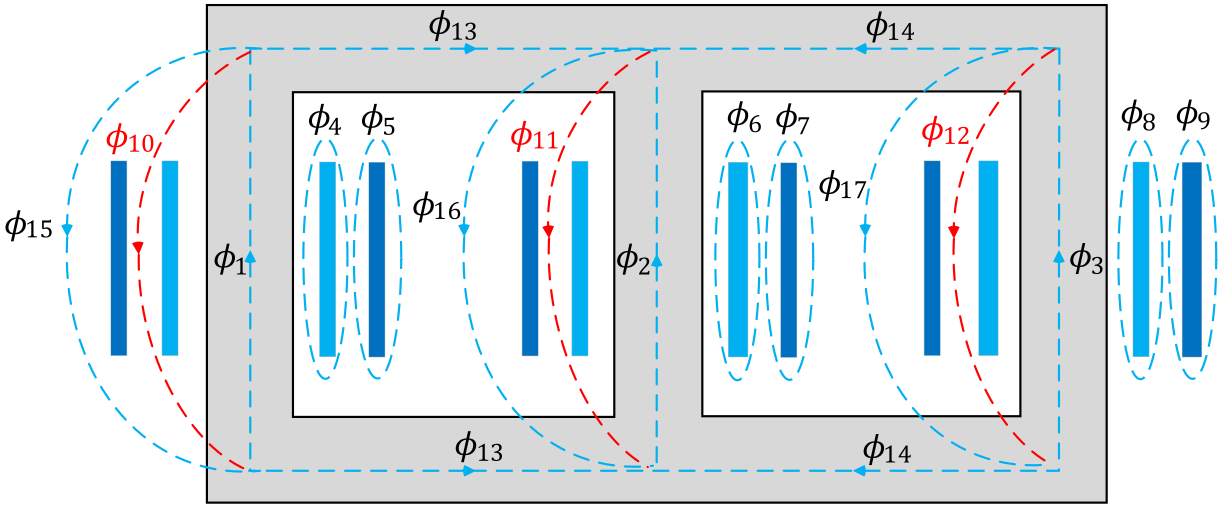

Figure 1.16 Magnetic flux paths assumed by TOPMAG for the three-legged two-winding transformer with concentric windings

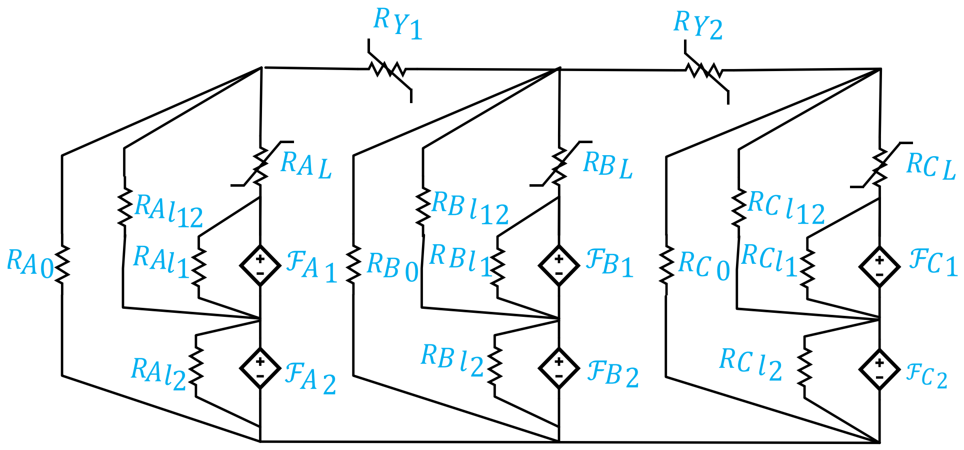

Figure 1.17 Magnetic equivalent circuit of TOPMAG model for the two-winding three-legged transformer shown in Figure 1.16

The TOPMAG transformer model was proposed based on the duality principle and is regarded one of the duality-derived topological models. Figure 1.18 demonstrates the duality-derived circuit representation of the TOPMAG model for the transformer depicted in Figure 1.16. In the duality circuit, the parameter definitions are identical to those in Figure 1.17, with the exception of the substitution of reluctances with symbol R for inductors with symbol L. It is noteworthy that this module had serious problems in EMTP and it was not possible to use it.

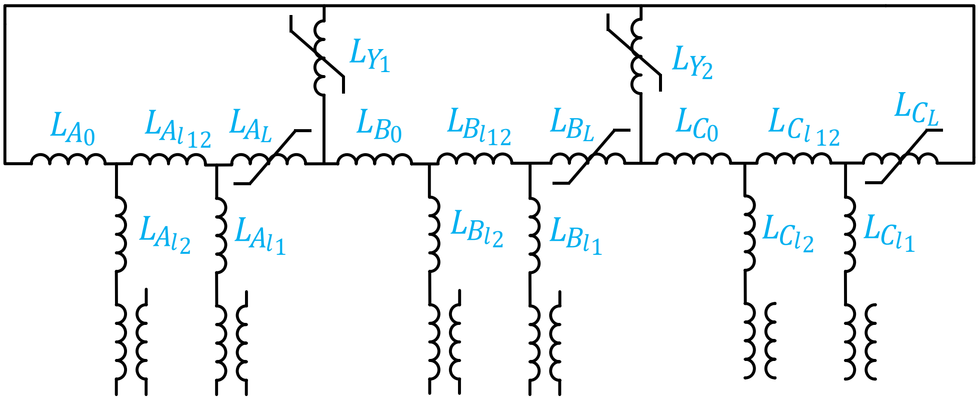

Figure 1.18 Duality derived transformer model based on the TOPMAG model for the transformer shown in Figure 1.16

1.2.2.3.3 Hybrid transformer model

It was discovered that topological transformer models are less accurate in representing leakage inductances than BCTRAN models; as a consequence, a hybrid approach [43-45] was presented that combines matrix representation with topologically based approaches. Leakage inductances are represented using an inductance matrix derived from the short-circuit test, whereas the core is represented using a topologically correct model. Figure 1.19 illustrates the definition of flux tubes according to the hybrid model. Figure 1.20 depicts the magnetic equivalent circuit generated from this definition of flux paths based on a hybrid approach. In the hybrid method, no flux path for self-leakage of each winding is considered; only leakage flux paths between windings are considered. With the exception of the absence of a self-leakage flux specification, the parameters depicted in Figure 1.19 and Figure 1.20 are identical to those defined in Figure 1.16 and Figure 1.17 respectively. Due to the fact that the duality principle enables topological transformer models to be implemented using standard elements in EMT-type programmes, duality has been utilised to represent topological transformer models. The derived models employing this principle are referred to as duality-derived transformer models [5, 20]. There are a lot of duality-derived transformer models [28-31, 33, 37, 44, 46-57].

The core of the transformer in the hybrid model are represented by a duality-derived circuit, whilst the leakage inductances are represented by a short-circuit matrix. Figure 1.21 illustrates the hybrid model schematic for a three-legged transformer. A fictitious winding is placed precisely on the core leg to connect the topologically correct core model with the matrix representation of leakage inductances. It is assumed that the fictitious winding is indefinitely thin. The leakage inductance between this fictitious winding and the innermost winding is computed by multiplying the leakage inductance between the high-voltage and low-voltage windings by a factor known as K. In several studies, this factor has been assigned a range of possible values. For example, it was given a value of 0.5 in [58], a value of 0.33 in [52], and a value of 0.7 in [43].

Several topological transformer models have been developed during recent years. Among these models is de Leon's [47, 59-62], which, according to Martinez's research [37], is thought to be the most comprehensive transformer model accessible. However, a limitation of topological transformer modelling is a lack of sufficient data to define the model parameters. In the hybrid model, it is also possible to account for core losses by placing resistors in parallel with nonlinear inductors that represent different sections of the transformer core (columns and yokes).

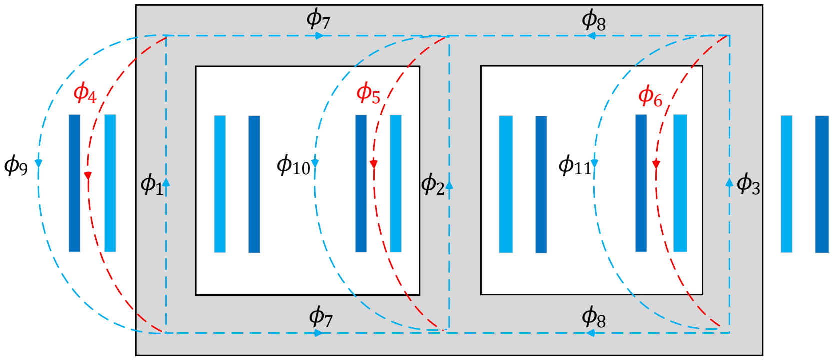

Figure 1.19 Magnetic flux paths assumed by hybrid model for the three-legged two-winding transformer with concentric windings

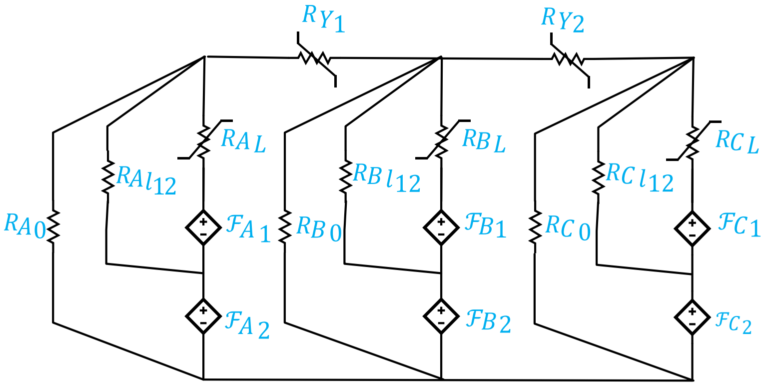

Figure 1.20 Magnetic equivalent circuit of hybrid model for the two-winding three-legged transformer shown in Figure 1.19

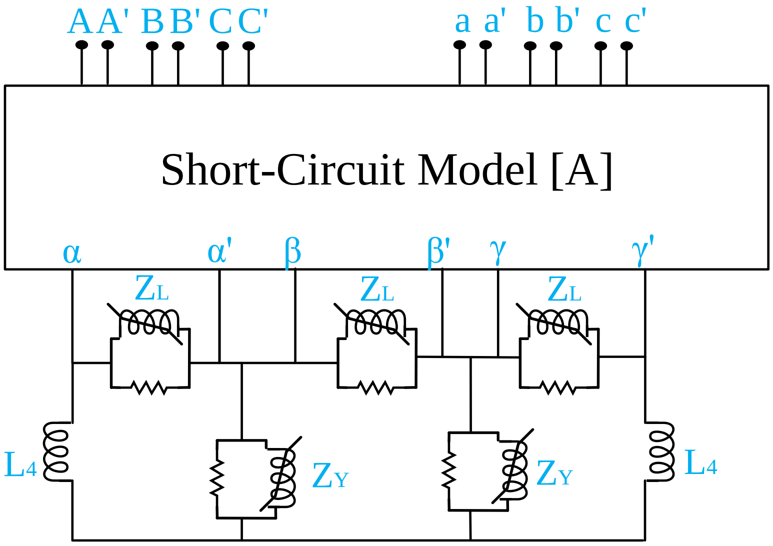

Figure 1.21 Hybrid transformer model for a three-legged transformer

1.2.2.3.4 Summary on the existing models

All of these transformer modelling methods are divided into two categories: black-box and gray-box modelling methods. The STC and BCTRAN transformer models are regarded as black-box models, in which there is no knowledge of the internal characteristics of the transformer. These two models attempt to match accurately the behaviour observed at the terminals of a transformer with measurements of the terminals, but are unable to explain the internal behaviour of the transformer. Even while they are capable of providing accurate terminal behaviour under normal operating conditions, they are not always capable of providing accurate terminal behaviour under unbalanced operating conditions.

Topological transformer models have a advantage over both STC and BCTRAN in that they can determine the terminal behaviour of transformers under all balanced and unbalanced operating conditions. In terms of ability to represent the internal behaviour of transformers, topological transformer models are classified as gray-box models, which fall between white-box models like FEM and black-box models like STC and BCTRAN. Indeed, topological transformer models are created based on measurement data and limited design data and cannot provide a full representation of internal behaviour. Due to the fact that they are all lumped parameter models with a limited number of elements, they can only represent a small number of internal parameters, such as the magnetising current of the columns or yokes. Table 1.1 summarises the characteristics of the aforementioned transformer models.

Considering the limits and uses of these models, it can be concluded that a white-box circuit-based model is required to accurately depict the internal behaviour of transformers. The needed white-box circuit-based technique should be in a meshed form that not only offers an accurate representation of the magnetic device as seen from its terminals, but also provides an accurate representation of the device's internal behaviour.

An approach termed ‘reluctance network model’ [63] has been used to represent a meshed form of the transformer model using circuit elements (see also [64-66]). The proposed solution [13] is primarily for design purposes, whereas the one presented in our paper is for electromagnetic transient studies. Due to the design objective of [63], the number of nodes and elements is minimized to allow for repeated iterations in optimization methods. The model has between 50 to 100 nodes. Due to the limited number of elements in their model, not all transformer geometry details can be demonstrated. In addition, [63] was originally presented for the purpose of calculating leakage inductances, and as such, aimed to distribute elements in the air that are crucial for leakage inductance calculations, but not the core, particularly the columns. Due to the lack of coupling between the transformer model and the external circuit in [63], such a model cannot be utilized to study the transformer's transient behavior in a network. In their method, only magnetomotive force sources have been distributed; electromotive force sources have not been taken into account, so there is no coupling between the magnetic equivalent circuit and the external electric circuit. Also, the authors of [63] used a 3D RNM for calculating leakage inductances, however it kept the limitations explained above for the 2D model.

Recently, [67] proposed mesh modelling of transformers using MEC in EMTP by establishing virtual circuits to account for magnetic flux distribution, which adds complexity to EMT-type software. The method proposed in [67] cannot be implemented using standard elements in EMT-type software; instead, it requires the definition and creation of new elements in these programmes, which is not desirable. Furthermore, this technique is incapable of accounting for three-dimensional effects associated with magnetic flux distributions.

Table 1.1 Summary of transformer models

Model	**Type**	**Characteristics**
Saturable Transformer Component (STC)	Black-box	• Limited to modelling single-phase transformers or three-phase transformers built from three single-phase transformers due to the inability to account for limb interactions. • It is limited to a maximum of three windings. • The magnetising inductance is connected to the star point, which is an incorrect topological representation. • Three-winding models can cause numerical instability. • Does not represent internal transformer characteristics and only provides terminal characteristics.
Matrix Representation (BCTRAN Model)	Black-box	• Phase-to-phase coupling and terminal features are included in these models. • It is only possible to represent linear models. • Nonlinear elements may be added externally to the terminals to provide excitation. • No internal transformer characteristics are represented; only terminal characteristics are presented. • It's based on experimental data and ignores topology.
Topology-based models	Gray-box	• They contain saturation effects in each column and leg. • They consider phase coupling and leakage inductances between windings. • They are topologically correct in comparison to STC and BCTRAN. • There are distinct circuits for each transformer based on how flux tubes are defined. • In addition to terminal characteristics, limited internal transformer characteristics, such as magnetising currents for columns and yokes, are presented.

1.3 Dissertation statement

1.3.1 Problem definition

The purpose of this research is to improve electromagnetic modelling of magnetic devices in order to observe the effect of a power system network on the magnetic device's internal behaviour.

Currently, lumped parameter models are highly preferred by power system analysts for studying electromagnetic transients including magnetic devices. However, it is not possible to observe the effect of the network on the internal behaviour of magnetic devices using the majority of existing lumped parameter models. When it was stated that these models are incapable of providing a detailed representation of magnetic flux distributions, it was stated that this was due to a limited number of lumped elements. It is worth noting that power system analysts prefer circuit-based methods for modelling magnetic devices because they are easily integrated in EMT-type software and interfaced with realistic power systems.

1.3.2 Objectives

The above observations motivated us to develop novel circuit-based approaches for electromagnetic modelling of magnetic devices that are capable of characterising the internal behaviour of magnetic devices, such as magnetic flux distributions. The proposed circuit-based solutions are intended to be easy enough to implement in EMT-type software, such as EMTP, without requiring the addition of new features not previously included in these software packages.

A list of specific objectives is provided below:

- Deriving new strategy for coupling field and circuit equations using exclusively circuit-based methods.

- Mesh functionality will be added to the proposed circuit-based technology in order to simulate magnetic devices in great detail and precision.

- The proposed circuit-based solution will be built using only the components already included in EMT-type software. The proposed distributed circuit-based approach in this thesis will be derived using all three approaches: Hopkinson analogy, the Buntenbach analogy, and the duality principle.

- The proposed circuit-based technique will be enhanced to account for the three-dimensional effects of magnetic fields.
- The models will be validated using the results of the FEM analysis.

1.4 Dissertation outline

Chapter 2 presents a distributed circuit-based technique and explains the underlying theory. Using the proposed strategy, the distributed circuits based on the Hopkinson analogy, the Buntenbach analogy, and the duality principle are derived. This chapter will model an inductor with and without an air gap as a simple demonstration. The proposed approach in this chapter is in two dimensions and is validated by comparison to two-dimensional FEM.

The proposed distributed circuit-based approaches are further developed in Chapter 3 to model transformers. First, the process of creating distributed models for a single-phase two-winding transformer with a small number of elements is described. The procedure for developing distributed models for a three-phase transformer with an adjustable number of meshes is also discussed. Then it is explained how distributed models can be utilised to represent transformer internal faults as well as multi-winding transformers. Finally, the results of the models are then compared to those of 2D FEM to determine the accuracy of the distributed models in describing both internal transformer behaviour and the transformer characteristics observed at its terminals.

The purpose of Chapter 4 is to improve the proposed distributed circuit-based approaches for accounting for the three-dimensional effects of magnetic fields in transformers. First, the limitations of single-2D methods for simulating three-dimensional magnetic field effects are discussed, as well as the significance of shifting from two- to three-dimensional models. Following that, the history of Double-2D FEM is described, as is its efficiency in representing three-dimensional magnetic field effects. After that, the proposed Double-2D circuit-based technique is provided, along with details on how it can be implemented for a two-winding single-phase transformer. It is also emphasised that the proposed Double-2D approach is capable of accurately computing leakage inductances. Leakage inductances are computed using the proposed method, which is then compared to existing analytical methods. The limits and assumptions of existing analytical approaches are discussed, and it is stated how the proposed method addresses these limitations. Finally, the proposed Double-2D circuit-based technique is applied to a three-phase transformer, and its great accuracy in expressing 3D magnetic field effects is proved by comparison to 3D FEM results.

Finally, in Chapter 5, the dissertation's conclusions are provided, along with research ideas that can be investigated further in future study.

CHAPTER 2 INDUCTOR MODEL BY DISTRIBUTED CIRCUIT-BASED METHODS

Currently, the flux paths of magnetic devices are represented by lumped models with a limited number of circuit components. Their computing efficiency is a major advantage, and they are precise enough for some analyses in which full modelling of magnetic flux paths and internal behaviours is not required. With the help of analytical formulas that are included with the design data, these models are able to determine the equivalent components that correspond to the magnetic flux paths. These analytical formulas are almost accurate when it comes to depicting flux paths in the core, but they are not accurate when it comes to representing flux paths in the air, which are difficult to characterise. Consequently, they are incapable of adequately accounting for leakage fluxes between winding turns or fluxes that flow outside the core during saturation or fringing fluxes in circumstances where there are air gaps in the magnetic device.

Two essential techniques have been employed to improve the accuracy of flux path descriptions in the literature. The first method is to enhance analytical equations by estimating the total image of flow paths. The second approach is to define new elements that will aid in the description of fluxes. For example, [27] revised the MEC model for a specific type of inductor to take into consideration fringing and leakage fluxes, among other things. While this study improved accuracy, it is not widely applicable and is based on assumptions that are accurate only in this particular instance of the study.

In contrast to the exiting lumped element models, which portray the magnetic field of an inductor using only a few flux paths, this research uses a vast number of flux paths to depict the magnetic field's behaviour. In contrast to previous lumped parameter models in which the flux tubes defined in them only consider the flux direction in one direction, the approach described in this chapter for defining flux tubes, considers two perpendicular directions of flux paths in defining flux tubes. The proposed method in this chapter is a distributed circuit-based methodology for accurately modelling an inductor. This approach can be used to correctly describe magnetic fluxes in the core as well as those leaking into the air. Essentially, the primary contribution of this method is that it allows circuit simulators to use distributed models that are as accurate as those generated by finite element modelling.

This chapter presents a distributed method for detailed modelling of magnetic devices based on circuit-based methods. Our method employs meshing to discretize space into electric/magnetic circuits. Indeed, like FEM, the proposed method can provide a detailed geometrical description of magnetic flux distributions as well as model non-homogeneous materials with magnetic saturation. Due to the fact that each of the three existing methods for linking magnetic circuits with electric circuits outlined in section 1.1 has unique advantages and disadvantages, the proposed distributed procedure creates equivalent circuits using each of the three approaches.

The remainder of this chapter is organized as follows: in section 2.1, the principles of the proposed method are outlined for a simple case of an inductor. In this section, the model is divided into a limited number of cells to aid comprehension of the concept. The Hopkinosn analogy, the Buntenbach analogy, and the duality principle are used to derive equivalent circuits for the meshed model of the inductor. Section 2.2 contains a more extensive explanation of how to create models for an inductor, one with an air gap and one without, but with a customizable amount of meshes. Also, section 2.2 presents and discusses results for three phenomena: open-circuit and short-circuit as normal operating conditions, and ferroresonance as a transient phenomenon, and compares them to those obtained using a FEM solver.

2.1 Methodology

In this section, a single-phase shell-type inductor is investigated. It is supposed that the inductor is connected to a voltage source U_{in} through a resistance R_{in}. The schematic of the studied inductor is presented in Figure 2.1. In order to have a meshed model, the inductor has been subdivided into 18 identical cells where each cell is represented using an equivalent magnetic circuit. It can be observed that the flux paths have been only assumed in the horizontal and vertical directions.

2.1.1 Electromagnetic modeling by Hopkinson Analogy

Figure 2.2 shows the circuit of an elementary cell for Hopkinson analogy. In this circuit the reluctances R_u, R_d, R_l and R_l are given by

$$R_u = R_d = \frac{\left(\frac{W_y}{2}\right)}{\mu W_x W_z} \tag{2.1}$$

$$R_l = R_r = \frac{\left(\frac{W_x}{2}\right)}{\mu W_y W_z} \tag{2.2}$$

where W_x, W_y, and W_z denote the lengths of the flux tubes in the x, y, and z directions. Also μ is permeability of the flux tubes. To derive the values of magnetomotive force sources $\mathcal{F}_u$ and $\mathcal{F}_d$ in each cell, Ampere's law and the boundary conditions are applied. The Neumann boundary condition [68], must be imposed at the external sides of the inductor. The Neumann boundary condition can be fulfilled by eliminating the reluctances perpendicular to the exterior sides of the inductor. In Figure 2.1(a), dashed blue reluctances are used to show eliminated reluctances.

To apply Ampere's law, the values of magnetomotive force sources are chosen in a way that the sum of them in a closed loop should be equal with the ampere-turn passing through it (the total enclosed current for the loop). For instance, for the green loop shown in Figure 2.1(a), which encloses three turns of the winding, the sum of the magnetomotive forces is three times the current, which is equal to the ampere-turns passing through it.

To take the coupling between the electric circuit and the magnetic circuit into account, Faraday's law should be applied in the distributed form. Figure 2.1(b) demonstrates the schematic diagram for illustrating the total magnetic fluxes enclosed by each turn. From Figure 2.1, and based on Faraday's law, the voltages induced in each turn are given by

$$\begin{bmatrix} E_{AB} \\ E_{CD} \\ E_{EF} \\ E_{GH} \end{bmatrix} = -\frac{d}{dt}\left(\begin{bmatrix} 0 & 0 & 0 & 0 & 0 & 1 & 1 & 0 \\ 0 & 1 & 1 & 0 & 0 & 0 & 0 & 0 \\ 0 & 0 & 0 & 0 & 1 & 1 & 1 & 1 \\ 1 & 1 & 1 & 1 & 0 & 0 & 0 & 0 \end{bmatrix} \begin{bmatrix} \varphi_1 \\ \varphi_2 \\ \varphi_3 \\ \varphi_4 \\ \varphi_5 \\ \varphi_6 \\ \varphi_7 \\ \varphi_8 \end{bmatrix} \right) \tag{2.3}$$

where E_{AB}, E_{CD}, E_{EF} and E_{GH} are the induced voltages in the turns AB, CD, EF, and GH, respectively. Moreover φ_1, φ_2, φ_3,…, φ_8 are the magnetic fluxes for the magnetomotive forces displayed in Figure 2.1(a). The total induced voltage E_{tot} is found from the sum of loop voltages

$$E_{tot} = -\frac{d}{dt}(\varphi_1 + 2\varphi_2 + 2\varphi_3 + \varphi_4 + \varphi_5 + 2\varphi_6 + 2\varphi_7 + \varphi_8) \tag{2.4}$$

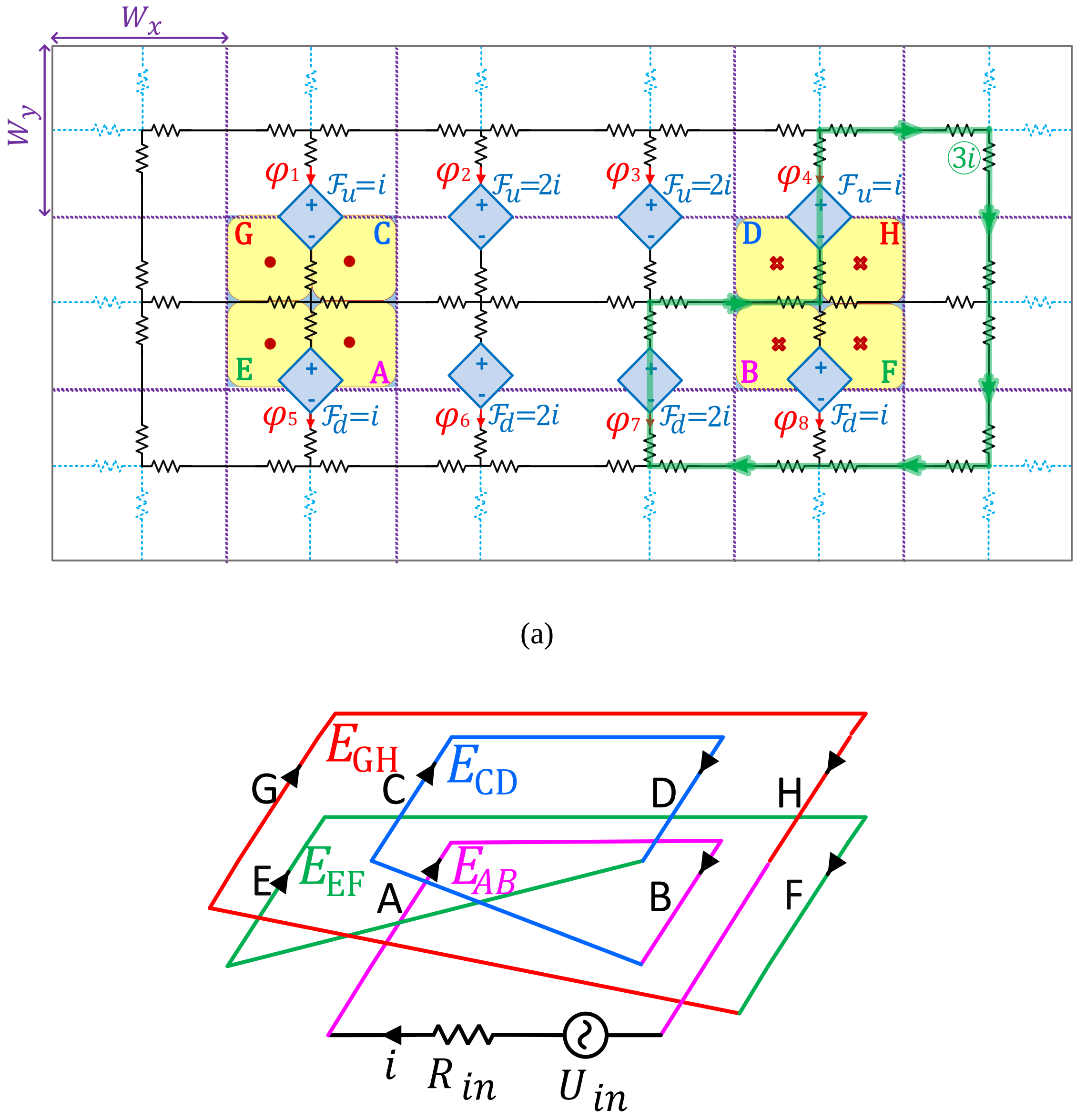

(a)

(b)

Figure 2.1 (a) Distributed magnetic circuit with magnetomotive forces, (b) schematic of inductor winding turns and external circuit

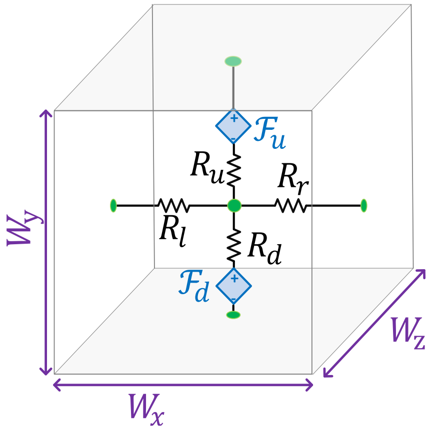

Figure 2.2 Circuit of the elementary cell in Hopkinson analogy

Finally, by considering the relations and laws mentioned above, the interface between the magnetic and electric circuits is derived as illustrated in Figure 2.3. The magnetic and electric circuits have been shown in black and blue, respectively. It is obvious that the sum of electromotive force sources distributed in the electric circuit is equal to E_{tot}. The resistance R_{tot} is equal to the sum of winding resistance R_w and external circuit resistance R_{in}. The current-controlled voltage sources have been applied to provide coupling between the magnetic and electric circuits. Each pair of current-controlled voltage sources in the equivalent circuit of Figure 2.3, is a specific type of mutator element: Type-2 L-R mutator. The schematic of the Type-2 L-R mutator was illustrated in Figure 1.2. Two coupled series R-L branches can be used to implement this type of mutator in EMT-type programs [11]. The values of self and mutual resistances and inductances associated with the two branches, are specified as follows

$$\begin{bmatrix} v_1 \\ v_2 \end{bmatrix} = \begin{bmatrix} 0 & 0 \\ N & 0 \end{bmatrix} \begin{bmatrix} i_1 \\ i_2 \end{bmatrix} + \begin{bmatrix} 0 & -N \\ 0 & 0 \end{bmatrix} \frac{d}{dt} \begin{bmatrix} i_1 \\ i_2 \end{bmatrix} \tag{2.5}$$

where N is the coupling factor of the mutator. The left part of the circuit shown in Figure 1.2, denotes the electric circuit and the right part denotes the magnetic circuit. Equation (2.5) is actually given by

$$\begin{bmatrix} E \\ \mathcal{F} \end{bmatrix} = \begin{bmatrix} 0 & 0 \\ N & 0 \end{bmatrix} \begin{bmatrix} i \\ \varphi \end{bmatrix} + \begin{bmatrix} 0 & -N \\ 0 & 0 \end{bmatrix} \frac{d}{dt} \begin{bmatrix} i \\ \varphi \end{bmatrix} \tag{2.6}$$

where E is electromotive force (EMF), $\mathcal{F}$ is the magnetomotive force (MMF) and φ is the magnetic flux. This equivalent circuit is demonstrated in the cells of Figure 2.3, which i is the current of the inductor. Furthermore, N is the coupling factor of the mutators.

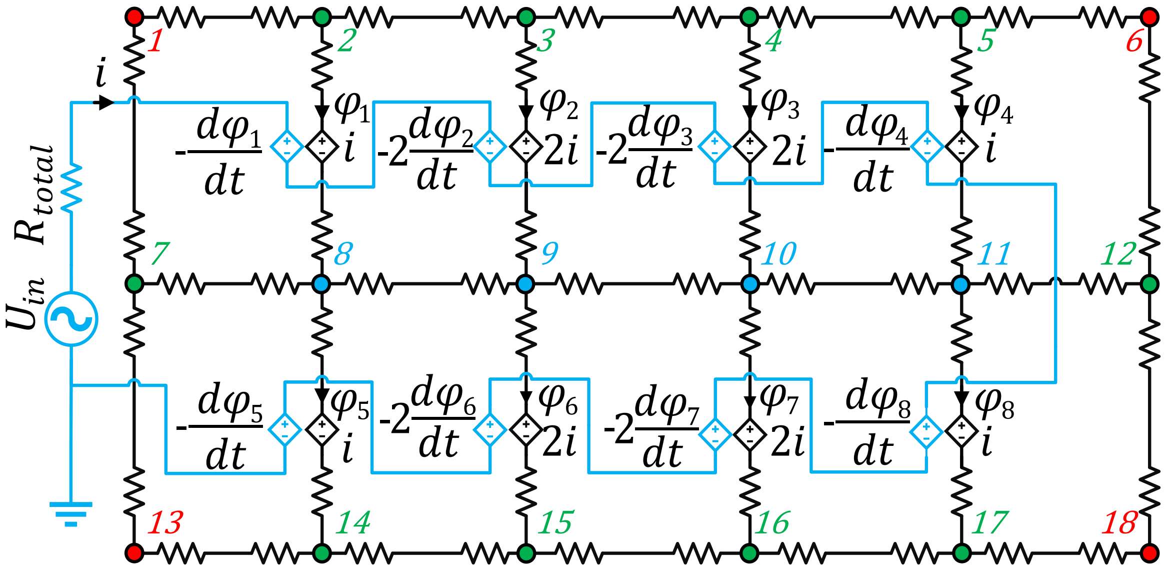

Figure 2.3 Distributed inductor model using Hopkinson analogy (including both magnetic and electric circuits and coupling between them)

2.1.2 Electromagnetic modeling by Buntenbach Analogy

To derive the equivalent circuit for the distributed Buntenbach analogy, the meshes and the nodes are the same as the meshes and the nodes for the equivalent circuit derived for Hopkinson analogy, but the resistances in Hopkinson analogy are replaced with capacitances. Additionally, for the coupling of the magnetic circuit with the electric circuit, another mutator termed Type-1 L-C is employed which was displayed in Figure 1.4.

In the equations of Type-1 L-C mutator, the values for resistors and inductors are set differently from (2.5) as

$$\begin{bmatrix}v_1\\v_2\end{bmatrix} = \begin{bmatrix}0 & -N\\N & 0\end{bmatrix}\begin{bmatrix}i_1\\i_2\end{bmatrix} + \begin{bmatrix}0 & 0\\0 & 0\end{bmatrix}\frac{d}{dt}\begin{bmatrix}i_1\\i_2\end{bmatrix} \tag{2.7}$$

Similar to equation (2.6) for Type-2 L-R, Type-1 L-C mutator couples the magnetic part and the electric part in this way

$$\begin{bmatrix}E\\\mathcal{F}\end{bmatrix} = \begin{bmatrix}0 & -N\\N & 0\end{bmatrix}\begin{bmatrix}i\\d\varphi/dt\end{bmatrix} + \begin{bmatrix}0 & 0\\0 & 0\end{bmatrix}\frac{d}{dt}\begin{bmatrix}i\\d\varphi/dt\end{bmatrix} \tag{2.8}$$

The complete Buntenbach circuit is now demonstrated in Figure 2.4.

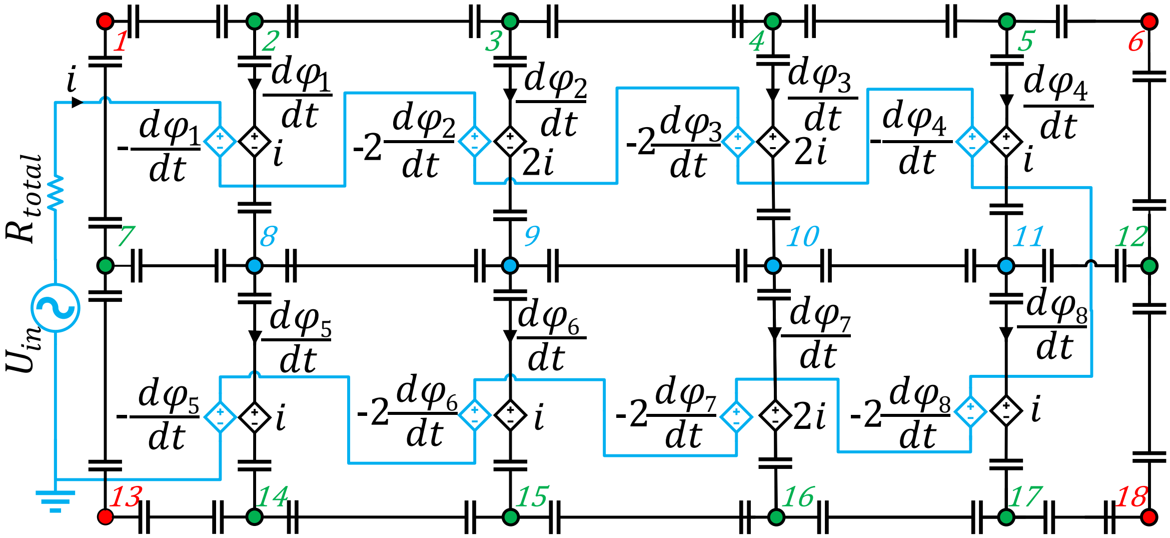

Figure 2.4 Distributed inductor model using Buntenbach analogy (including both magnetic and electric circuits and coupling between them)

2.1.3 Electromagnetic modeling by duality principle

It can be observed that the graph of the magnetic circuit in Figure 2.3 is a planar graph, and a dual circuit can be obtained for it [69]. Therefore, by considering all the rules mentioned in section 1.1.3, the dual circuits for various cells (sections) of the magnetic circuit are derived, as shown in Figure 2.5 and Figure 2.6.

As illustrated in Figure 2.5 and Figure 2.6, the cells, comprised of resistors that have a common node, are converted to dual cells, comprised of inductances enclosed in a mesh. Besides, as demonstrated in Figure 2.6 the controlled voltage source of the magnetic side in the Type 2 L-R mutator, the circuit of Figure 2.6(a) is converted to the controlled current source, the circuit of Figure 2.6(b). The relations between the two sides of the derived circuit, in Figure 2.6(b), are given by

$$\begin{bmatrix} i_1 \\ v_1 \end{bmatrix} = \begin{bmatrix} {}^{1}\!/_{N} & 0 \\ 0 & N \end{bmatrix} \begin{bmatrix} i_2 \\ v_2 \end{bmatrix} \tag{2.9}$$

It is apparent that (2.9) describes the equations of an ideal transformer with ratio *N:1* (or power-scalor). Accordingly, for deriving the duality circuit, the coupling element is modeled using an ideal transformer, as depicted in the circuit of Figure 2.6(c).

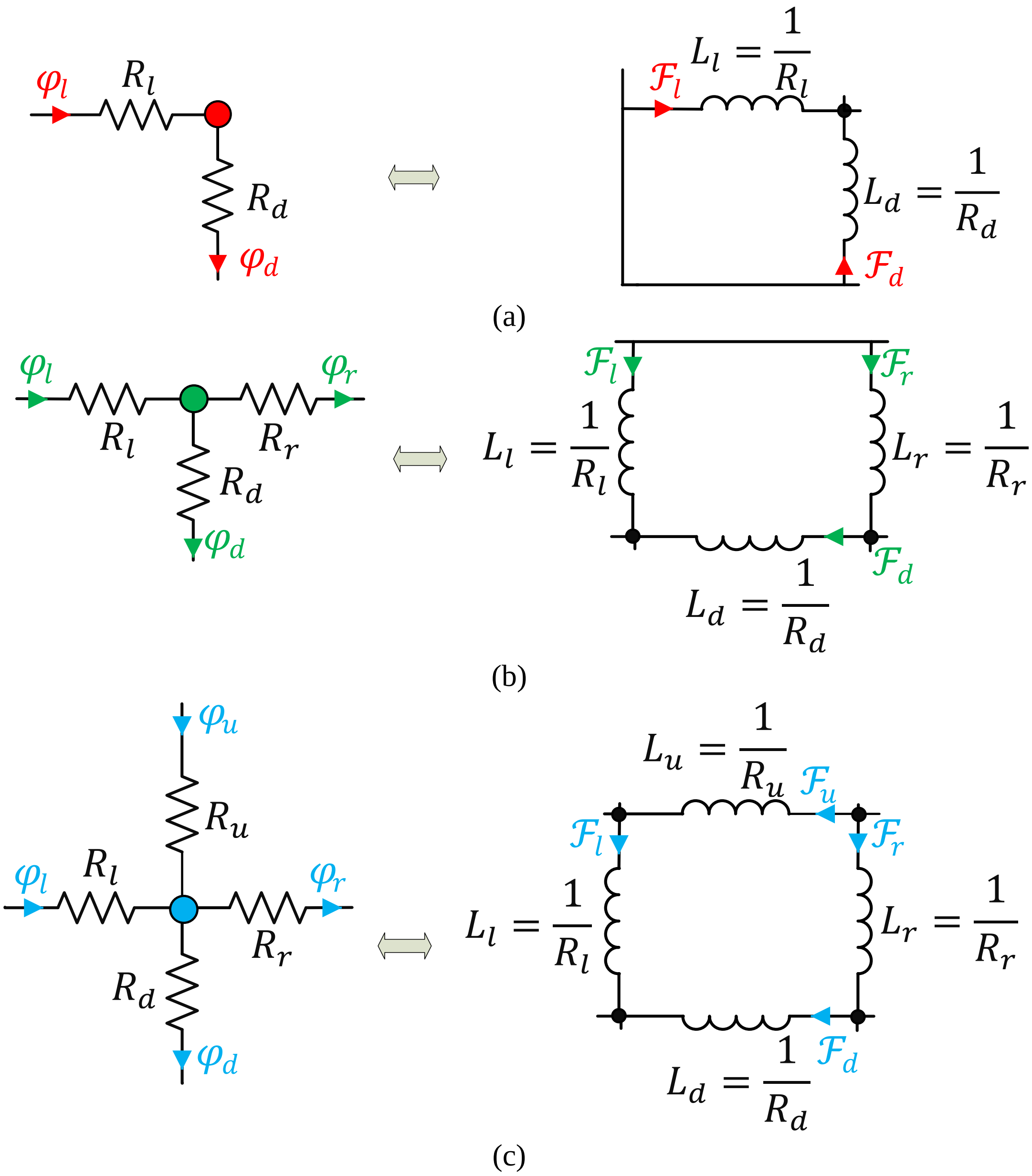

Figure 2.5 Graphical derivation of the dual circuit of the magnetic circuit for three types of cells, excluding coupling elements

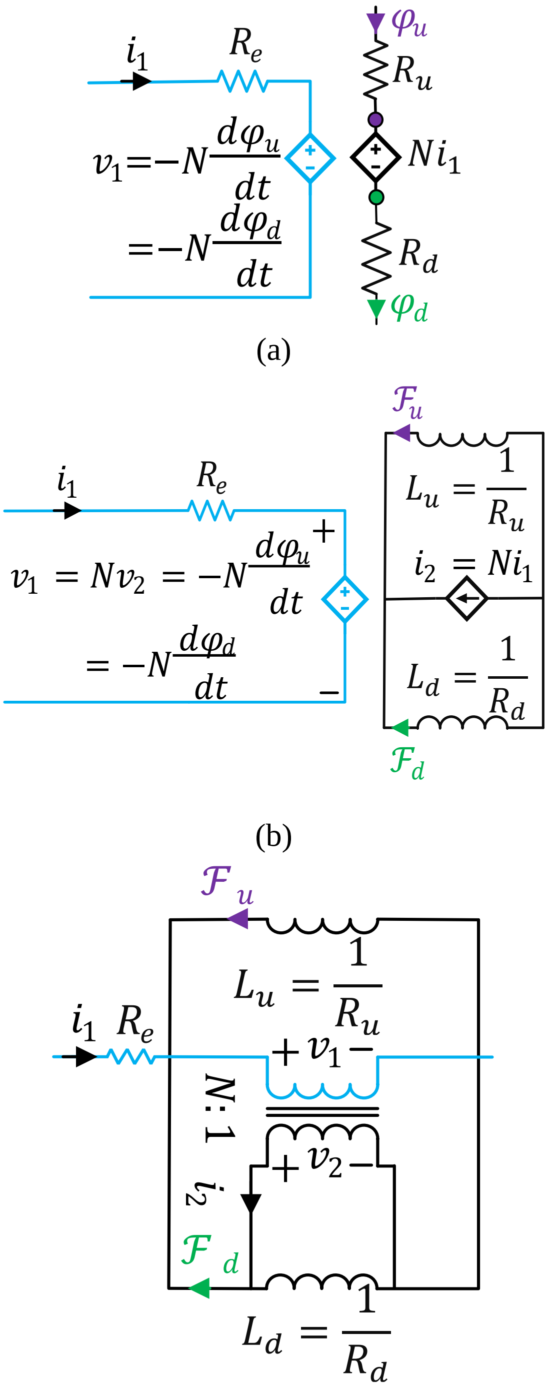

(a)

(b)

(c)

Figure 2.6 Graphical derivation of the dual circuit of the magnetic circuit for one type of cell, including coupling elements

Figure 2.7 presents the distributed duality-based circuit resulted from the distributed resistive circuit shown in Figure 2.3. To achieve the distributed duality-based model, the dual circuits for each cell of Figure 2.3, numbered from 1 to 18, are derived using the procedures previously mentioned. The duality-based circuits regarding each cell are presented in Figure 2.7 with the same number as their dual cells in the circuit of Figure 2.3. The resulting duality-based circuits are connected to each other based on the rule that the nodes in the magnetic circuit are converted to the meshes in the electric circuit and vice versa.

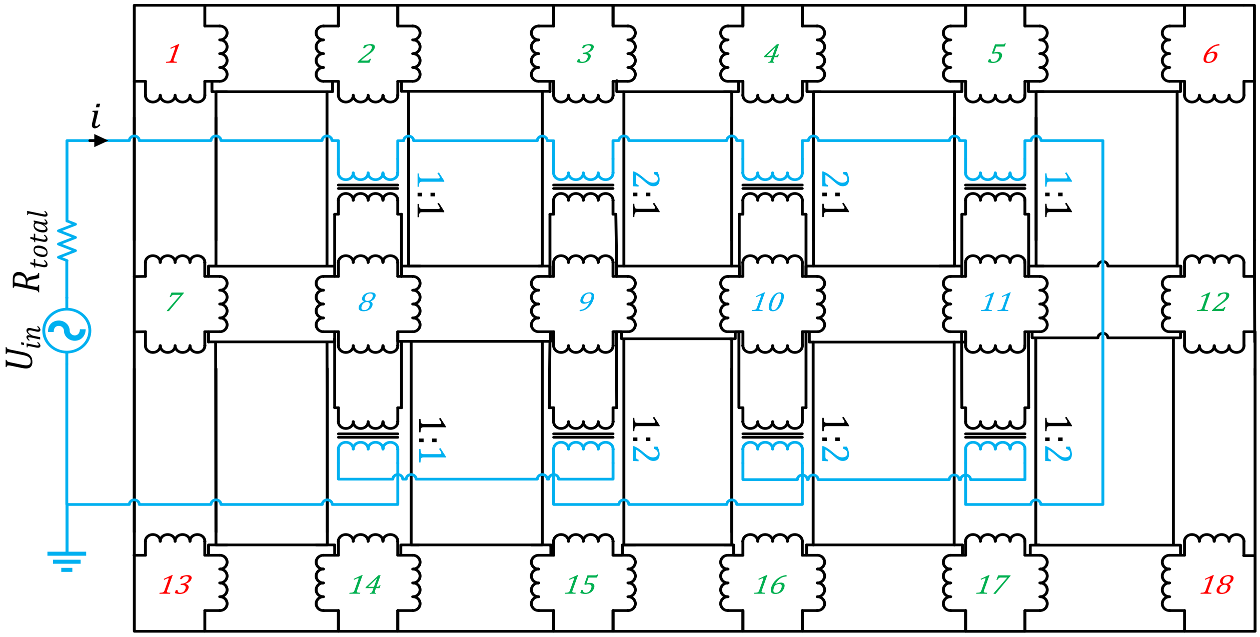

Figure 2.7 Distributed duality-based inductor model, including both magnetic and electric circuits and coupling between them

2.2 Validation

In this section, the HBD-circuits introduced in the previous section are improved and studied for an inductor. Its winding includes 100 turns. Two different core designs are considered: without air gap (gapless core) and with an air gap (gapped core). The dimensions of the core and the winding are shown in Figure 2.8. The winding material is copper, and the core material is soft iron.

The two main goals of this section are to compare the results of HBD-circuits against each other and against FEM results. In this section, the EMTP software is employed to implement HBD-circuits and the COMSOL Multiphysics 5.4 is employed to solve FEM.

Here, firstly, two examples of the inductor current waveforms for the gapless and the gapped core inductors are illustrated. Secondly, the magnetic field intensity curves regarding a sample point placed in the core are exhibited for both gapless and gapped core inductors. The results are obtained for two different numbers of meshes: 72 and 1152. Thirdly, the voltage-current characteristics observed from the terminals of the gapless and gapped core inductors are presented for two mentioned number of meshes.

To obtain the results, for both gapless and gapped core inductors, a 60 Hz sinusoidal voltage source is applied across the winding, and the steady-state voltage and current waveforms of the inductor are derived. For both inductors, the resistance R_{tot} is equal to 0.032 Ω (the DC resistance of the inductor winding) and the simulation time-step is 10 μs. The limit in this case is due to the complexity of the extra-large nonlinear system and the underlying solution process to achieve convergence. It is worth mentioning that this test setup is only employed to perform numerical comparisons for HBD-circuits.

In the previous section, the number of elements was selected as a fixed small value to provide a simple explanation. But, in FEMs, the number of meshes can be varied and adjusted according to the frequency of the phenomena, and the dimensions of the device. Since the distributed circuit-based approaches must have a strong resemblance to FEM, they must be flexible to mesh sizing and numbering. In the following, an adjustable meshing procedure is explained.

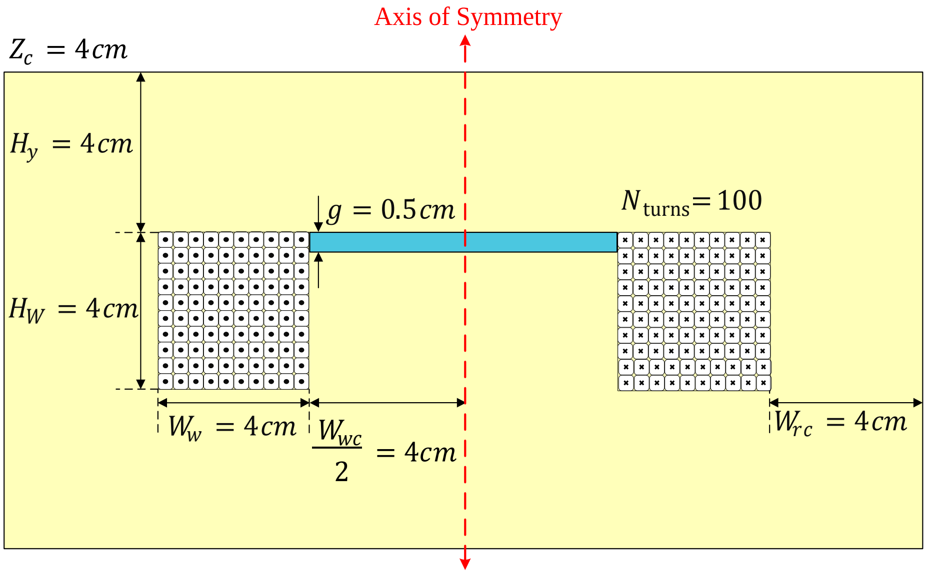

Figure 2.8 Cross-section of the gapped inductor

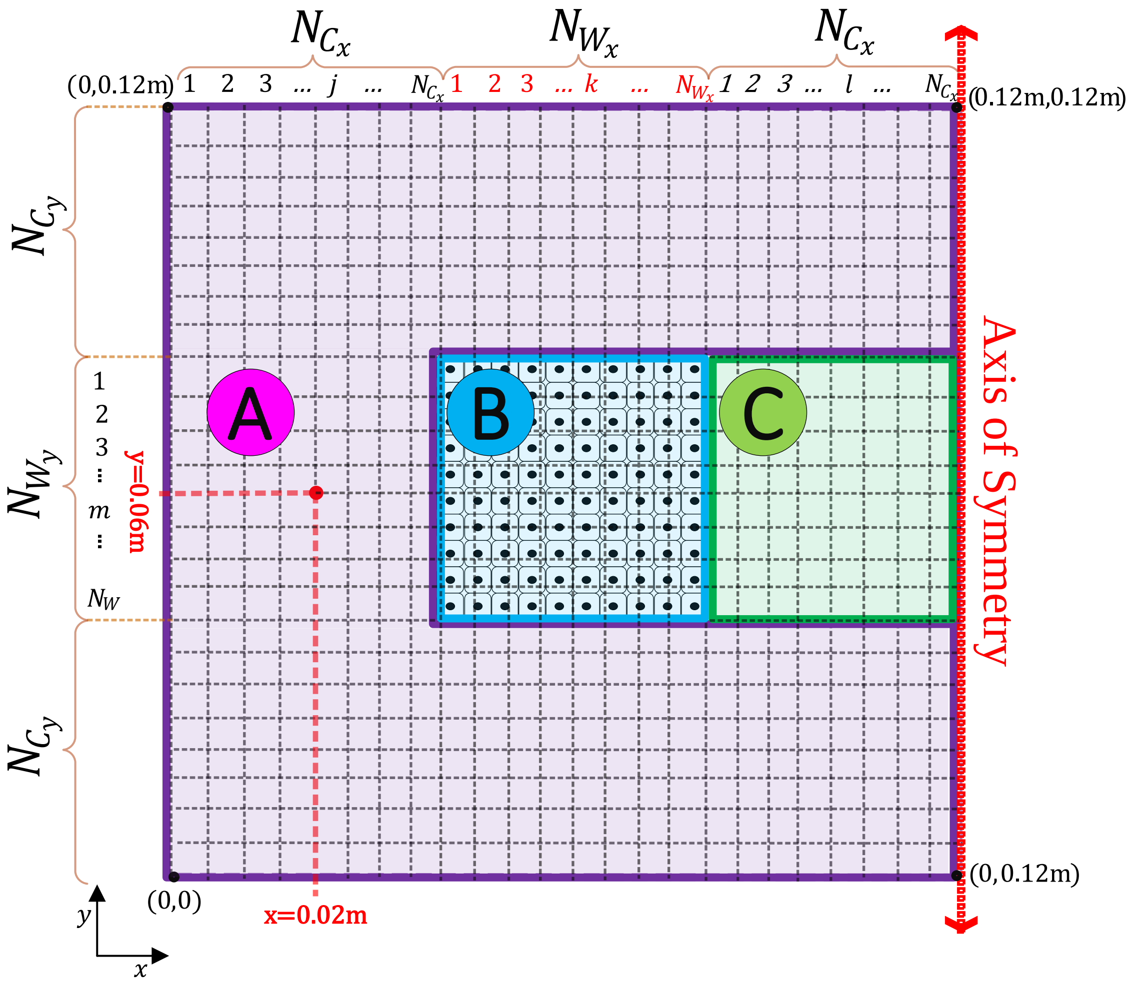

Figure 2.9 Cross-section of left half of the inductor

In this case study, since there is a vertical symmetry, the size of the problem can be reduced to half, as illustrated in Figure 2.9. In this figure, N_{W_x} and N_{W_y} are the numbers of meshes in the horizontal and vertical directions of part B (winding). Also, N_{C_x} and N_{C_y} are the numbers of meshes in the horizontal and vertical directions of part C (middle column of the core). Besides, HBD-circuits are constituted of three general different types of cells called type-A, type-B, and type-C, exposed in Figure 2.9. Type-A cells are only comprised of the nonlinear RLC elements. Type-B cells are comprised of the linear RLC elements and the coupling elements. For gapless inductor, Type-C cells are formed of the nonlinear RLC elements and the coupling elements. But, for the gapped core inductor, based on the meshing, Type-C cells can be formed of the linear or nonlinear RLC elements and the coupling elements. Figure 2.10 shows the equivalent resistive, capacitive, and inductive circuits regarding the three mentioned types.

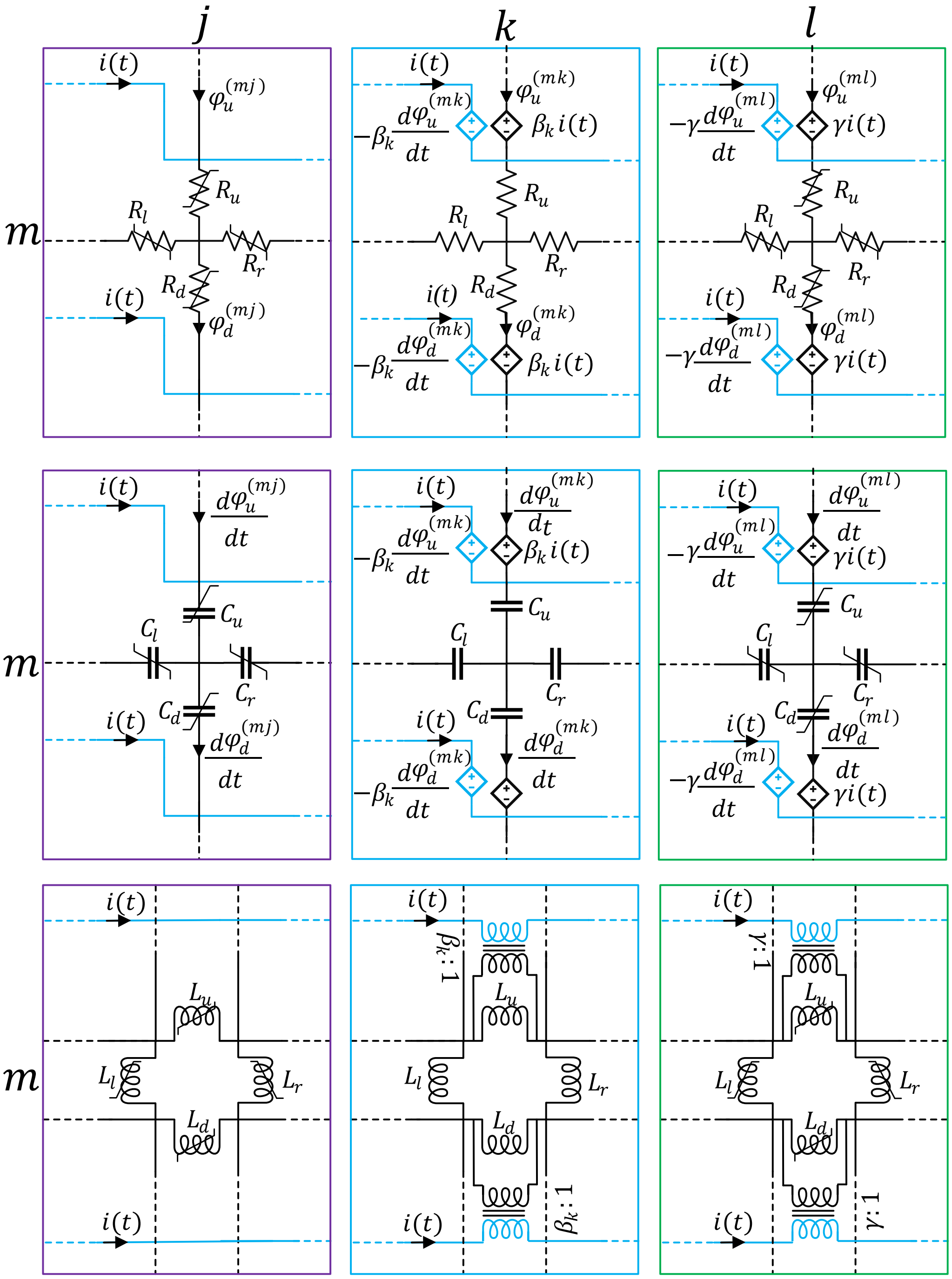

(a) Part A of Figure 2.9 (b) Part B of Figure 2.9 (c) Part C of Figure 2.9

Figure 2.10 Distributed resistive, capacitive, and inductive circuits regarding three sample cells of the meshed inductor model shown in Figure 2.9

First, the linear and nonlinear RLC elements are calculated. The values of the RLC linear elements are determined and correlated by

$$R = \frac{1}{C} = \frac{1}{L} = \frac{l}{\mu_0 S} \tag{2.10}$$

where l and S are the mean length and cross-section regarding the flux path represented by the element, and μ_0 is the magnetic permeability of air.

Table 2.1 Piecewise-linear curve (first quadrant) presenting soft iron

number	$\boldsymbol{B[T]}$	$\boldsymbol{H\left[\frac{kA}{m}\right]}$	**number**	$\boldsymbol{B[T]}$	$\boldsymbol{H\left[\frac{kA}{m}\right]}$	**number**	$\boldsymbol{B[T]}$	$\boldsymbol{H\left[\frac{kA}{m}\right]}$
1	1.0	0.66	6	1.5	5.43	11	2.0	61.21
2	1.1	1.07	7	1.6	7.96	12	2.1	111.40
3	1.2	1.71	8	1.7	12.30	13	2.2	188.50
4	1.3	2.46	9	1.8	20.46	14	2.3	267.93
5	1.4	3.84	10	1.9	32.17	15	2.4	347.51

To represent the nonlinear RLC elements of type-A and type-C cells, the magnetizing curve is represented by a piecewise linear function with 15 linear segments (Table 2.1) which is the characteristic of the material (soft iron) defined in the materials library in COMSOL Multiphysics. The incremental magnetic relative permeability μ_p of each segment of the piecewise linear curve is characterized as the slope between changepoints p and $p-1$

$$\mu_p = \frac{1}{\mu_0} \frac{B_p - B_{p-1}}{H_p - H_{p-1}} \tag{2.11}$$

for $p = 1, 2, \ldots, 15$. As a result, nonlinear resistance curves, nonlinear capacitance curves, and nonlinear inductance curves are modeled using piecewise linear representation with 15 segments. The incremental resistance R_p, capacitance C_p, and inductance L_p of segment p of the piecewise-linear curve are specified as the slopes between changepoints p and $p-1$

$$R_p = \frac{v_p - v_{p-1}}{i_p - i_{p-1}} \tag{2.12}$$

$$C_p = \frac{q_p - q_{p-1}}{v_p - v_{p-1}} \tag{2.13}$$

$$L_p = \frac{\varphi_p - \varphi_{p-1}}{i_p - i_{p-1}} \tag{2.14}$$

where R_p, C_p and L_p are given by (2.10), except that the value of the permeability μ, is set equal to μ_p.

So far, it has been assumed that each mesh has been constituted of one material. But based on the size and position of the mesh, it is possible that it is composed of different materials with different relative permeability values. An example of a nonuniform cell composing of two different materials with relative permeabilities of μ_1 and μ_2 has been demonstrated in Figure 2.11. The lengthwise averages of permeability regarding this type of cell in horizontal and vertical directions respectively named $\overline{\mu_h}$ and $\overline{\mu_v}$ are given by

$$\overline{H_h} = H_{h_1} = H_{h_2} \tag{2.15}$$

$$\varphi_h = \varphi_{h_1} + \varphi_{h_2} \tag{2.16}$$

$$\overline{B_h}\left(S_{h_1} + S_{h_2}\right) = B_{h_1} S_{h_1} + B_{h_2} S_{h_2} \tag{2.17}$$

$$\overline{\mu_h} = \frac{\overline{B_h}}{\overline{H_h}} = \mu_1\left(\frac{h_1}{h_1 + h_2}\right) + \mu_2\left(\frac{h_2}{h_1 + h_2}\right) \tag{2.18}$$

$$\overline{B_v} = B_{v_1} = B_{v_2} \tag{2.19}$$

$$F_v = F_{v_1} + F_{v_2} \tag{2.20}$$

$$\overline{H_v}(h_1 + h_2) = H_{v_1} h_1 + H_{v_2} h_2 \tag{2.21}$$

$$\overline{\mu_v} = \frac{\overline{B_v}}{\overline{H_v}} = \frac{1}{\frac{1}{\mu_1}\left(\frac{h_1}{h_1 + h_2}\right) + \frac{1}{\mu_2}\left(\frac{h_2}{h_1 + h_2}\right)} \tag{2.22}$$

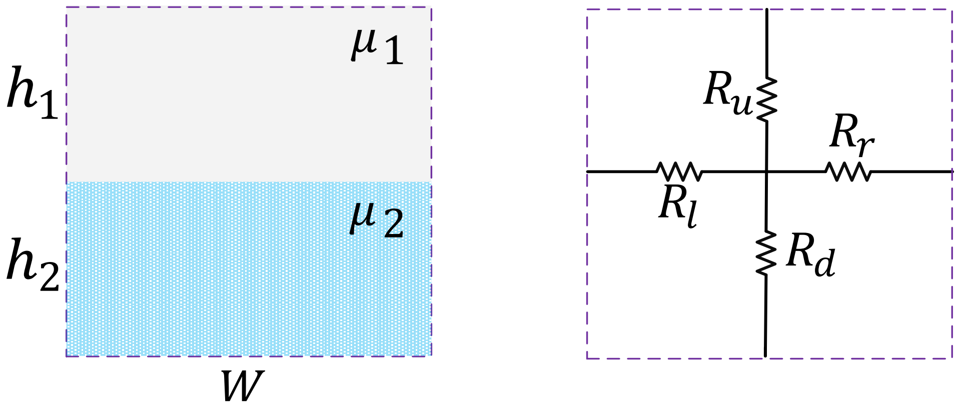

Figure 2.11 Nonuniform cell

The parameters β_k and γ associated with the coupling elements (Type-2 L-R mutator, Type-1 L-C mutator, and ideal transformer), for the circuits presented Figure 2.10(b) and (c), are given by

$$\beta_k = \frac{50k - 25}{N_{W_y} N_{W_x}} \tag{2.23}$$

$$\gamma = \frac{50}{N_{W_y}} \tag{2.24}$$

After implementing the HBD-circuits with 72 and 1152 in EMTP, their performances are verified as follows.

Firstly, for both gapless core and gapped core inductors, the currents resulting from HBD-circuits are compared with each other for the case that there are 1152 meshes. The results are also compared with the results from FEM with 3778 meshes. The voltage source is set to 130 volts for gapless core inductor and it set to 200 volts for gapped core inductor. Obtained results for both inductors are illustrated in Figure 2.12 and Figure 2.13, respectively.

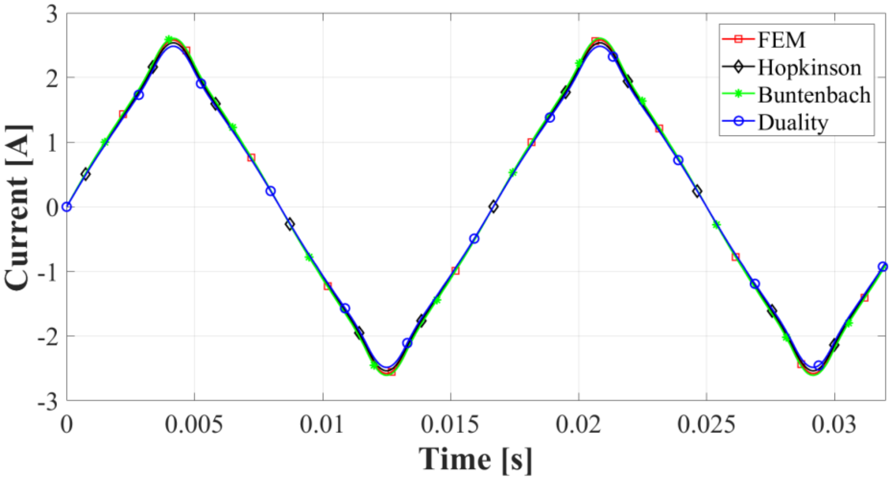

Figure 2.12 Gapless core inductor current i for HBD-circuits (1152 meshes) and FEM (3778 elements), during the nonlinear condition

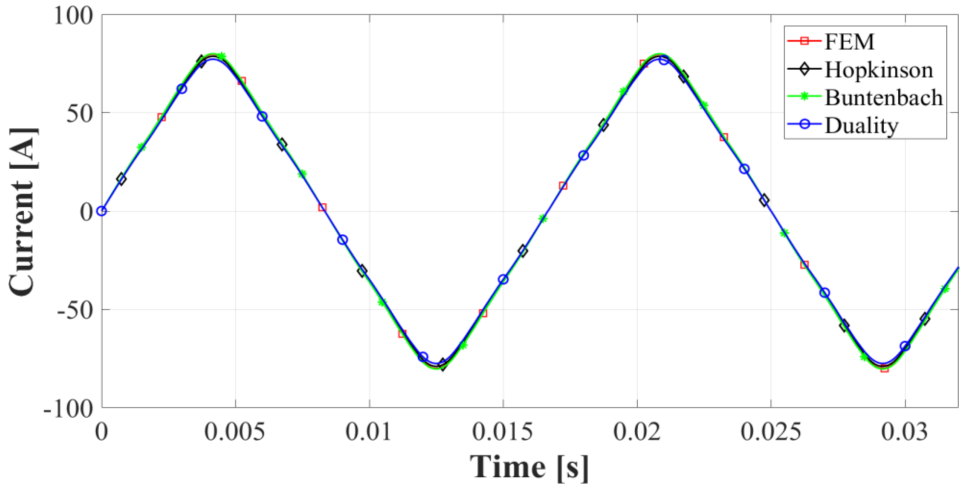

Figure 2.13 Gapped core inductor current i for HBD-circuits (1152 meshes) and FEM (3778 meshes) during the nonlinear condition

Secondly, as mentioned in the introduction, similar to FEM, HBD-circuits are able to represent the internal behavior of magnetic devices. For instance, as an advantage over topological transformer models and magnetic equivalent circuit-based models, the HBD-circuits can present local magnetic saturation. In this section, the magnetic field intensity regarding a local point are obtained for HBD-circuits with 1152 meshes and FEM with 3778 meshes. These results are derived for a point in the middle of the left column which has coordinates $(0.02\mathrm{m}, 0.06\mathrm{m})$, as illustrated in Figure 2.9. To present local magnetic saturation for gapless core and gapped core inductors, input voltage sources are set to 130 and 200 volts, respectively. The simulation results illustrating local saturation regarding both gapless and gapped core inductors are demonstrated in Figure 2.14 and Figure 2.15, respectively.

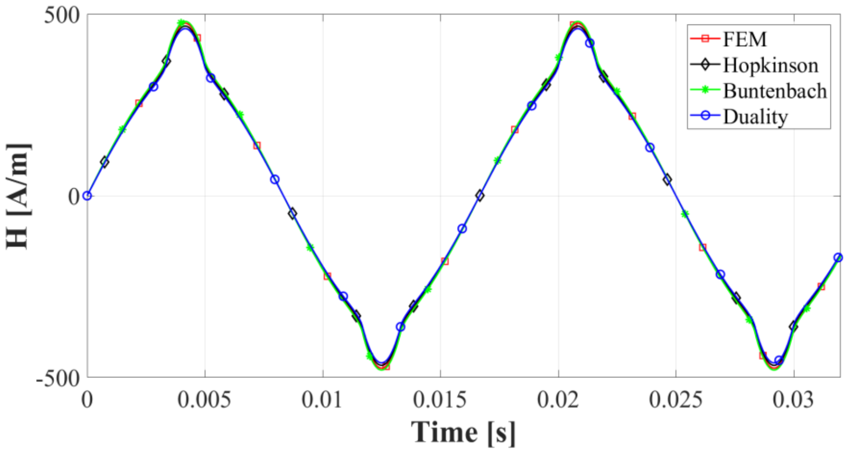

Figure 2.14 Magnetic field intensity H regarding a point of the gapless core with coordinates $(0.02m, 0.06m)$ during magnetic local saturation

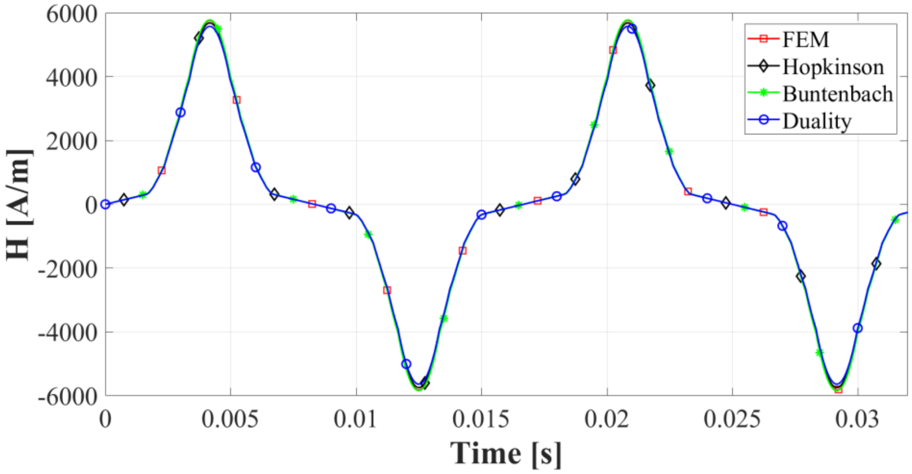

Figure 2.15 Magnetic field intensity H regarding a point of gapped core with coordinates $(0.02m, 0.06m)$ during magnetic local saturation

Finally, voltage-current characteristics, viewed from the terminals of the both inductors, obtained from HBD-circuits, are compared to those obtained from FEM in 2D. In the case of the gapless core inductor, the comparisons for two different numbers of meshes are shown in Figure 2.16 and Figure 2.17. Also, in the case of the gapped core inductor, the same comparisons have been illustrated in Figure 2.18 and Figure 2.19. In all results the number of meshes for FEM model equals 3778.

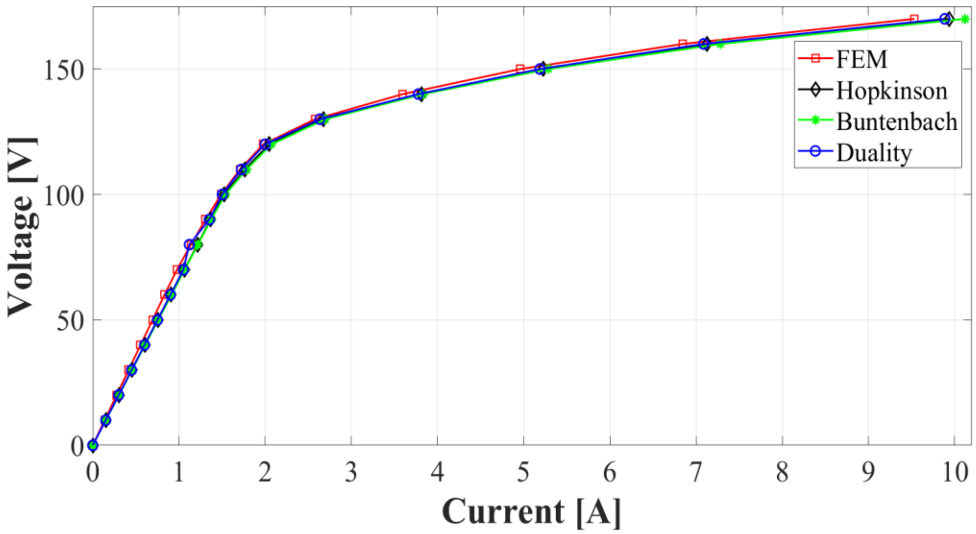

Figure 2.16 Voltage-current characteristics viewed from the terminals of the gapless core inductor (HBD-circuits with 72 meshes)

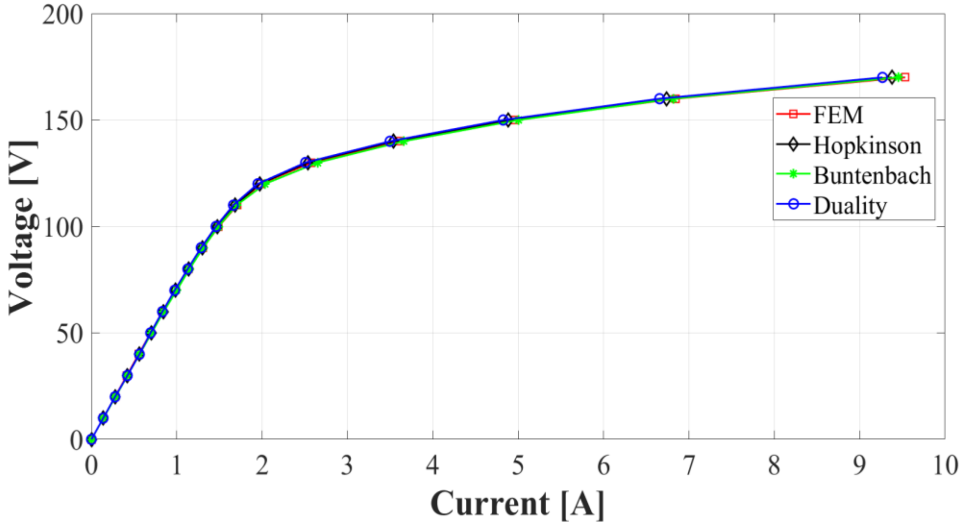

Figure 2.17 Voltage-current characteristics viewed from the terminals of the gapless core inductor (HBD-circuits with 1152)

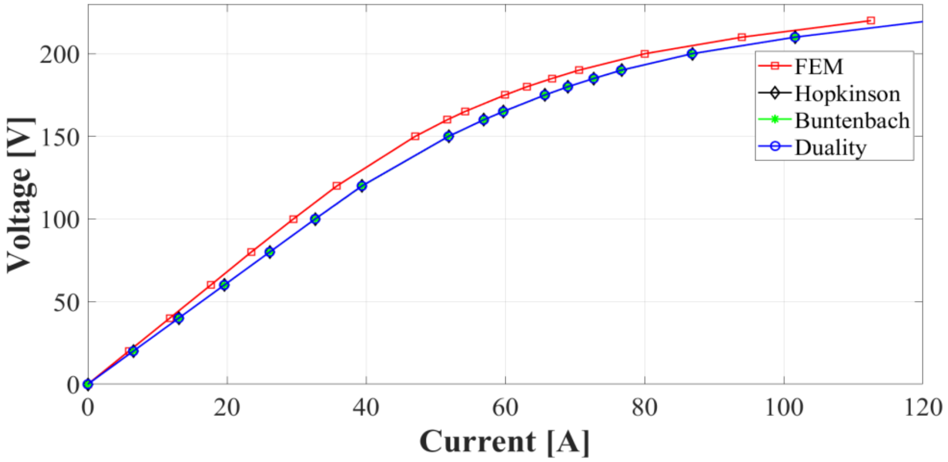

Figure 2.18 Voltage-current characteristics viewed from the terminals of the gapped core inductor (HBD-circuits with 72 meshes)

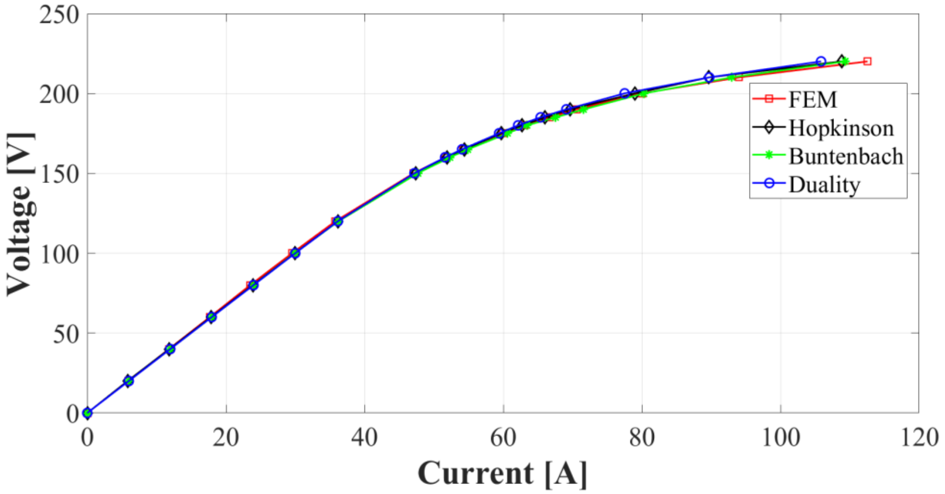

Figure 2.19 Voltage-current characteristics viewed from the terminals of the gapped core inductor (HBD-circuits with 1152 meshes)

It is observed that HBD-circuits are providing similar results. This is a significant achievement given the very large-scale nonlinear circuits solved in EMTP. The small differences are mainly due to numerical implementation details for nonlinear inductance and nonlinear capacitance in the Newton solution method employed in EMTP.

To provide validation for the accuracy of HBD-circuits, the normalized root mean square error (nRMSE) is applied on the voltage-current characteristic derived by each method. The nRMSE results for both gapless and gapped core cases are presented in Table 2.2, it can be concluded that

HBD-circuits give accurate results in comparison with FEM. In addition, it is observed that the effect of increasing the meshes on reducing the error is greater in the gapped core inductor. It is due to the fact that for the gapped core case which magnetic flux fringing out into the air, a greater number of meshes is needed to accurately present magnetic flux paths along the air gap and the core area in the vicinity of air gap.

Table 2.2 Accuracy analysis for HBD-circuits

Core type	**Error (%)**			
	Gapless Core		**Gapped Core**	
Mesh size	72	1152	72	1152
Hopkinson	6.18	1.13	9.22	1.52
Duality	6.12	1.19	9.17	1.59
Buntenbach	6.15	1.16	9.19	1.67

The key advantage of HBD-circuits over FEM is their computing speed, which is attributable to the fact that they require fewer elements and solve equations that are fundamentally less complicated. In fact, they are faster even when the number of elements is the same, as demonstrated in Figure 2.20, where the number of elements in FEM is 1102 and 1150 for gapped core and gapless core cases, respectively, and HBD circuits have 1152 elements in both cases. Simulations were run for 32 ms with a 1 μs time step for both linear and saturated operation conditions. For linear operation condition, HBD-circuits are around 30 times faster than FEMs, and for saturated condition with a high degree of nonlinearity, HBD circuits are around 15 times faster than FEM. However, for gapped core inductor in saturated condition, Hopkinson is about 10 times faster and Buntenbach and Duality are about 4 times faster than FEM.

HBD-circuits outperform FEM in all circumstances, with Hopkinson being the fastest of the three. This is due to the fact that Buntenbach and Duality have more differential equations than Hopkinson. It is worth noting that the number of elements in FEM and HBD-circuits are considered to be the same in Figure 2.20, only to compare the methods. However, to achieve a certain degree of accuracy, the number of elements in FEM must typically be set larger than the number of HBD elements, causing FEM to run much slower. In addition, as noted in the introduction, to use FEM to model magnetic devices in the power system, the indirect coupling method is commonly used, which slows them down even more. HBD-circuits, on the other hand, do not have these limits, and their speed advantages reveal themselves in these cases better.

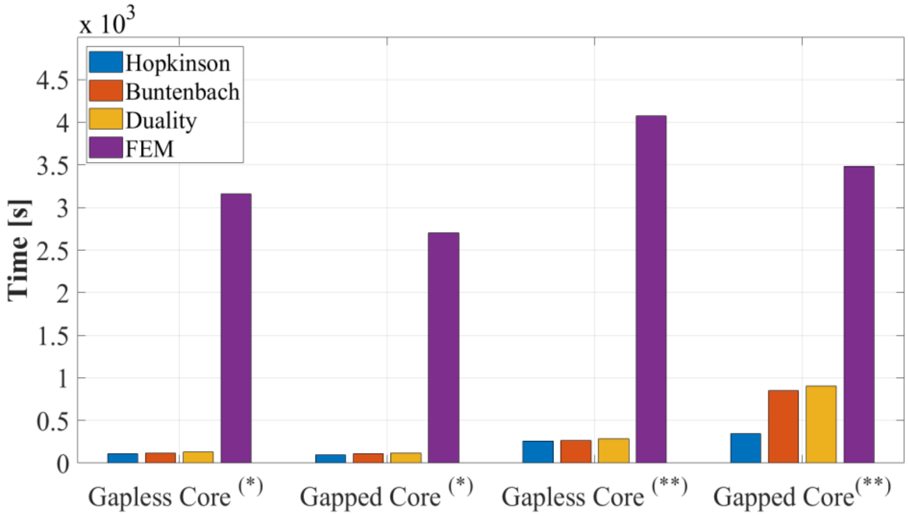

(*) : Linear operating condition
(**) : Saturated operating condition

Figure 2.20 HBD-circuits vs. FEM in terms of computation time

As it was mentioned in introduction, HBD-circuits can be used to study the effect of the external electrical network on the internal behavior of electromagnetic devices. As the final validation example, ferroresonance as a nonlinear phenomenon in the power system, is modeled using HBD-circuits. A ferroresonance circuit consisting of the gapped core inductor connected in series with a capacitance ($C = 9.82\,\mu F$) and a voltage source ($U_{in} = 100\cos(\omega t)$), is used to study ferroresonance by HBD-circuits and FEM. Figure 2.21 shows that the results of HBD-circuits with 1152 meshes and FEM with 3778 elements are remarkably similar. Studying different electromagnetic transient phenomena using HBD-circuits is desirable for future work.

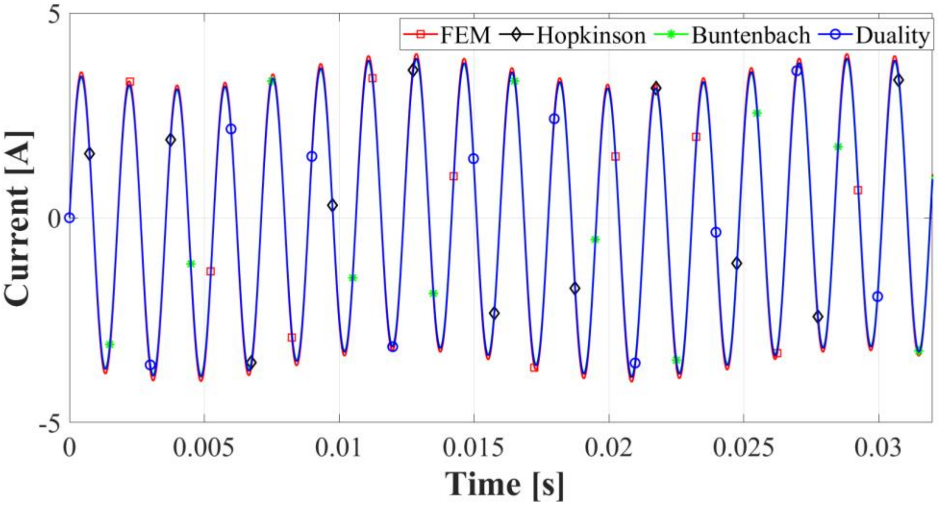

Figure 2.21 Inductor Current modeled by HBD-circuits and FEM during ferroresonance

2.3 Conclusion

In this study, three circuit-based methods named HBD-circuits were created in a distributed form for accurately modelling magnetic devices in EMTP. These methods are based on the Hopkinson analogy, the Buntenbach analogy, and the duality principle. The proposed HBD-circuits were utilised to model two inductors: one inductor with no air gap in its core (gapless core inductor) and one inductor with an air gap in its core (gapped core inductor). For both inductor cases, HBD-circuits were compared to one another as well as to FEM in terms of accuracy and computation speeds.

With the use of HBD-circuits, it was discovered that it was possible to achieve high levels of accuracy in showing both the external and internal behaviour of inductors. To represent the external behaviour of the inductors, HBD-circuits and FEM were used to determine the voltage-current characteristic observed at the inductors' terminals.

Additionally, in order to better depict the internal behaviour, the flux distribution over the core calculated using HBD-circuits was compared to the flux distribution derived using FEM. Furthermore, even when the number of components is huge, these techniques outperform FEM in terms of computational speed.

Finally, ferroresonance phenomenon in a circuit with an inductor was studied in EMTP while the inductor was represented by HBD-circuits, and the same circuit was implemented in COMSOL while the inductor was modelled by FEM. The results are consistent with one another, revealing that HBD-circuits can exhibit inductor behaviour not only in steady state, but also in transient conditions.

CHAPTER 3 TRANSFORMER MODEL BY DISTRIBUTED CIRCUIT-BASED METHODS

The FEM is the first choice when it comes to modelling transformers with high accuracy and having details on internal behaviour. Additionally, FEM may enable multi-physics modelling of transformers, allowing analysts to study, for example, the effect of internal faults on the temperature of various parts of a transformer [70]. However, as previously stated in Chapter 1, FEM cannot be used to study the transformer in a large network, and it is not possible to see the effect of the large network on the internal behaviour of the transformer and vice versa. Furthermore, Chapter 1 discussed how direct and indirect field-circuit coupling solutions can be used to generate a detailed model of magnetic devices in a network (see [25] as an example for modeling the transformer). However, it was emphasized that coupling solutions face several numerical issues, the majority of which are time demanding. In addition, it was said that power system analysts prefer circuit-based methods to simulate magnetic devices in the network, and that none of the coupling methods indicated above are preferred by them.

Currently, topological transformer models known as physically meaningful models are commonly employed in EMT-type software. These models are derived based on the principle of duality, which yields an equivalent electric circuit analogous to the reluctance model. Leakage inductances between windings are represented in these models by mutually coupled inductors, whose self and mutual inductances are obtained from short-circuit test data. For transformers with more than two windings, a large number of short-circuit tests are necessary, which can be time-consuming and impracticable. Furthermore, utilizing this method to study internal faults in transformers necessitates inter-turn fault tests, which are extremely difficult to be carried out. To avoid the need for short-circuit tests, Lambert et al. [71] used the analytical method proposed in [72, 73], to calculate the short-circuit impedances between winding pairs directly from geometrical data. The proposed method could closely reproduce experimental measurements from single-phase and three-phase transformers. However, the air flux paths during saturated operating conditions or zero-sequence flux paths have not been yet modeled accurately in topological transformer models. This is mainly due to the fact that these models represent magnetic devices by a limited number of flux tubes. To address this problem, some study has been conducted to see if FEM can be used to bring the values of electric elements in models closer to reality. For example, in [74], the authors used

FEM to improve the relations for determining air core inductance in topological transformer models and introduced a correction factor by comparing the findings to 2D-FEM results. In [75],the off-core inductances of topological transformer model were estimated using 2D-FEM. Even though topological transformer models are more accurate than other available transformer models in EMT-type software, they do not appear to be good enough in studies that need accurate flux path representation.

This chapter improves HBD-circuits proposed in Chapter 2 for more accurate transformer modelling. This proposed transformer model is like (follows the same approach) the inductor model presented in Chapter 2. It can provide a greater number of flux tubes to represent magnetic flux tubes than other mentioned circuit-based methods used in EMT-type software. As a result, both magnetic flux paths in the core and in the air can be accurately represented during various transformer operating conditions, such as normal operation, inrush currents, short-circuit, geomagnetically induced currents, ferroresonance, and harmonics. The proposed approach can produce a detailed representation of the transformer that is quite similar to FEM and can be used in EMT-type software and consequently to examine the transformer in a network that may contain a large number of power components. In addition, this method has the benefit of direct coupling methods, which simultaneously solves magnetic equivalent circuits and electric circuits of the network. As was mentioned in the previous chapter, recently, in [67], Naïdjate et al. proposed mesh modelling of transformers using MEC in EMTP by establishing intermediate circuits and defining new elements. Even though [67] has been able to provide both magnetic field distribution in the transformer and voltage distribution along each winding, they are complex, and modelers prefer methods that can be built utilizing the capabilities already accessible in EMTP-type tools. The models proposed in this chapter are similar to the inductor models proposed in Chapter 2 .The methodology does not necessitate the creation of new elements or complex intermediate circuits.

In addition, these models are able to simulate internal faults in transformers. Existing circuit-based models use common analytical formula to calculate leakage inductances which are one of the main difficulties encountered in winding fault transformer circuit-based models [76, 77]. The existing methods [76, 77] have two drawbacks: first, the analytical formulas used to calculate leakage inductances are geometrically constrained and do not account for the core effect, and second, the transformer models employed are not very accurate and detailed. The proposed method not only represents leakage flux paths correctly, but it also considers the effect of the core, including saturation behavior, and can consequently give more accurate leakage inductances. This approach subdivides the faulty winding into some sub sections, resulting in models that resemble multi-winding transformer models. As a result, it can be useful in power electronic studies to simulate multi-winding transformers in dynamic power electronic systems, which as stated in [18, 19, 78, 79], require methods that can accurately calculate leakage inductances between windings as well as be coupled with heavily nonlinear power electronic circuits.

The transformer is modelled in 2D in this work and is validated with 2D FEM, which is still the method of choice in power system applications, especially when connection between the field and circuit equations is sought or when they are employed as validations or improvements of circuit-based methods. In addition, in this studies, magnetic nonlinearity is represented by non-hysteretic models (piecewise linear models), which are sufficiently accurate for transient studies with negligible core losses.

Specifically, it is explained in this chapter how the HBD-circuits proposed in Chapter 2 are improved so that they are capable of modelling transformers. Indeed, it is demonstrated how the HBD-circuits can be extended to include magnetic devices with more than one winding.

The remainder of this chapter is organized as follows. In section 3.1, the principles of the proposed method are outlined for a two-winding single-phase transformer. The proposed method for a two-winding three-phase transformer, which is a practical example, is discussed in greater detail in section 3.2. Section 3.3 explains how the proposed model can be used to model inter-turn faults. Section 3.4 presents and discusses results for three phenomena: normal operation, internal fault, and inrush current. The results are compared with those from a FEM solver.

3.1 Methodology

In this section, the proposed HBD-circuits are explained for a single-phase shell-type transformer which is shown in Figure 3.1. The primary winding is connected to the voltage source U_P through resistance R_P and the secondary winding is connected to the voltage source U_S through resistance R_S. Implementing an electromagnetic model for the defined transformer using circuit-based methods in a meshed form includes three main steps. Firstly, the space of the problem is meshed into suitable number of elements based on the required accuracy. Secondly, Maxwell’s equations including Ampere's and Faraday's laws are employed. Finally, the boundary conditions are imposed.

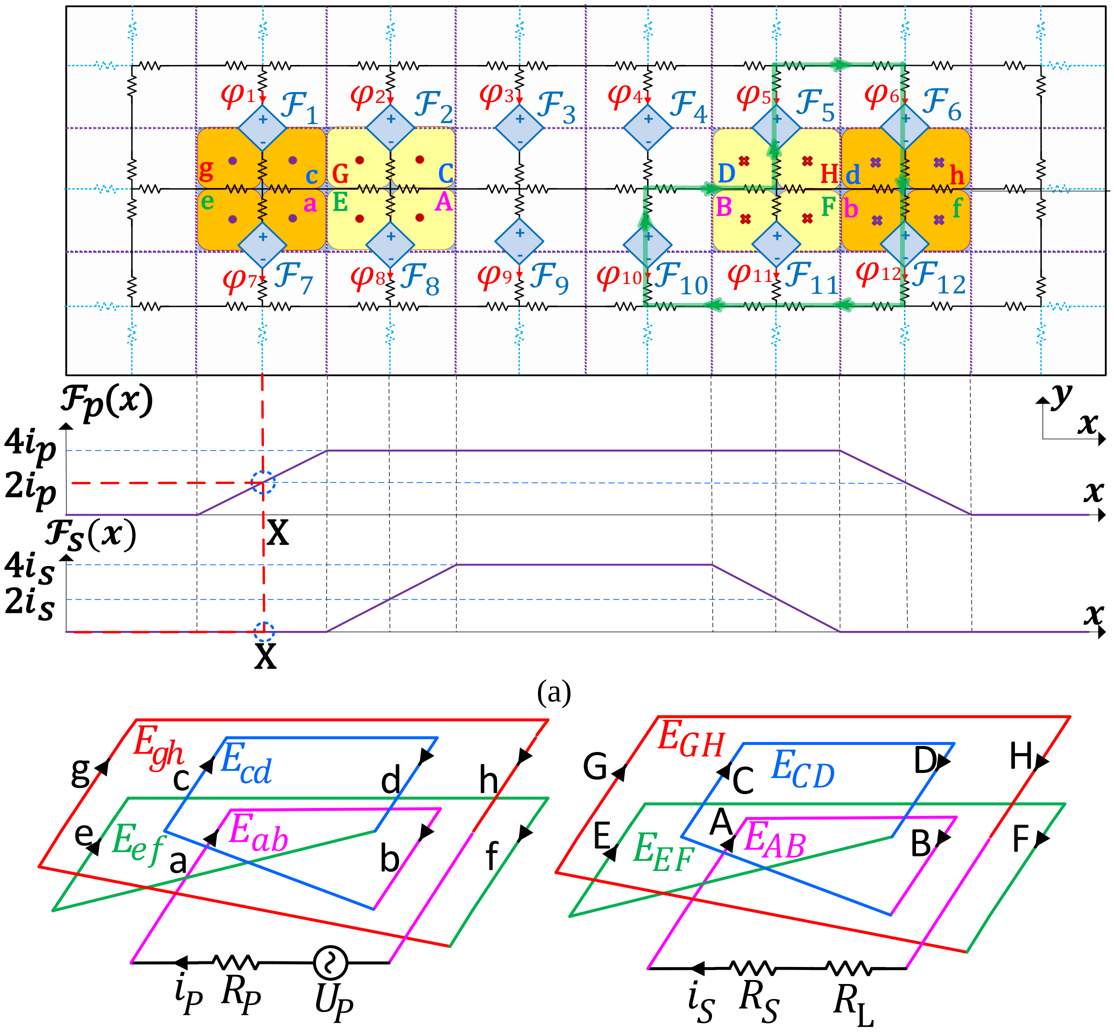

(a)

(b)

Figure 3.1 (a) Distributed magnetic circuit with magnetomotive forces, (b) schematic of transformer winding turns and external circuit

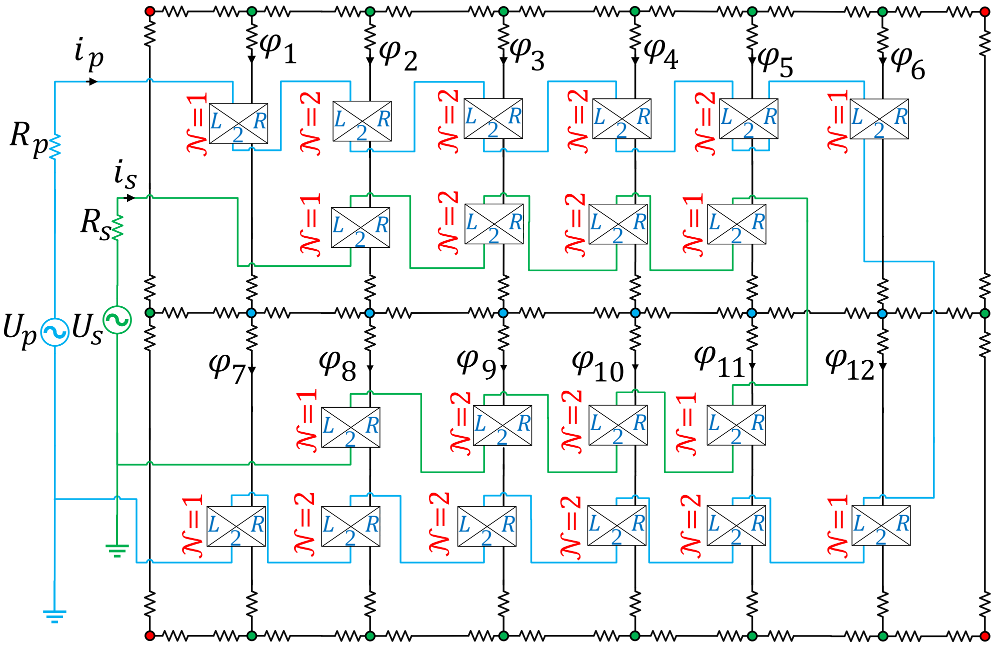

Figure 3.2 DRNM for a transformer (magnetic and electric circuits, as well as their coupling)

3.1.1 Hopkinson Analogy

In this section, as shown in Figure 3.1(a), the problem space is meshed into 24 elements. The magnetic flux paths in each element are represented by two horizontal and two vertical reluctances. To impose the boundary conditions, the reluctances perpendicular to the outside sides of the problem space are also eliminated. In Figure 3.1(a), eliminated reluctances are represented by dashed blue reluctances. In this figure, a, b, c, d, e, f, g, and h determine the primary winding coils, while A, B, C, D, E, F, G, and H determine the secondary winding coils. φ_1, φ_2, φ_3,…, φ_{12} represent the magnetic fluxes that pass through the winding turns, while $(\mathcal{F}_1, \mathcal{F}_2, \mathcal{F}_3, \dots, \mathcal{F}_{12})$ are the magnetomotive force sources distributed through the transformer.

The values of the magnetomotive force sources $(\mathcal{F}_1, \mathcal{F}_2, \mathcal{F}_3, \dots, \mathcal{F}_{12})$ are derived by applying Ampere’s law. Their values in each cell are derived based on this rule: in any closed loop of the problem space, the total magnetomotive force sources around the loop are equal to the sum of all ampere-turn passing through the same loop. For instance, the total magnetomotive force sources around the green loop shown in Figure 3.1(a), which encloses two turns of the primary winding with the current i_p and three turns of the secondary winding with the current i_s, should be equal to

$\mathcal{F} = 2i_p + 3i_s$. According to this rule, the values of the magnetomotive force sources ($\mathcal{F}_1, \mathcal{F}_2, \mathcal{F}_3, \dots, \mathcal{F}_{12}$) are given by

$$\mathbf{F} = \mathbf{N}_{MMF}\mathbf{I} \tag{3.1}$$

where $\mathbf{F} = [\mathcal{F}_1 \quad \mathcal{F}_2 \quad \mathcal{F}_3 \quad \dots \quad \mathcal{F}_{12}]^{\mathrm{T}}$ with $\mathcal{F}_1, \mathcal{F}_2, \mathcal{F}_3, \dots, \mathcal{F}_{12}$ as the values of the magnetomotive force sources indicated in Figure 3.1(a). And $\mathbf{I} = [i_p \quad i_s]^T$ which i_P and i_S are the primary and secondary winding currents, respectively. The components of $\mathbf{N}_{MMF}$ which has been introduced to relate **F** and **I** are derived using curves of the magnetomotive force distribution along the x axis for the primary and secondary windings ($\mathcal{F}_{\mathrm{p}}(x)$ and $\mathcal{F}_{\mathrm{s}}(x)$) presented below the transformer in Figure 3.1(a). On each position in the x axis, the sum of the magnetomotive force sources displayed on the magnetic equivalent circuit must equal the sum of $\mathcal{F}_{\mathrm{p}}(x)$ and $\mathcal{F}_{\mathrm{s}}(x)$ at that point. For example, the sum of $\mathcal{F}_1$ and $\mathcal{F}_7$ in the circuit which are on the same position of $x = X$, equals the sum of $\mathcal{F}_{\mathrm{p}}(x)$ and $\mathcal{F}_{\mathrm{s}}(x)$ at that position, which are $\mathcal{F}_{\mathrm{p}}(\mathrm{X}) = 2ip$ and $\mathcal{F}_{\mathrm{s}}(\mathrm{X}) = 0$, and because the circuit has horizontal symmetry, the values of $\mathcal{F}_1$ and $\mathcal{F}_7$ are the same, and their values equal i_p. The other components of $\mathbf{N}_{MMF}$ are derived using the same rule as follows.

$$\mathbf{N}_{MMF} = \begin{bmatrix} 1 & 2 & 2 & 2 & 2 & 1 & 1 & 2 & 2 & 2 & 2 & 1 \\ 0 & 1 & 2 & 2 & 1 & 0 & 0 & 1 & 2 & 2 & 1 & 0 \end{bmatrix}^T \tag{3.2}$$

Until now, only the magnetic circuit has been included. Faraday's law is used to include the electric circuit and the coupling of the electric and the magnetic circuits. Figure 3.1(b) presents the schematic diagram for winding configuration demonstrating the total magnetic fluxes within each winding turn. The induced voltage in each turn is determined by the fluxes that flow through it. For instance, in the turn AB of the secondary winding which encloses the fluxes of the φ_9 and φ_{10}, the voltage E_{AB} is induced which is derived by

$$E_{AB} = -\frac{d}{dt}(\varphi_9 + \varphi_{10}) \tag{3.3}$$

The voltages induced in other turns and the fluxes passing through them have the same relationship. Then, by adding the voltages induced in the turns of each winding, the total induced voltages in the primary winding E_p and secondary winding E_s are given by

$$\mathbf{E} = -\frac{d}{dt}\mathbf{N}_{EMF}\mathbf{\Phi} \tag{3.4}$$

where

$$\mathbf{E} = \begin{bmatrix} E_p \\ E_s \end{bmatrix} = \begin{bmatrix} E_{ab} + E_{cd} + E_{ef} + E_{gh} \\ E_{AB} + E_{CD} + E_{EF} + E_{GH} \end{bmatrix} \tag{3.5}$$

$$\mathbf{\Phi} = [\varphi_1\ \ \varphi_2\ \ \varphi_3\ \ \varphi_4\ \ \varphi_5\ \ \varphi_6\ \varphi_7\ \varphi_8\ \varphi_9\ \varphi_{10}\ \varphi_{11}\ \varphi_{12}]^T \tag{3.6}$$

$$\mathbf{N}_{EMF} = \mathbf{N}_{MMF}^{\boldsymbol{T}} \tag{3.7}$$

In which E_{AB}, E_{CD}, E_{EF}, E_{GH}, E_{ab}, E_{cd}, E_{ef} and E_{gh} are the electromotive forces induced in the turns AB, CD, EF, GH, ab, cd, ef, and gh respectively. Moreover φ_1, φ_2, φ_3,…, φ_{12} are the magnetic fluxes that pass through the winding turns which have been displayed in Figure 3.1(a). And $\mathbf{N}_{EMF}$ is the matrix introduced to relate **E** and **Φ.**

Finally, the interface between the magnetic and electric circuits is derived using the above-mentioned relations and rules, as shown in Figure 3.2. The magnetic circuit is shown in black, while the primary and secondary winding electric circuits are shown in blue and green, respectively. The sum of electromotive force sources distributed in the primary and secondary winding electric circuits is obviously equal to E_p and E_s, respectively, as shown in Figure 3.2. The primary and secondary side resistances are represented by R_p and R_s. Coupling between the magnetic circuit with both the primary and secondary electric circuits has been achieved using current-controlled voltage sources. In the equivalent circuit of Figure 3.2, each pair of current-controlled voltage sources is a specific type of mutator element, i.e., the Type-2 L-R mutator which was shown in Figure 1.2. As it was stated in the previous chapter, in EMT-type programs, two coupled series R-L branches can be deployed to implement this type of mutator with values determined by (2.5).

3.1.2 Buntenbach Analogy

As it was mentioned in section 2.1.2, the meshes and nodes used to calculate the equivalent circuit for the distributed Buntenbach analogy are the same as those used to derive the equivalent circuit for the Hopkinson analogy, but the resistances in the Hopkinson analogy are substituted with capacitances. Another mutator, the Type-1 L-C mutator [26] (see Figure 1.4), is used to connect the magnetic and electric parts of the circuit. In section 2.1.2, it was also indicated that this type of mutator is implemented using two coupled series R-L branches, the values of which are determined by (2.7). Considering all these rules, the Buntenbach circuit represented in Figure 3.3 is derived. For each mutator in this circuit, the value of coupling factor $\mathcal{N}$ has been determined.

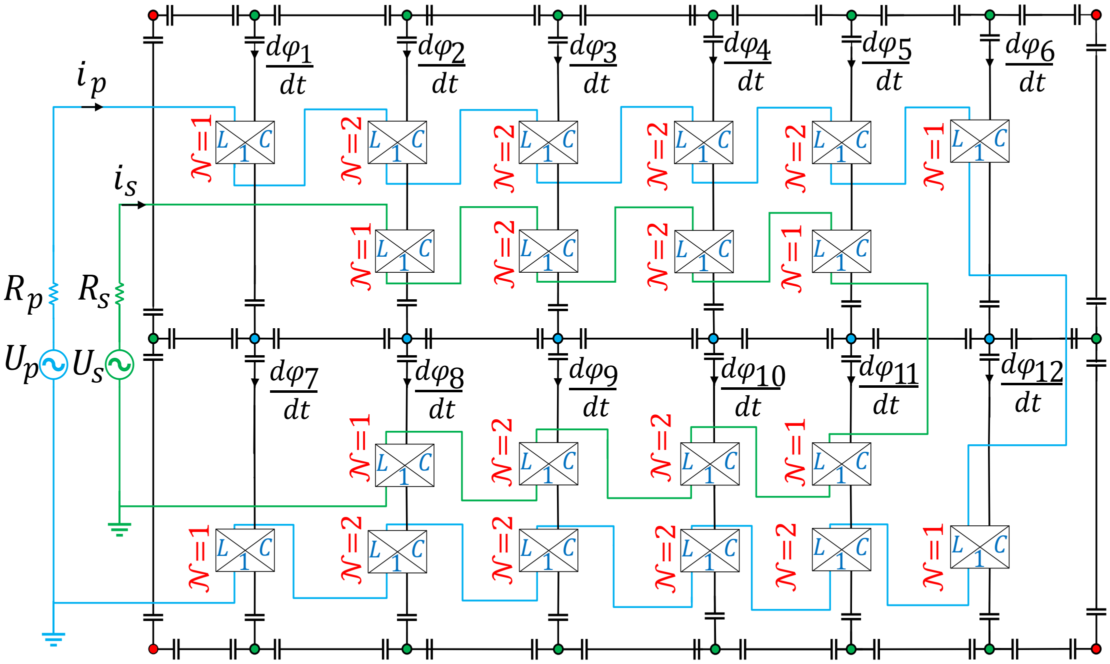

Figure 3.3 Distributed transformer model using Buntenbach analogy, including both magnetic and electric circuits and coupling between them

3.1.3 Duality principle

First, it should be mentioned that the graph of the magnetic circuit in Figure 3.2 is a planar graph, and a dual circuit can be obtained for it. Second, the rules mentioned in section 2.1.3 are employed to derive the electric dual circuit of the magnetic circuit; a) the cells, comprised of resistors that have a common node, are converted to dual cells, comprised of inductances enclosed in a mesh, b) the Type 2 L-R mutator is converted to ideal transformers. As a result, the duality circuit shown in Figure 3.4 is derived for the meshed model of the transformer shown in Figure 3.1.

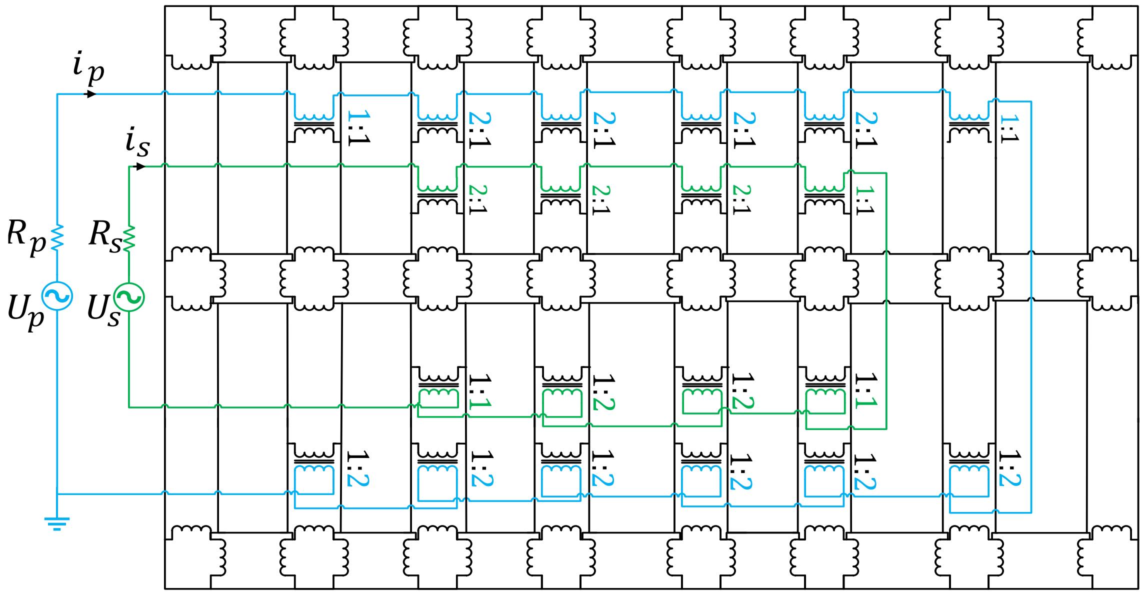

Figure 3.4 Distributed duality-based transformer model, including both magnetic and electric circuits and coupling between them

3.2 Distributed reluctance network model for a three-phase transformer

In this section, HBD-circuits, which were derived for a single-phase transformer in the previous section, are used for a three-phase transformer case. Here, it is implemented only for the three-phase three-legged core-type transformer, but it can be also implemented for the three-phase five-legged core-type and shell-type transformers. In addition, the problem space is meshed into a configurable number of elements, and the formulas required to calculate the properties of each element are presented in detail.

The diagram of the transformer modeled in this section is shown in Figure 3.5. W_p and H_p symbols have been used to determine the width and height of the HV winding, while W_s and H_s symbols have been used to determine the width and height of the LV winding. The thickness of the tank is denoted by the T_n symbol. The length of the air gap between the HV and LV windings for each phase is denoted by btw, and the length of the air gap between the LV winding and the core is denoted by the $lift$ symbol. Also, the air gaps between the HV winding in the central column and the HV windings in the side columns that are equal are represented by the notation BTW. In the three-legged core, all three columns have the same width, shown by the letter C in this diagram.

The letters D and E represent the width and height of the two identical transformer windows. The letter A indicates the mean length of each yoke of the core. Ghp denotes the vertical air gap between the HV winding and the up yoke, while Gbp denotes the vertical air gap between the HV winding and the low yoke. Ghs denotes the vertical air gap between the HV winding and the up yoke, while Gbs denotes the vertical air gap between the HV winding and the low yoke.

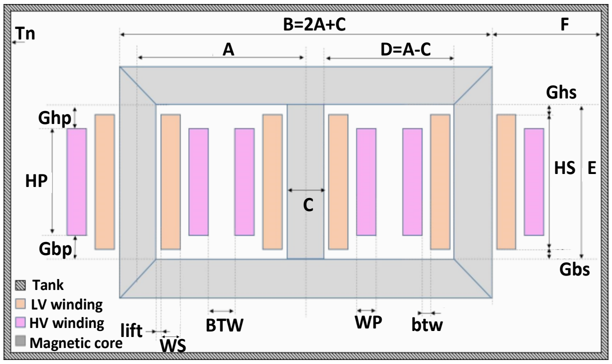

Figure 3.5 Schematic of a three-phase three-legged core-type transformer

The following steps are followed to implement HBD-circuits for the transformer in EMTP. First, the problem space is divided into elements based on the study's requirements and the required accuracy. Second, the model elements are drawn from a set of generic types of elements. Third, the elements are connected based on how the transformer has been meshed as well as the transformer winding connections. Finally, the values for the model elements are determined and given. In the following, these steps are described in more detail.

3.2.1 Meshing and indexing

Since all the three phases of the transformer are similar, the meshing, the indexing, and the value determination processes are the same for all of them. In the following, they are only explained for the phase in the middle column of the core. Furthermore, due to the vertical symmetry of the core, only the meshing for the left side of the core is explained, as illustrated in Figure 3.6. In this diagram, LV winding is represented by the purple colour and HV winding is represented by the yellow colour. In addition, the core is depicted in grey, the tank is represented by diagonal black lines, and the air parts are shown in white. W_p and H_p symbols have been used to determine the width and height of the HV winding, while W_s and H_s symbols have been used to determine the width and height of the LV winding. The thickness of the tank is denoted by the T_n symbol. In the mesh applied to this diagram, the number of elements along the x axis is M and along the y axis is N. Based on the type and position of the elements used to model the transformer, the transformer has been subdivided into ten distinct areas labelled 1, 2, 3, 4, 5, 6, 7, 33, 44, and 66, with these numbers shown in the left-up position of each area.

In addition, the HBD-circuits for this transformer are made up of four general types of cells: Type-A, Type-B, Type-C, and Type-D which have been indicated in Figure 3.7 for Hopkinson Analogy, in Figure 3.8 for Buntenbach Analogy, and in Figure 3.9 for duality principle. Each of the four types of Hopkinson elements contains four linear or nonlinear resistive elements called R_u, R_d, R_r and R_l which have been shown in Figure 3.7. And as shown in Figure 3.8, each of the four types of Buntenbach elements has four linear or nonlinear capacitive elements: C_u, C_d, C_r, and C_l. Four linear or nonlinear inductive components found in each of the four types of duality elements, as depicted in Figure 3.9. These are L_u, L_d, L_r, and L_l. In Type-B cells, there is one pair of mutators which are for HV winding. In Type-C cells, there are two pairs of mutators, one pair for HV winding and the other for LV winding. In Type-D cells, there is a single pair of LV winding mutators. In Figure 3.7, Figure 3.8, and Figure 3.9, the coupling factors of the mutators associated to HV and LV windings are defined by β_{ij} and γ_{ij}, respectively. Parts 1 and 7 are made up of Type-A elements, parts 2 and 5 are made up of Type-B elements, parts 3, 4, and 6 are made up of Type-C elements, and parts 33, 44, and 66 are made up of Type-D components for the parts shown in Figure 3.6.

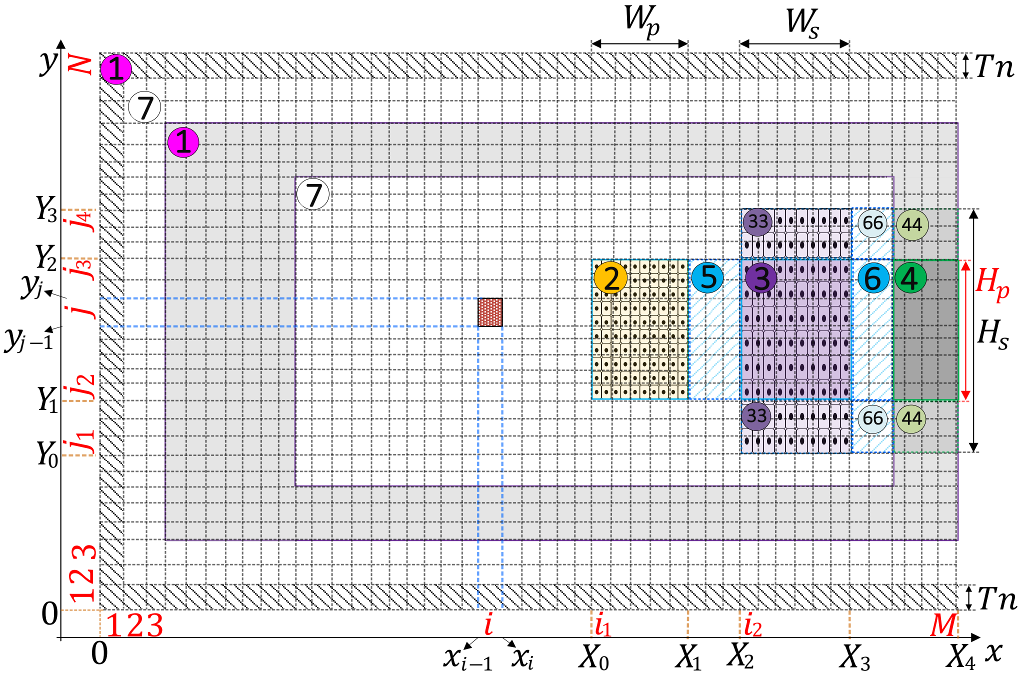

Figure 3.6 Cross-section of left half of the core

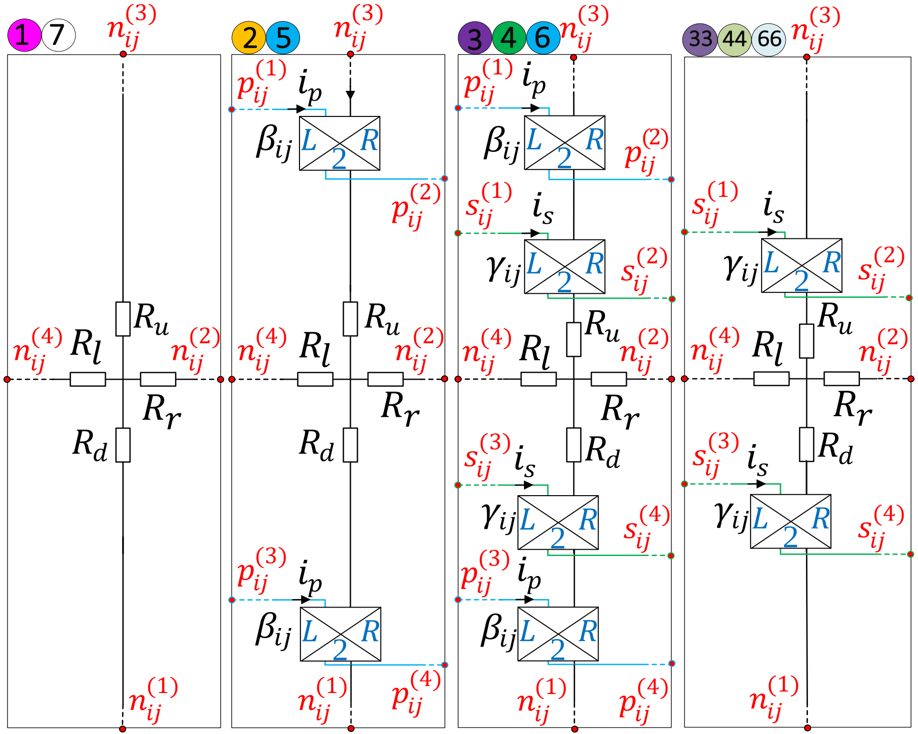

(Type-A) (Type-B) (Type-C) (Type-D)

Figure 3.7 Circuits based on Hopkinson Analogy for four cell types (A, B, C, and D)

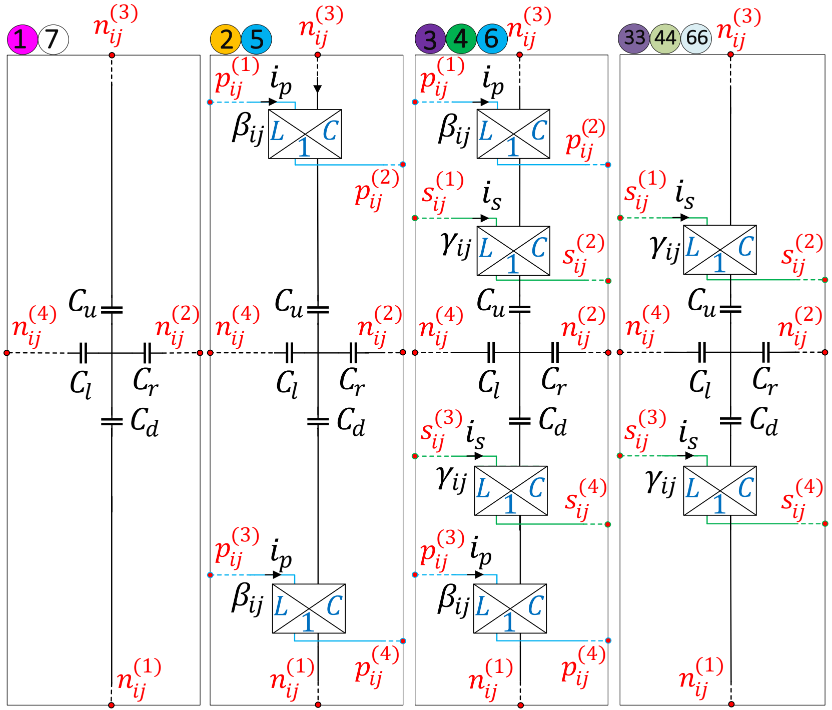

(Type-A) (Type-B) (Type-C) (Type-D)

Figure 3.8 Circuits based on Hopkinson Analogy for four cell types (A, B, C, and D)

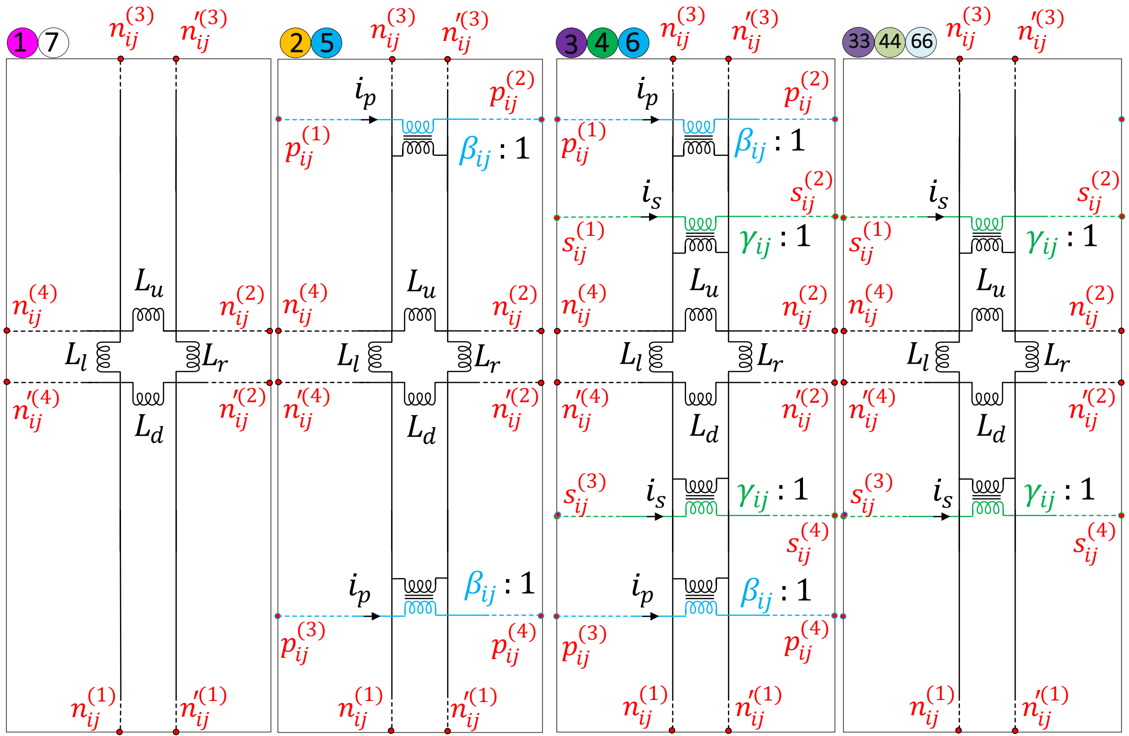

(Type-A) (Type-B) (Type-C) (Type-D)

Figure 3.9 Circuits based on Duality principle for four cell types (A, B, C, and D)

3.2.2 Determination of circuit parameters

The RLC parameters for elements are calculated in the same way that they were calculated in sections 2.1.1, 2.1.2, and 2.1.3, but the parameters of the mutators of the Type-B, Type-C, and Type-D elements depicted in Figure 3.7, Figure 3.8, and Figure 3.9 are found by applying Ampere's law and Faraday's law in a distributed form. The coupling factors β_{ij} and γ_{ij}, which are related to the mutators of the HV and LV windings of the element in i^{th} column and j^{th} row of the mesh presented in Figure 3.6, are given by (3.8) and (3.9) respectively. Where N_p and N_s represent the number of HV and LV winding turns, respectively. W_p and W_s are the widths of the HV and LV windings, respectively, and H_p and H_s are the heights of the HV and LV windings. x_{i-1}, x_i, y_{j-1} and y_j are the horizontal and vertical coordinates of the cell placed in i^{th} column and j^{th} row. X_0, X_1, Y_1 and Y_2 are the horizontal and vertical coordinates of the HV winding and X_2, X_3, Y_0 and Y_3 are the horizontal and vertical coordinates of the LV winding. X_4 is the horizontal coordinate of the center of the core.

$$\beta_{ij} = \begin{cases} \dfrac{N_p(y_j - y_{j-1})}{2W_pH_p}\left(\dfrac{x_{i-1} + x_i}{2} - X_0\right) & x_{i-1} \geq X_0, x_i \leq X_1, y_{j-1} \geq Y_1, y_j \leq Y_2 \\ \dfrac{N_p(y_j - y_{j-1})}{2H_p} & x_{i-1} \geq X_1,\ x_i \leq X_4,\ y_{j-1} \geq Y_1,\ y_j \leq Y_2 \end{cases} \tag{3.8}$$

$$\gamma_{ij} = \begin{cases} \dfrac{N_s(y_j - y_{j-1})}{2W_sH_s}\left(\dfrac{x_{i-1} + x_i}{2} - X_2\right) & x_{i-1} \geq X_2,\ x_i \leq X_3,\ y_{j-1} \geq Y_0,\ y_j \leq Y_3 \\ \dfrac{N_s(y_j - y_{j-1})}{2H_s} & x_{i-1} \geq X_3,\ x_i \leq X_4,\ y_{j-1} \geq Y_0,\ y_j \leq Y_3 \end{cases} \tag{3.9}$$

3.2.3 Connection of model elements

After finding and assigning the parameters for each element, the elements must now be connected internally before being linked to the external circuit. As it can be observed in the Hopkinson and Buntenbach elements presented in Figure 3.7 and Figure 3.8, nodes $n_{ij}^{(1)}$, $n_{ij}^{(2)}$, $n_{ij}^{(3)}$, and $n_{ij}^{(4)}$ are the nodes related to the magnetic part of the element placed in i^{th} column and j^{th} row of mesh shown in Figure 3.6. In Algorithm 3.1, it has been shown how magnetic parts of the elements are connected through these nodes for Hopkinson and Buntenbach Circuits. For duality elements shown in Figure 3.9, in which $n_{ij}^{(1)}$, $n_{ij}^{(2)}$, $n_{ij}^{(3)}$, $n_{ij}^{(4)}$, ${n'}_{ij}^{(1)}$, ${n'}_{ij}^{(2)}$, ${n'}_{ij}^{(3)}$, and ${n'}_{ij}^{(4)}$ are the nodes related to the magnetic part, Algorithm 3.2 is followed to connect magnetic parts of the elements.

For all three HBD-circuits, Algorithm 3.3 and Algorithm 3.4 are used to establish the internal electrical connections between elements. As it can be observed in the elements presented in Figures Figure 3.7, Figure 3.8 and Figure 3.9, nodes $p_{ij}^{(1)}$, $p_{ij}^{(2)}$, $p_{ij}^{(3)}$, and $p_{ij}^{(4)}$ are the nodes related to the HV winding of the element placed in i^{th} column and j^{th} row of Figure 3.6 and they are connected using the procedure presented in Algorithm 3.3. Nodes $s_{ij}^{(1)}$, $s_{ij}^{(2)}$, $s_{ij}^{(3)}$, and $s_{ij}^{(4)}$ are the nodes related to the LV winding of those elements and they are connected using the procedure presented in Algorithm 3.3. In all three HBD-circuits, the internal electrical connections for two other transformer phases are established using the same algorithms.

Algorithm 3.1 Internal magnetic connections for Hopkinson and Buntenbach circuits

```
for $j^{*} \leftarrow 1$ to $N^{**}$ do
    for $i^{***} \leftarrow 1$ to $(2M^{****})$ do
        if $j < N$ & $i < 2M$
            connect $(n_{ij}^{(2)}, n_{(i+1)j}^{(4)})$
            connect $(n_{ij}^{(3)}, n_{i(j+1)}^{(1)})$
        elseif $j = N$ & $i < 2M$
            connect $(n_{ij}^{(2)}, n_{(i+1)j}^{(4)})$
        elseif $j < N$ & $i = 2M$
            connect $(n_{ij}^{(3)}, n_{i(j+1)}^{(1)})$
        end
    end
end
```

*: j is the row number of the cell.

**: N is the total number of rows in Figure 3.6.

***: i is the column number of the cell.

****: M is total number of columns in Figure 3.6.

Algorithm 3.2. Internal magnetic connections for Duality circuit

```
for $j^{*} \leftarrow 1$ to $N^{**}$ do
    for $i^{***} \leftarrow 1$ to $(2M^{****})$ do
        if $j < N$ & $i < 2M$
            connect $(n_{ij}^{(2)}, n_{(i+1)j}^{(4)})$
            connect $(n'^{(2)}_{ij}, n'^{(4)}_{(i+1)j})$
            connect $(n_{ij}^{(3)}, n_{i(j+1)}^{(1)})$
            connect $(n'^{(3)}_{ij}, n'^{(1)}_{i(j+1)})$
        elseif $j = N$ & $i < 2M$
            connect $(n_{ij}^{(2)}, n_{(i+1)j}^{(4)})$
            connect $(n'^{(2)}_{ij}, n'^{(4)}_{(i+1)j})$
        elseif $j < N$ & $i = 2M$
            connect $(n_{ij}^{(3)}, n_{i(j+1)}^{(1)})$
            connect $(n'^{(3)}_{ij}, n'^{(1)}_{i(j+1)})$
        end
    end
end
```

*: j is the row number of the cell.

**: N is the total number of rows in Figure 3.6.

***: i is the column number of the cell.

****: M is total number of columns in Figure 3.6.

Algorithm 3.3. Electric connections for HV windings in all HBD-circuits

```
for $j \leftarrow j_2^{*}$ to $j_3^{**}$ do
    for $i \leftarrow i_1^{***}$ to $(2M - i_1)$ do
        connect $(p_{ij}^{(2)}, p_{(i+1)j}^{(1)})$
        connect $(p_{ij}^{(4)}, p_{(i+1)j}^{(3)})$
    end
    connect $(p_{(2M-i_1+1)^{****}j}^{(2)}, p_{(i_1)j}^{(3)})$
    if $j > j_2$ then
        connect $(p_{(2M-i_1+1)j}^{(4)}, p_{(i_1)(j-1)}^{(3)})$
    end
end
```

*: j_2 is the row number of the lowest cells related to HV winding in Figure 3.6.
**: j_3 is the row number of the highest cells related to HV winding in Figure 3.6.
***: i_1 is the column number of the leftmost cells related to HV winding in Figure 3.6.
****:$2M - i_1 + 1$ is the column number of the rightmost cells related to right part of HV winding which due to the symmetry has not been shown in Figure 3.6.

Algorithm 3.4. Electric connections for LV winding in all HBD-circuits

```
for $j \leftarrow j_1^{*}$ to $j_4^{**}$ do
for $i \leftarrow i_2^{***}$ to $(2M - i_2)$ do
        connect $(s_{ij}^{(2)}, s_{(i+1)j}^{(1)})$
        connect $(s_{ij}^{(4)}, s_{(i+1)j}^{(3)})$
end
connect $(s_{(2M-i_2+1)^{****}j}^{(2)}, s_{(i_2)j}^{(3)})$
if $j > j_1$ then
    connect $(s_{(2M-i_2+1)j}^{(4)}, s_{(i_2)(j-1)}^{(3)})$
end
```

*: j_1 is the row number of the lowest cells related to LV winding in Figure 3.6.
**: j_4 is the row number of the highest cells related to LV winding in Figure 3.6.
***: i_2 is the column number of the leftmost cells related to LV winding in Figure 3.6.
****:$2M - i_2 + 1$ is the column number of the rightmost cells related to right part of LV winding which due to the symmetry has not been shown in Figure 3.6.

3.3 Study of internal faults using HBD-circuits

In this section, the proposed HBD-circuits are used to model internal faults in transformer using EMTP. To accomplish this, the faulty and healthy parts of the winding are treated as distinct windings. The fault between a coil and the ground, as well as the fault between two turns of a winding, are both modelled using HBD-circuits. To model a turn-to-earth fault, the faulty winding is divided into two parts, as shown in Figure 3.10(a). As illustrated in Figure 3.10(b), the faulty winding is divided into three parts to model a turn-to-turn fault. In HBD-circuits, each new part is treated as a distinct winding, with Ampere's and Faraday's laws applied independently. The distinct parts are then connected to one another, with the faulty part is also being connected to the impedance of the fault. The steps in the prior section are followed to model internal faults. However, because additional parts have been introduced, new elements must be defined.

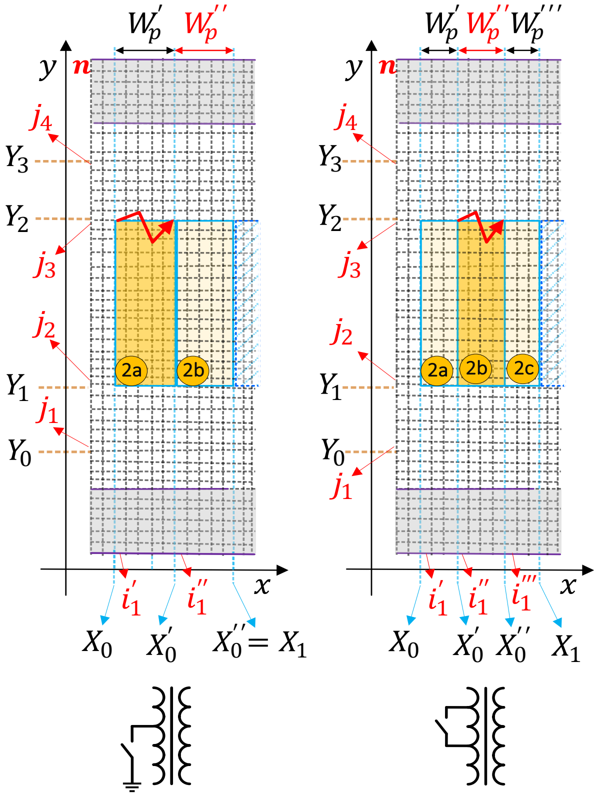

(a) (b)

Figure 3.10 Meshes generated for a portion of a faulty transformer with a fault in the middle column's HV winding, (a) Turn to earth fault, (b) Turn to turn fault

3.3.1 Element definition

A pair of mutators are added to the model exclusively for each part of the faulty winding that was deemed as a separate winding. Figure 3.11 shows three new defined element types (Type-B$_1$, Type-B$_2$, and Type-C$_1$) for a case involving a coil-to-earth fault using Hopkinson method. For this type of fault, based on Buntenbach Analogy, Figure 3.12 displays three new element types (Type-B$_1$, Type-B_2, and Type-C_1). To represent this type of fault using duality principle, three new element types (Type-B_1, Type-B_2, and Type-C_1) shown in are used Figure 3.13. The healthy section of the winding, which is labelled 2a in Figure 3.10(a), is represented by a pair of mutators with the coupling factor of β'_{ij} in the Type-B_1, Type-B_2, and Type-C_1 cells. And for the faulty section of the winding, which is labelled 2b in Figure 3.10(a), a pair of mutators with the coupling factor of β''_{ij} has been provided in Type-B_2 and Type-C_1 cells.

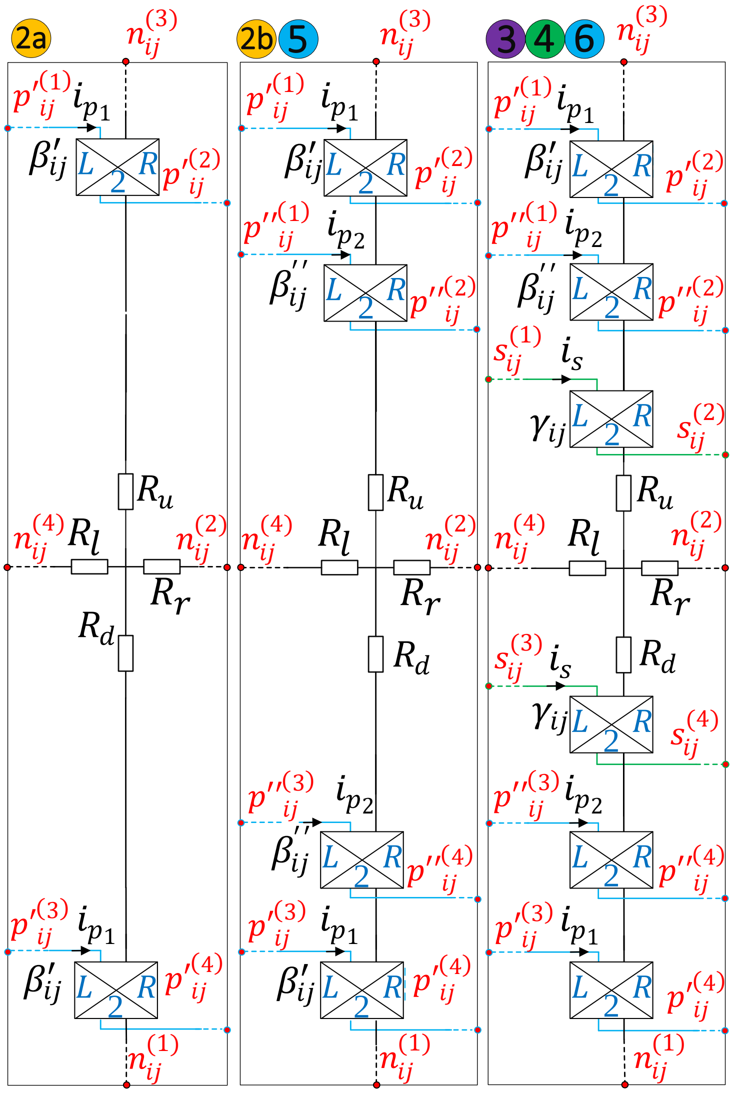

(Type-B_1) (Type-B_2) (Type-C_1)

Figure 3.11 Circuits based on Hopkinson Analogy for three cell types (B_1, B_2 C_1) related to the mesh generated in Figure 3.10(a)

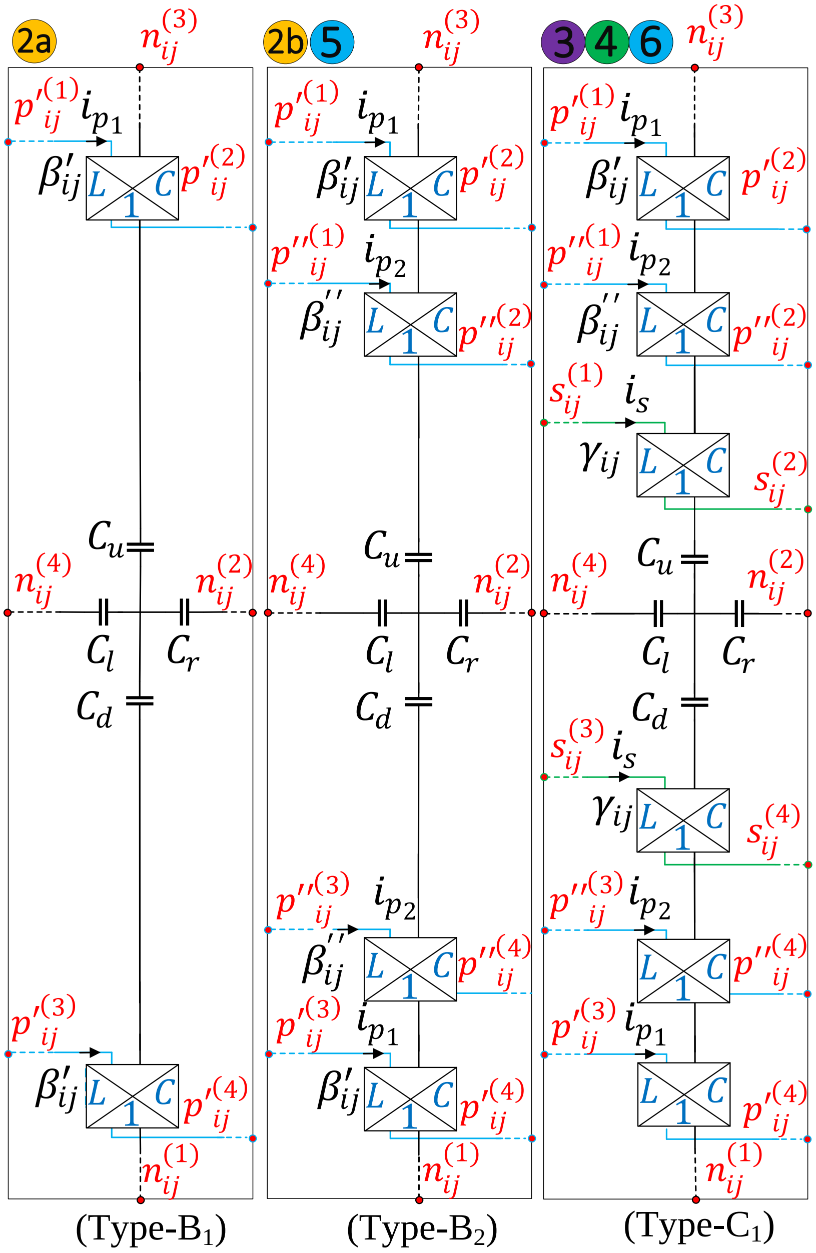

Figure 3.12 Circuits based on Buntenbach Analogy for three cell types (B1, B2, and C1) related to the mesh generated in Figure 3.10(a)

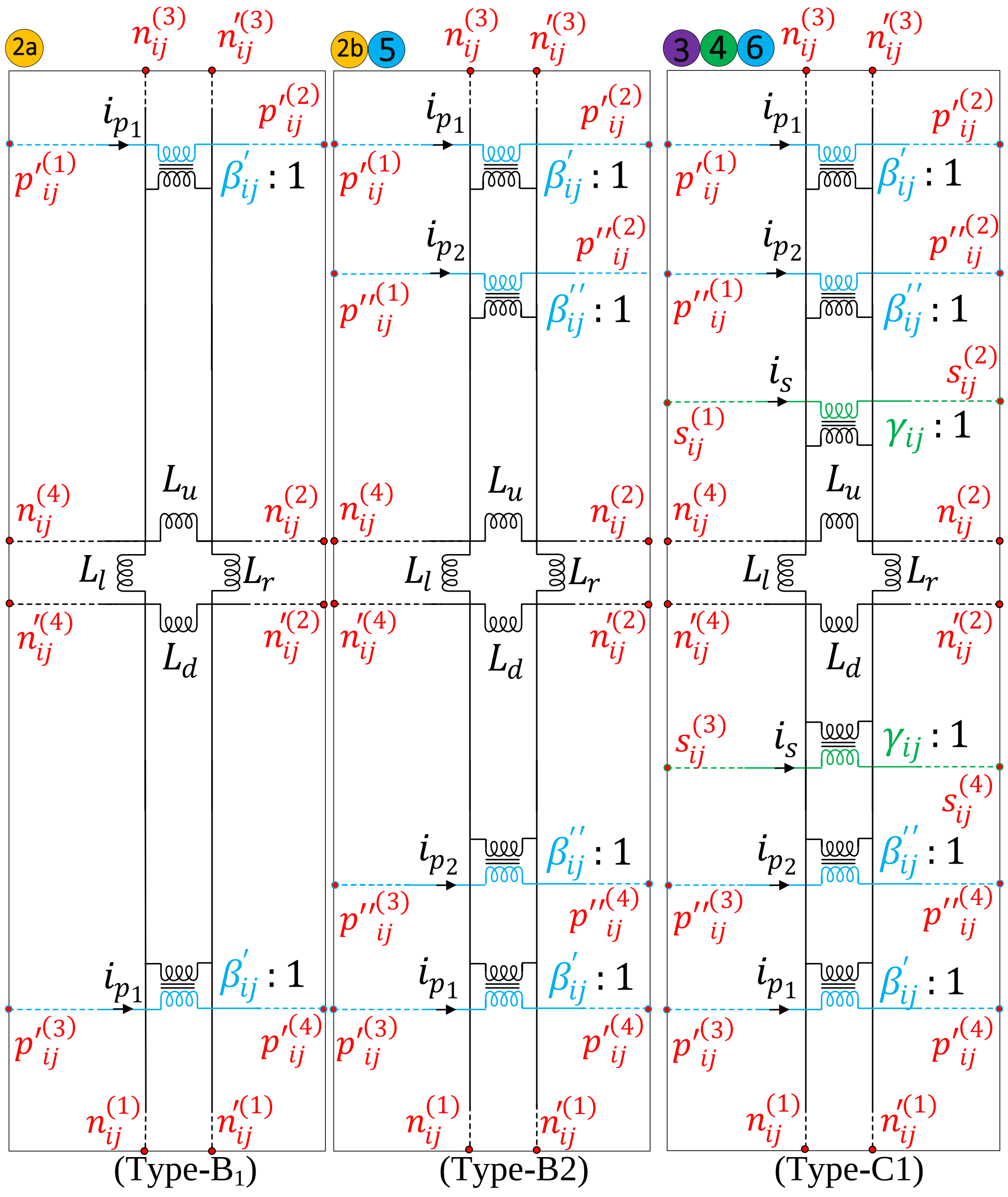

Figure 3.13 Circuits based on Duality principle for three cell types (B$_1$, B$_2$ C$_1$) related to the mesh generated in Figure 3.10(a)

For the turn-to-turn fault case, which has been shown in Figure 3.10(b), four new element types (Type-B$_1$, Type-B$_2$, Type-B$_3$, and Type-C$_2$) are defined. Figure 3.14, Figure 3.15, and Figure 3.16 show equivalent circuits for Hopkinson Analogy, Buntenbach Analogy, and the duality principle, respectively. The healthy section of the winding, which is labelled 2a in Figure 3.10(b) and is in the left side of the faulty section, is represented by a pair of mutators with the coupling factor of $\beta_{ij}^{\prime}$ in the Type-B$_1$, Type-B$_2$, Type-B$_3$, and Type-C$_2$ cells. A pair of mutators with the coupling factor of $\beta_{ij}^{\prime\prime}$ has been used in Type-B$_2$, Type-B$_3$, and Type-C$_2$ cells for the faulty section of the winding, which is labelled 2b in Figure 3.10(b). The other healthy section of the winding, which is labelled 2c in Figure 3.10(b) and is on the right side of the faulty section, is indicated by a pair of mutators with the coupling factor of β_{ij}''' in the Type-B$_3$ and Type-C$_2$ cells.

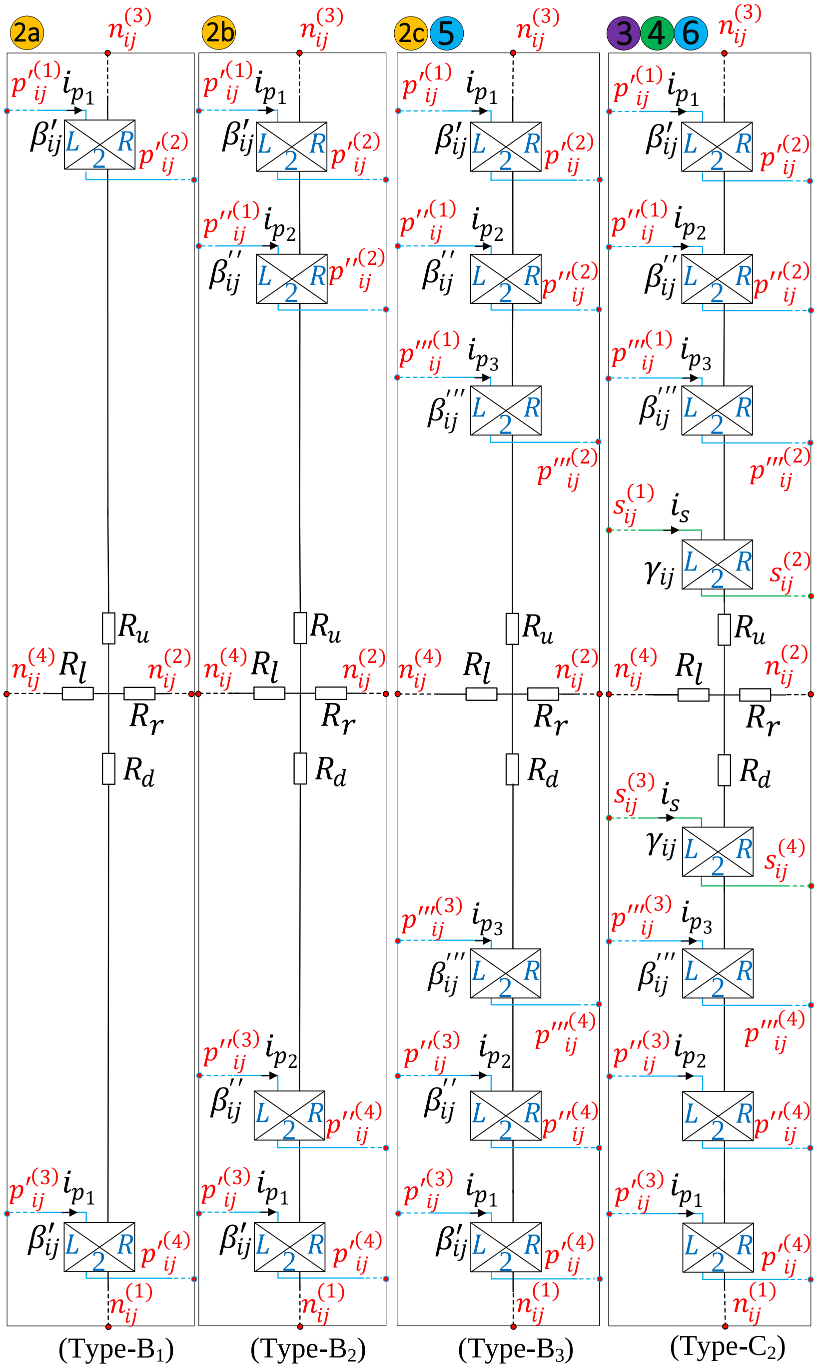

Figure 3.14 Circuits based on Hopkinson Analogy for four cell types (B$_1$, B$_2$ B$_3$, C$_2$) related to the mesh generated in Figure 3.10(b)

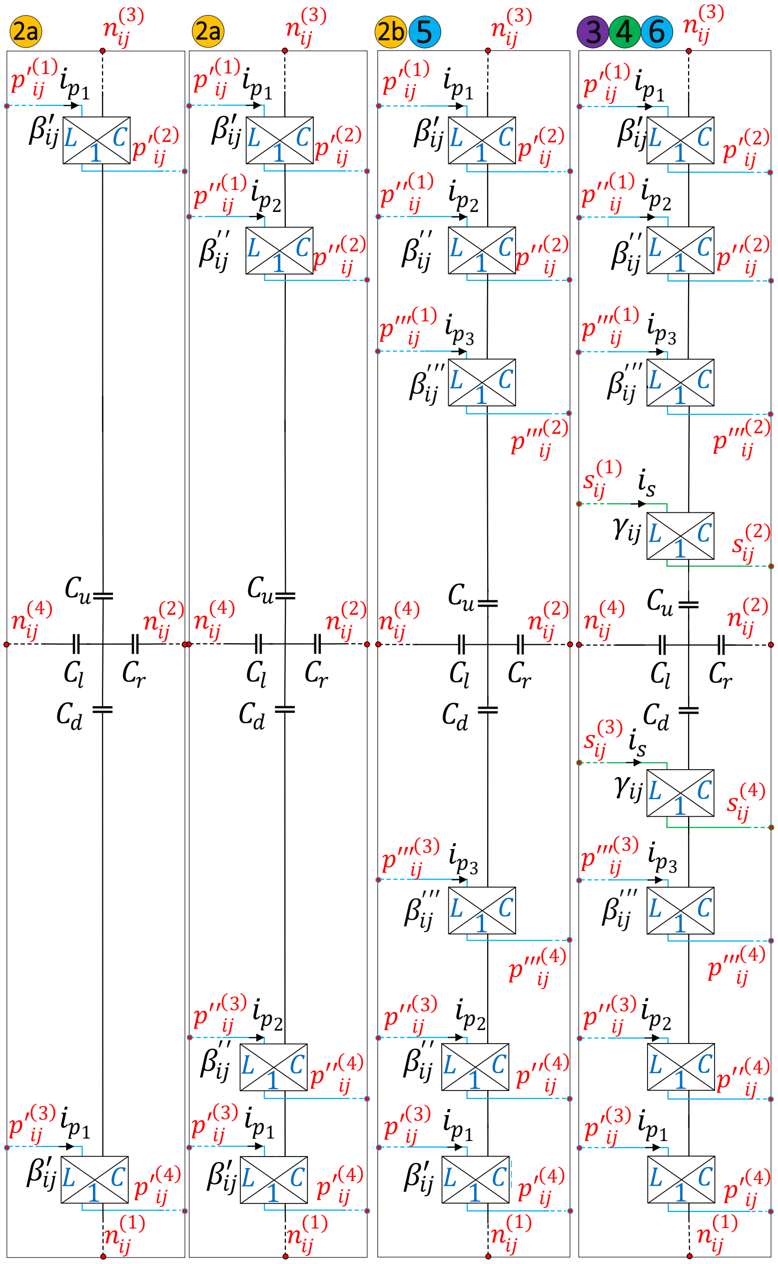

(Type-B1) (Type-B2) (Type-B3) (Type-C2)

Figure 3.15 Circuits based on Buntenbach Analogy for four cell types (B₁, B₂ B₃, C₂) related to the mesh generated in Figure 3.10(b)

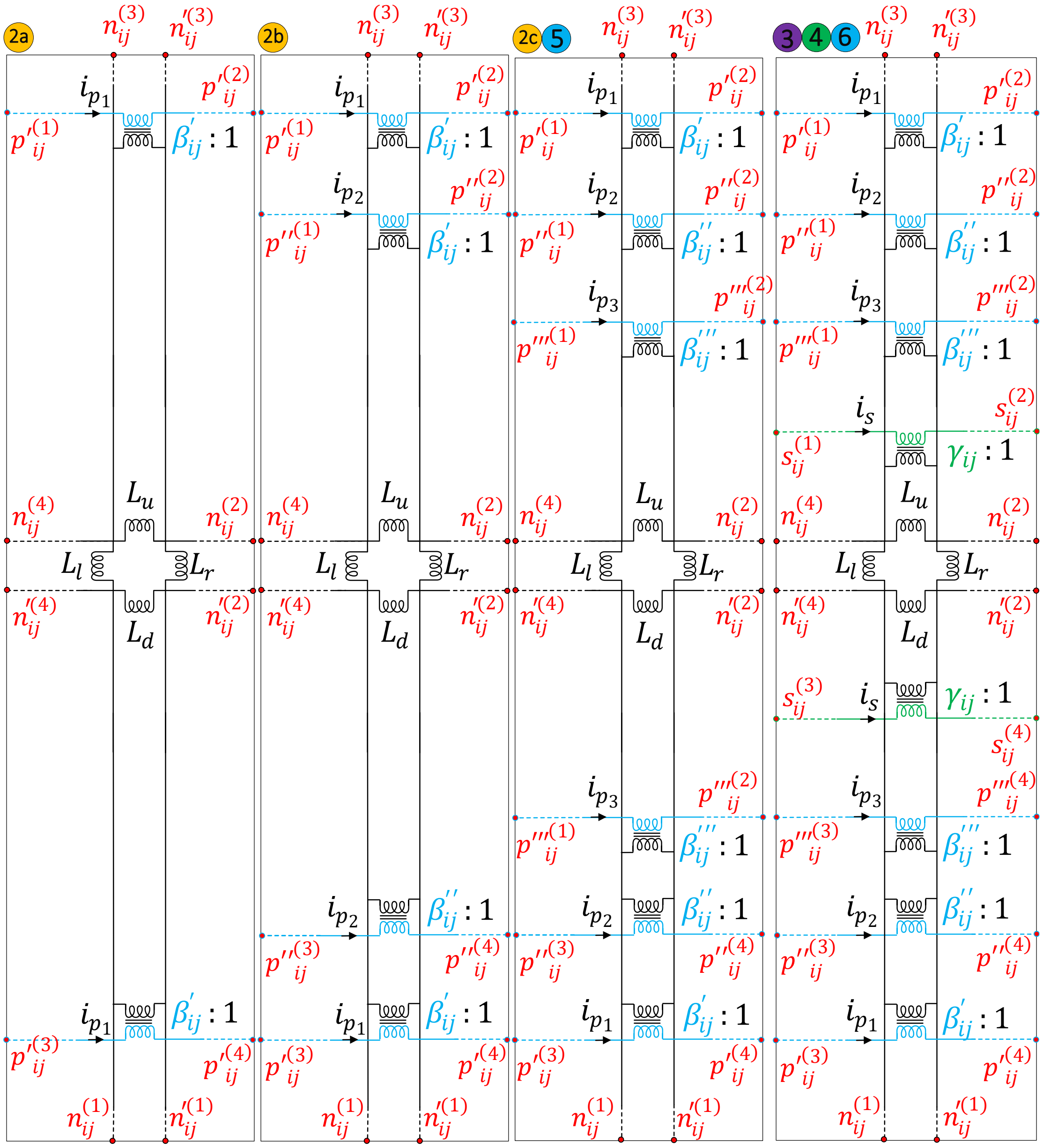

(Type-B$_1$) (Type-B$_2$) (Type-B$_3$) (Type-C$_2$)

Figure 3.16 Circuits based on Duality principle for four cell types (B$_1$, B$_2$ B$_3$, C$_2$) related to the mesh generated in Figure 3.10(b)

3.3.2 Determination of circuit parameters

The RLC parameters for elements are determined in the same manner as in 2.1.1, 2.1.2, and 2.1.3. And the coupling factor γ_{ij}, which is related to the mutator of the LV winding of the element in i^{th} column and j^{th} row of the meshes presented in Figure 3.10(a) and (b), is given by (3.9). The coupling factor of the new mutators shown in Figure 3.11- Figure 3.16 are given by (3.10), (3.11), and (3.12) where N_p is the number of turns of HV winding, and for the turn to earth fault shown in Figure 3.10(a), W_p' and W_p'' are the width of the faulty and healthy parts of HV winding, X_0, X_0', Y_1 and Y_2 are the horizontal and vertical coordinates of the faulty part of HV winding and X_0', X_0'', Y_1 and Y_2 are the horizontal and vertical coordinates of the healthy part of HV winding. And for the turn-to-turn fault shown in Figure 3.10(b), W_p' and W_p''' are the widths of the healthy parts of HV winding, and W_p'' is the width of the faulty part. X_0, X_0', Y_1 and Y_2 are the horizontal and vertical coordinates of the healthy part of HV winding which is on the left side of the faulty part and X_0', X_0'', Y_1 and Y_2 are the horizontal and vertical coordinates of the faulty part of HV winding and X_0'', X_0''', Y_1 and Y_2 are the horizontal and vertical coordinates of the healthy part of HV winding which is located on the right side of the faulty part.

$$\beta_{ij}' = \begin{cases} \dfrac{N_p\left(y_j - y_{j-1}\right)}{2W_pH_p}\left(\dfrac{x_{i-1}+x_i}{2} - X_0\right) & x_{i-1} \geq X_0,\ x_i \leq X_0',\ y_{j-1} \geq Y_1,\ y_j \leq Y_2 \\ \dfrac{N_pW_p'(y_i - y_{i-1})}{2W_p^2H_p} & x_{i-1} \geq X_0',\ x_i \leq X_4,\ y_{j-1} \geq Y_1,\ y_j \leq Y_2 \end{cases} \tag{3.10}$$

$$\beta_{ij}'' = \begin{cases} \dfrac{N_p\left(y_j - y_{j-1}\right)}{2W_pH_p}\left(\dfrac{x_{i-1}+x_i}{2} - X_0'\right) & x_{i-1} \geq X_0',\ x_i \leq X_0'',\ y_{j-1} \geq Y_1,\ y_j \leq Y_2 \\ \dfrac{N_pW_p''(y_i - y_{i-1})}{2W_pH_p} & x_{i-1} \geq X_0'',\ x_i \leq X_4,\ y_{j-1} \geq Y_1,\ y_j \leq Y_2 \end{cases} \tag{3.11}$$

$$\beta_{ij}''' = \begin{cases} \dfrac{N_p\left(y_j - y_{j-1}\right)}{2W_pH_p}\left(\dfrac{x_{i-1}+x_i}{2} - X_0''\right) & x_{i-1} \geq X_0'', x_i \leq X_1, y_{j-1} \geq Y_0, y_j \leq Y_3 \\ \dfrac{N_pW_p'''(y_i - y_{i-1})}{2W_pH_p} & x_{i-1} \geq X_1, x_i \leq X_4, y_{j-1} \geq Y_0, y_j \leq Y_3 \end{cases} \tag{3.12}$$

3.3.3 Connection of model elements

The rules for all magnetic and electric connections of the model are identical to the rules outlined in section 3.2.3. Except that the faulty winding is divided into distinct windings, and the connections between the mutators for each distinct winding are made by the procedure presented in Algorithm 3.5.

Algorithm 3.5 Electric connections for HV winding

```
for $j \leftarrow j_2$ to $j_3$ do
    for $w \leftarrow (i_1'^{*}, i_1''^{**}, i_1'''^{***})$
        for $i \leftarrow w$ to $(2M - w)$ do
            connect $(p_{ij}^{(2)}, p_{(i+1)j}^{(1)})$
            connect $(p_{ij}^{(4)}, p_{(i+1)j}^{(3)})$
        end
        connect $(p_{(2M-w+1)^{****}j}^{(2)}, p_{(w)j}^{(3)})$
        if $j > j_2$ then
            connect $(p_{(2M-w+1)\,j}^{(4)}, p_{(w)(j-1)}^{(3)})$
        end
    end
end
```

*: i_1' : for turn-to-earth fault in Figure 3.10(a) is the column number of the leftmost cells related to the faulty part of HV winding called part 2a, and for turn-to-turn fault shown in Figure 3.10(b) is the column number of the leftmost cells related to the healthy part of HV winding called part 2a.

**: i_1'' : for turn to earth fault in Figure 3.10(a) is the column number of the leftmost cells related to the healthy part of HV winding and for turn to turn fault in Figure 3.10(b) is the column number of the leftmost cells related to the faulty part of HV winding called part 2b.

***: i_1''' : for turn-to-turn fault in Figure 3.10(b) is the column number of the leftmost cells related to the healthy part of HV winding called part 2c.

****:$2M - w + 1$ is the column number of the rightmost cells related to right part of different sections of HV windings which due to the symmetry has not been shown in Figure 3.10.

3.4 Results and validation

In this section, the proposed HBD-circuits approaches are implemented for the three-phase transformer shown in Figure 3.5, whose characteristics are listed in Table 3.1 and dimensions are listed in Table 3.2. The DRNM approach is implemented using EMTP [34], and FEM is solved using ANSYS Electromagnetics.

Initially, we must determine the suitable mesh size before we can obtain the results. In a similar way to FEM, the accuracy that can be obtained from HBD-circuits is directly related to the mesh that is used. As the elements are reduced in size and the mesh is refined, the computed solution will approach the true solution. However, as the number of elements increases, the computational burden increase, and as a result, a technique known as mesh refinement is used. Mesh refinement is a process in which the mesh size is successively reduced, and the results are compared. Two mesh refinement metrics are investigated to determine whether the mesh refinement has resulted in a converged solution. One local metric and one global metric are used in this chapter. The local metric is the magnetic flux amplitude in a single spot on the core, while the global metric is the current of the HV winding. Figure 3.17 illustrates the convergence of both the global (red) and local (blue) metrics with 1% error bars in comparison to the most refined solution. After weighing all of these factors, the mesh size for HBD-circuits is set to 2848. In addition, the FEM mesh includes 3292 elements.

Table 3.1 Specifications of transformer

Nominal power (MVA)	15	Connection type	YnD
Primary voltage (kV)	25.663	Number of primary winding turns	317
Secondary voltage (kV)	4.530	Number of secondary winding turns	56

Table 3.2 Design and geometrical parameters of transformer

Parameter	Length [mm]	Parameter	Length [mm]	Parameter	Length [mm]
A	995	HS	1190	HP	1121
B	2410	Ghs	158	Ghp	197
C	420	Gbs	143	Gbp	182
D	575	lift	21	WP	60
E	1491	WS	45.5	btw	91

After meshing and to have the results to validate the models, first, open-circuit results are acquired by unloading the secondary, exciting the primary winding at various voltage levels, and deriving the current in the primary winding (to see the circuit used in this case, see Figure 3.18). In Figure 3.19, rms voltage-current characteristics derived from HBD-circuits are compared to those obtained from FEM in 2D. To provide validation for the accuracy of HBD-circuits in representing transformer behavior in open-circuit condition, the normalized root mean square error (nRMSE) is applied on the voltage-current characteristic derived by each method. The nRMSE results for both linear and saturated operating conditions are presented in Table 3.3. It can be concluded that HBD-circuits give accurate results in comparison with FEM and they are around 1-2% range in linear operating conditions, and 3-4% in saturated operating conditions.

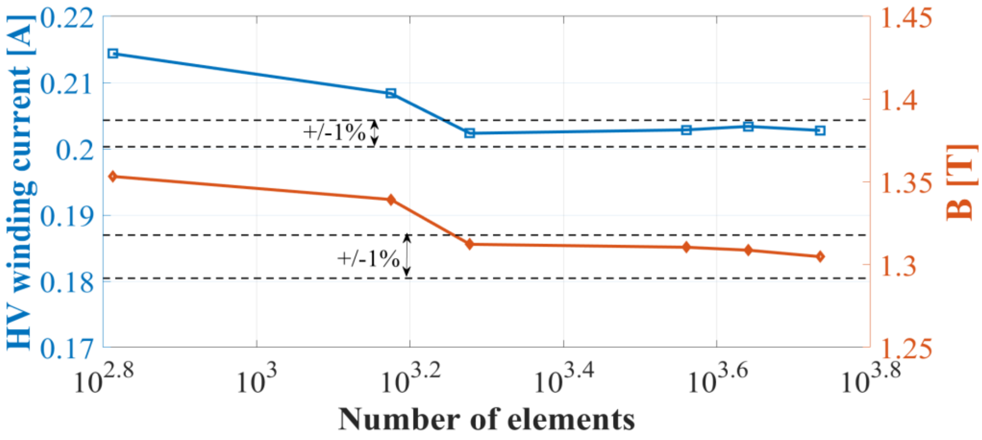

Figure 3.17 Convergence of a global metric (blue) and a local metric (red)

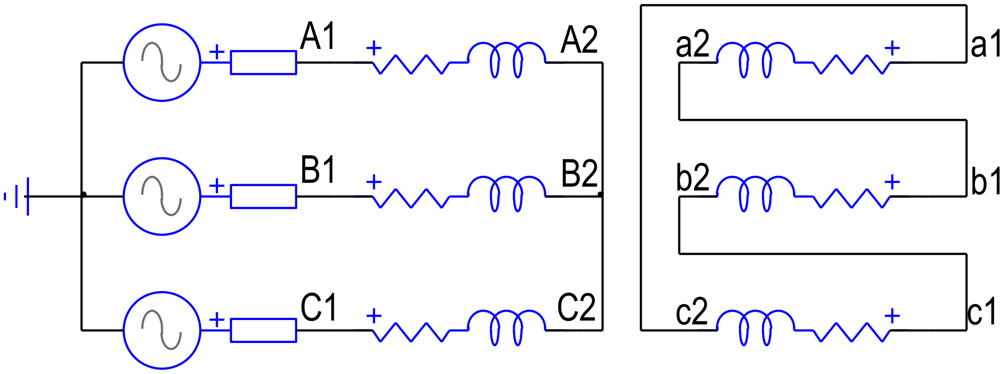

Figure 3.18 Circuit for open-circuit test, transformer with Y-Delta connection

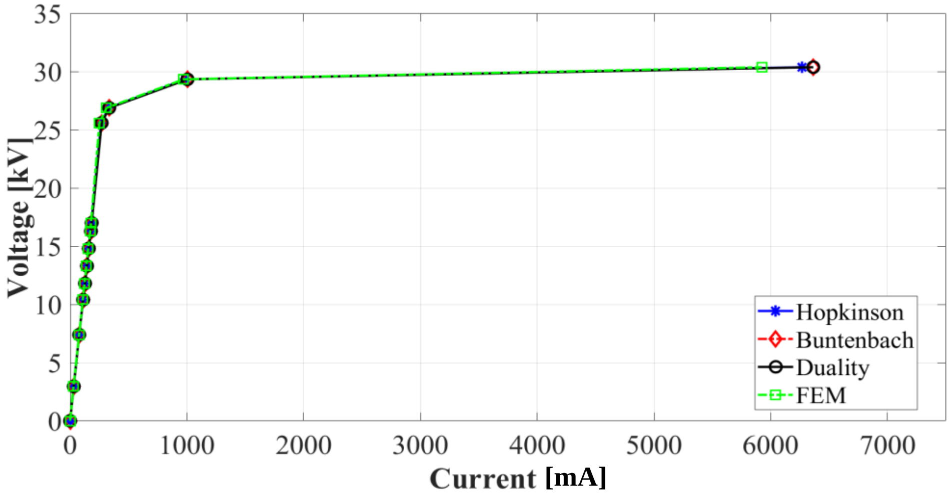

Figure 3.19 V-I characteristic for open-circuit test

Table 3.3 Accuracy Analysis for HBD-circuits for open-circuit condition in both linear and saturated operating points, FEM is the reference.

Model	nRMSE (%)	
	Operating Condition	
	Linear	Saturated
Hopkinson	1.25	3.31
Buntenbach	1.32	3.62
Duality	1.46	3.50

In addition, as an example, the currents of primary windings for phases a, b, and c are shown in Figure 3.20, Figure 3.21, and Figure 3.22, when the voltage exciting the primary winding is set to 20 kV and the secondary winding is an open-circuit. The results are remarkably similar to those obtained using FEM and include the nonlinear behavior of transformer.

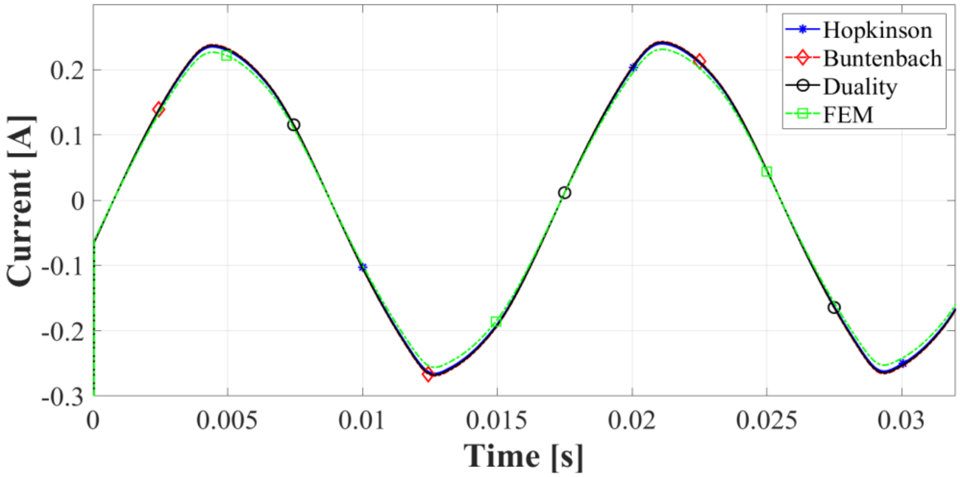

Figure 3.20 Primary winding current of phase-a, open-circuit

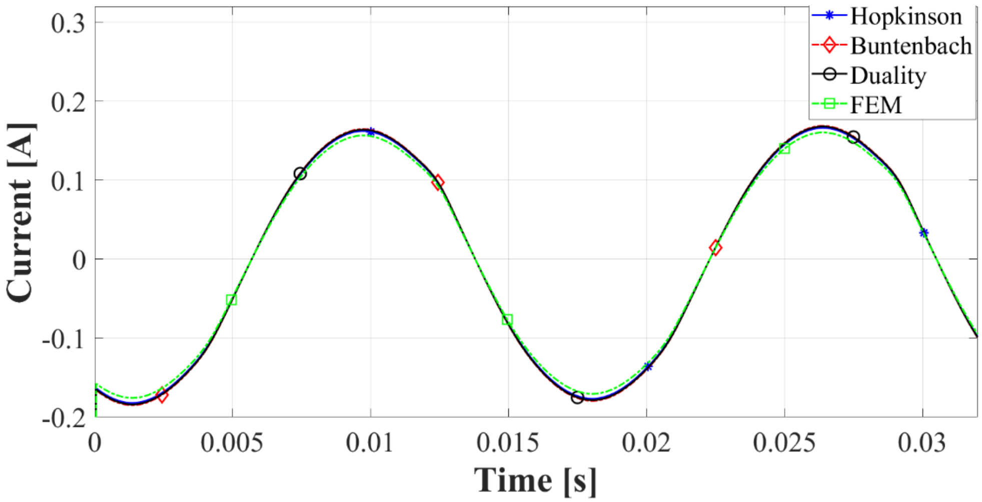

Figure 3.21 Primary winding current of phase-b, open-circuit

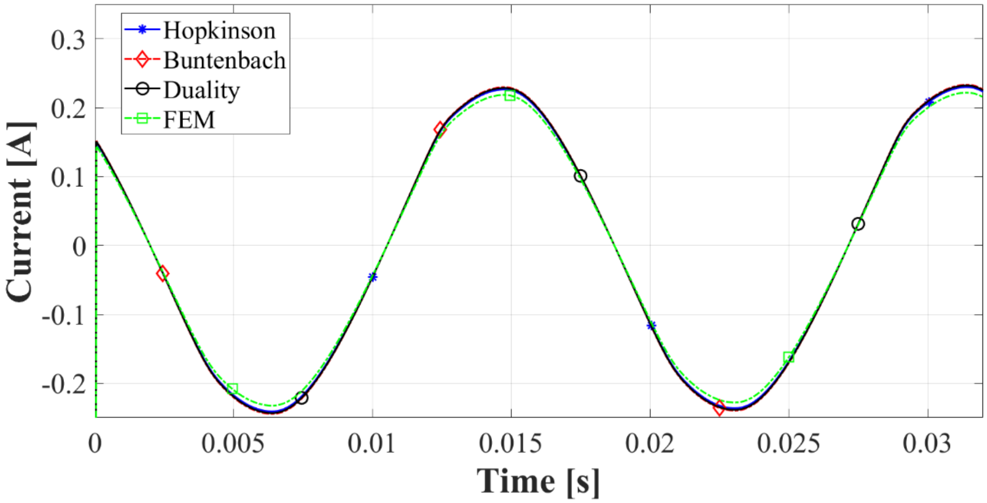

Figure 3.22 Primary winding current of phase-c, open-circuit

Second, as shown in Figure 3.23, the secondary winding is short-circuited in order to obtain short-circuit results. In Figure 3.24, voltage-current characteristics obtained by HBD-circuits are compared to those determined from FEM. By applying the normalised root mean square error (nRMSE) to the voltage-current characteristic generated by each method and comparing it to FEM results, Table 3.4 is derived to evaluate the accuracy of each method.

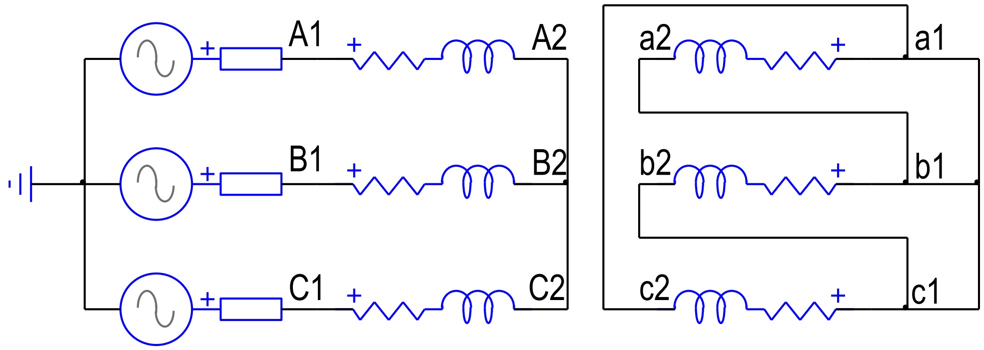

Figure 3.23 Circuit for short-circuit test, transformer with Y-Delta connection

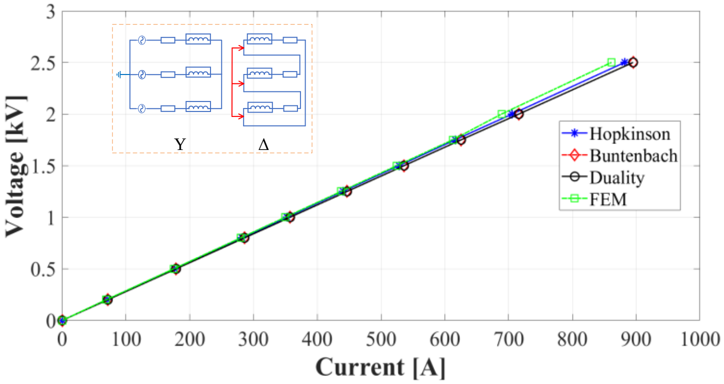

Figure 3.24 V-I characteristic while short-circuiting the secondary side

Table 3.4 Accuracy analysis for HBD-circuits for short-circuit condition, FEM is the reference

Model	Hopkinson	Buntenbach	Duality
nRMSE (%)	1.96	2.01	2.14

Figure 3.25, Figure 3.26, and Figure 3.27 show the currents for the three phases of the primary winding when its excitation voltage is set to $1000\ V$ and the secondary winding is short circuited. The HBD-circuit results are very similar to each other and to FEM.

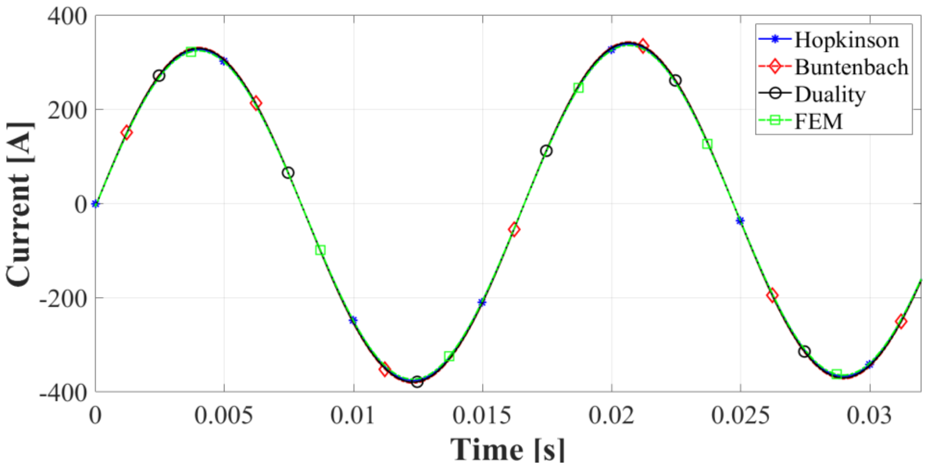

Figure 3.25 Primary winding current in phase-a, during short-circuit

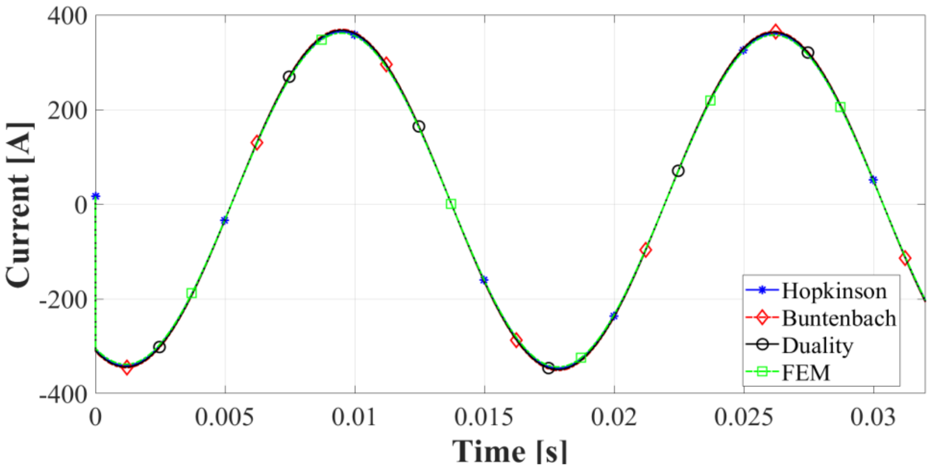

Figure 3.26 Primary winding current in phase-b, during short-circuit

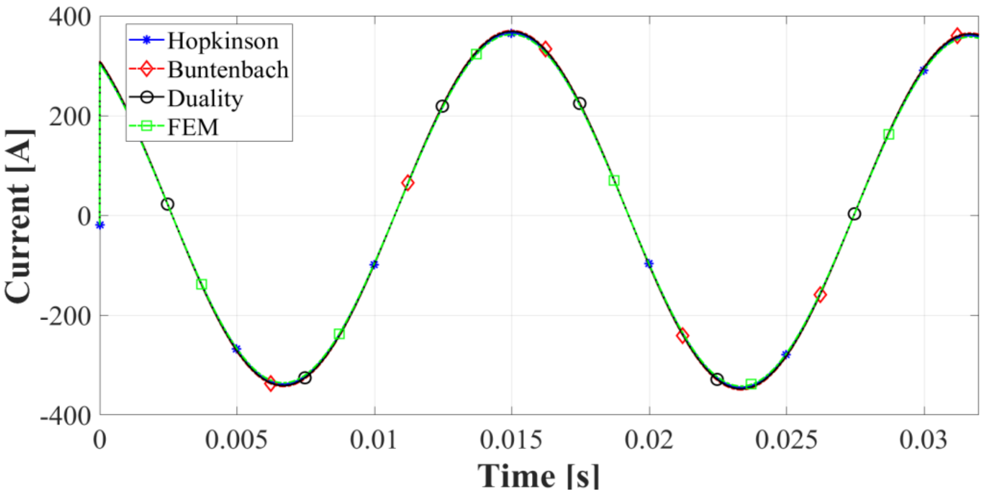

Figure 3.27 Primary winding current in phase-c, during short-circuit

HBD-circuits, like FEM, can reflect the internal behavior of magnetic devices. As an example, as seen in Figure 3.26, the magnetic flux of a local spot which is located exactly in the middle of the left air gap between HV and LV windings of phase A is obtained by HBD-circuits and FEM. By applying the normalised root mean square error (nRMSE) to the current curves generated by each method and comparing it to FEM results, Table 3.5 is derived to evaluate the accuracy of each method in local representation of magnetic fluxes.

Additionally, the HBD-circuits have an interesting feature that allows them to represent flux distributions in various places of the transformer and under various operating conditions. Figure 3.27, Figure 3.28, and Figure 3.29 show flux distributions for short-circuit operating condition derived by Hopkinson, Buntenbach and duality, respectively. It is clear that HBD-circuits are able to provide a good resolution of flux paths in such a way that not only the general view of flux distributions, which in short-circuit conditions are confined more between two windings, but also various details, such as the flux distributions in the edges, have been successfully represented.

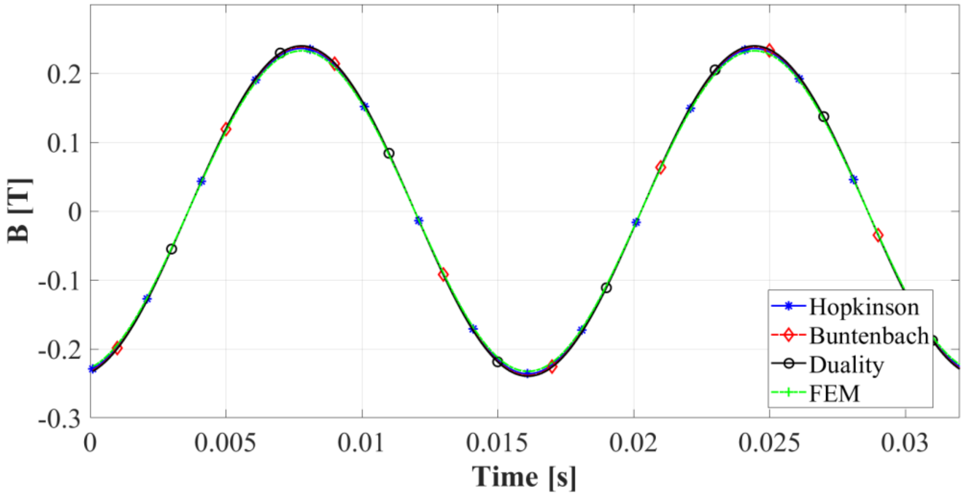

Figure 3.28 Magnetic flux B regarding a point of gap between the windings of phase A

Table 3.5 Accuracy analysis for HBD-circuits for local point representation, FEM is the reference

Model	Hopkinson	Buntenbach	Duality
nRMSE (%)	2.08	2.16	2.21

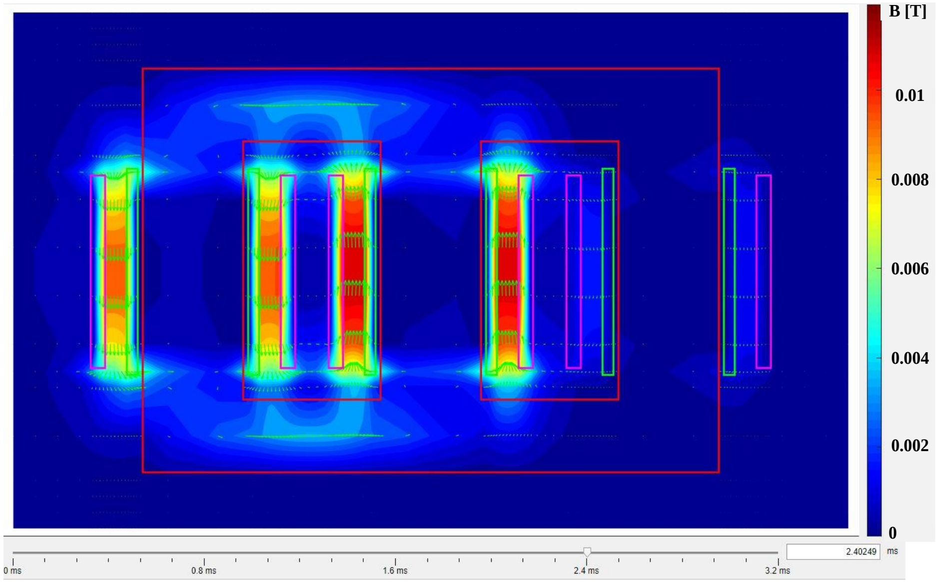

Figure 3.29 Flux distribution for short-circuit condition derived by Hopkinson Analogy

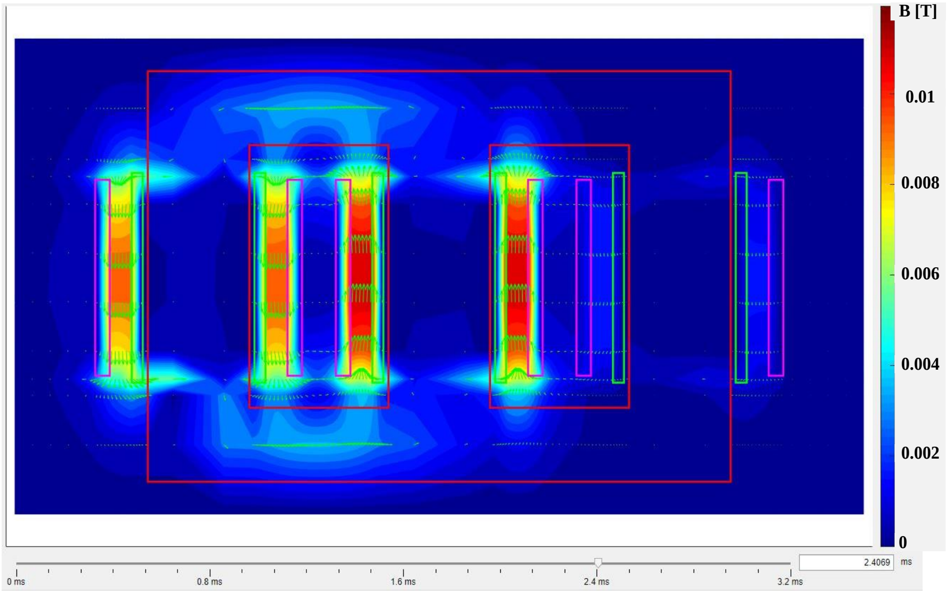

Figure 3.30 Flux distribution for short-circuit condition derived by Buntenbach Analogy

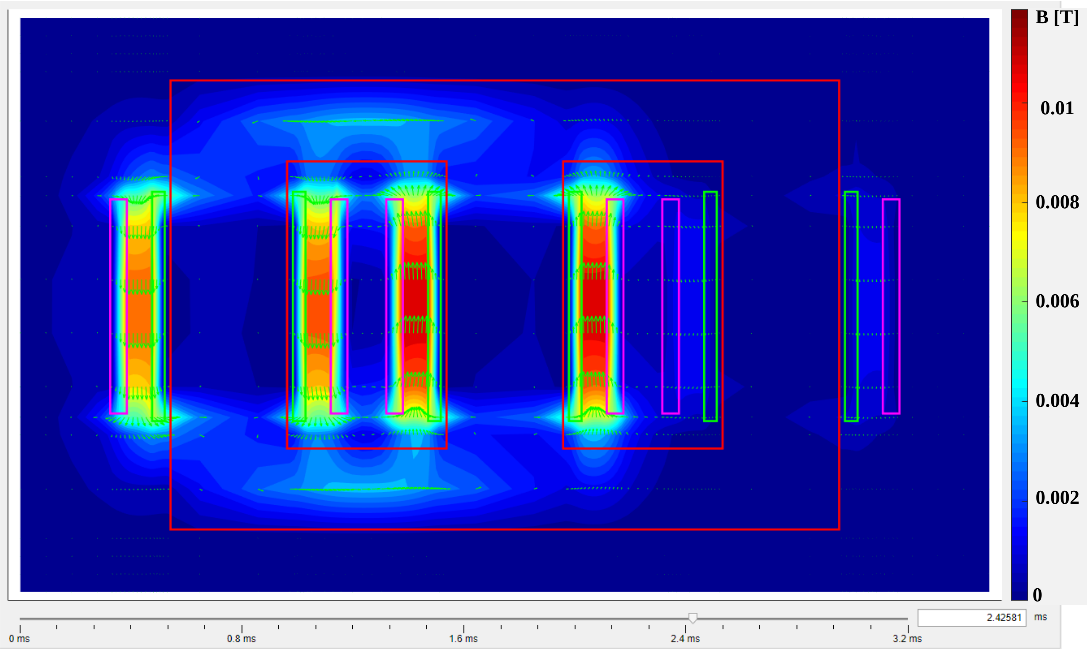

Figure 3.31 Flux distribution for short-circuit condition derived by Duality principle

To demonstrate that the HBD-circuits can be used to study transformer electromagnetic transients, a simple example of energizing the transformer connected to an RL impedance ($R_L = 10\text{m}\Omega, L_L = 10\text{m}\Omega$), and a voltage source with an amplitude of 14 kV (the circuit has been shown in Figure 3.32) is investigated. The 3 phases are energized simultaneously. The inrush currents generated by HBD-circuits are compared to those from FEM. The phase-b inrush currents are shown in Figure 3.33. The maximum relative error between HBD-circuits and FEM is shown in Table 3.6.

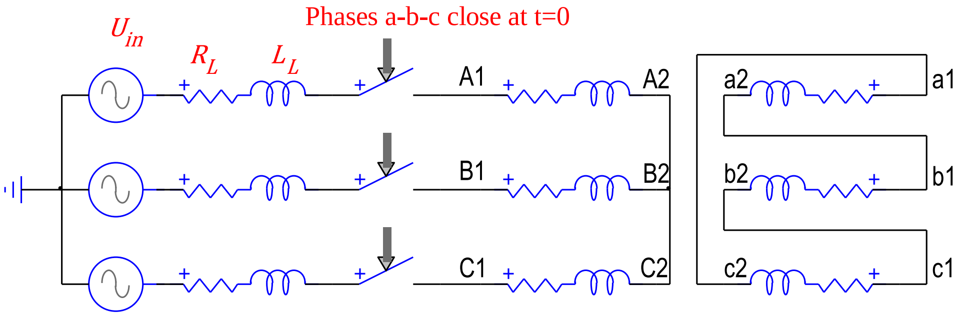

Figure 3.32 Circuit for transformer energization, Y-Delta connection

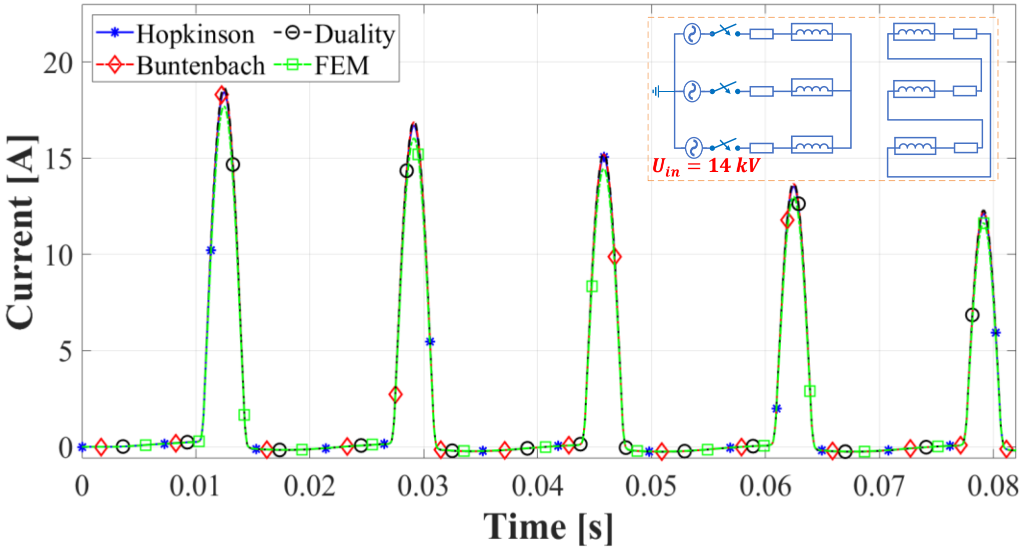

Figure 3.33 Inrush currents, solved with HBD-circuits and FEM

Table 3.6 Accuracy analysis for HBD-circuits in representing energization transients, FEM is the reference

Model	Hopkinson	Buntenbach	Duality
Maximum relative error (%)	3.27	3.29	3.26

Finally, the capacity of HBD-circuits to represent internal faults is demonstrated. To begin, only the phase in the middle column of the core is energized to validate the accuracy of HBD-circuits in representing the leakage flux paths during internal faults. Transformer windings are multi-layered in this case, with ten layers in the high-voltage winding. Here, an internal fault with resistance R_f between the second and third layers of the HV winding is investigated. The HV winding is connected at its nominal voltage in this case, whereas the LV winding is connected to a resistive load of $R_{load} = 1.3681\ \Omega$ which makes nominal current to flow through the transformer. The currents of the healthy and faulty sections of the HV winding, denoted by I_p and I_f, as well as the current of the LV winding, denoted by I_s, are determined using HBD-circuits and FEM for various values of R_f. First for an example, where R_f is set to 3 Ω, I_p, I_s, and I_f are derived in Figure 3.34, Figure 3.35, and Figure 3.36, respectively. In addition, for various fault resistances, Figure 3.37 illustrates the current of the faulty section of the HV winding derived using HBD-circuits and

FEM. Table 3.7 is used to evaluate the accuracy of each method in fault representation by deriving the root mean square (rms) value of the percent error between the fault currents derived by each HBD-circuits and the fault currents derived by FEM as the fault resistance is varied from 1 Ω to 100 kΩ.

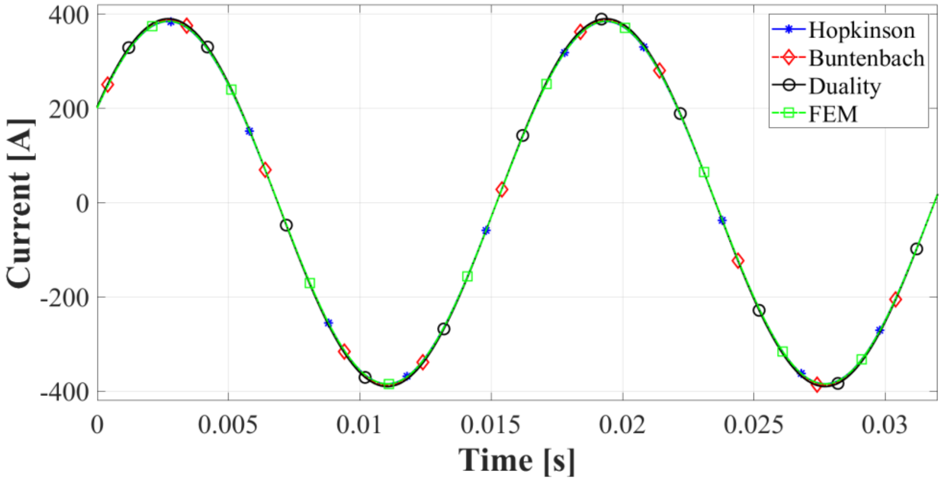

Figure 3.34 Current of healthy part of HV winding during an inter-turn fault

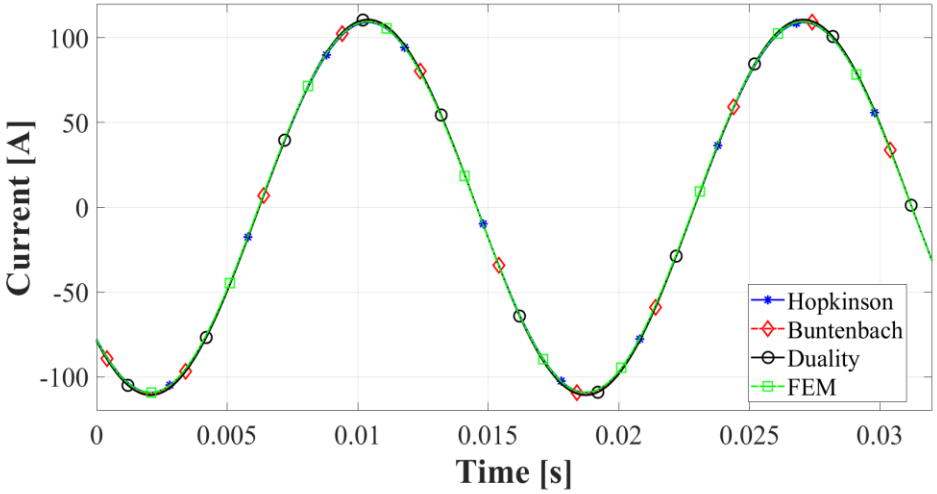

Figure 3.35 Current of faulty part of HV winding during an inter-turn fault

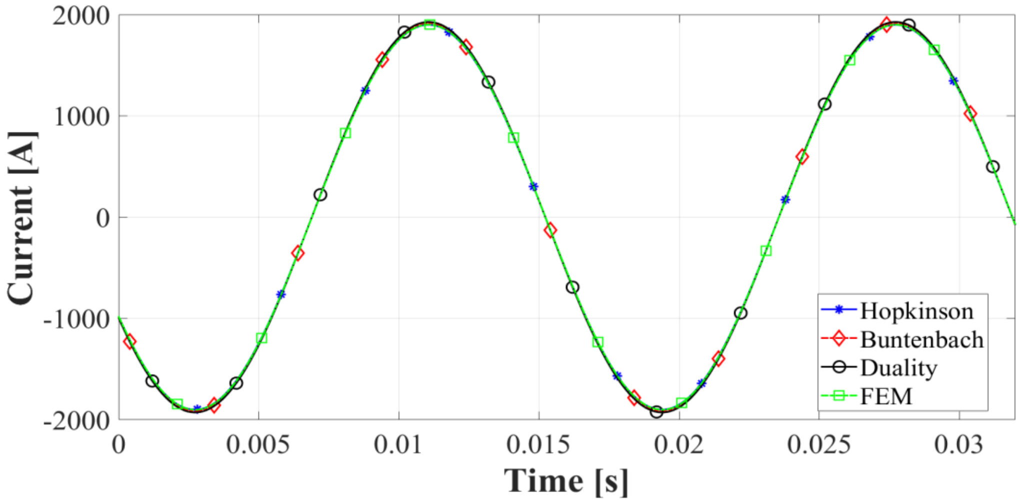

Figure 3.36 Current of secondary winding during an inter-turn fault

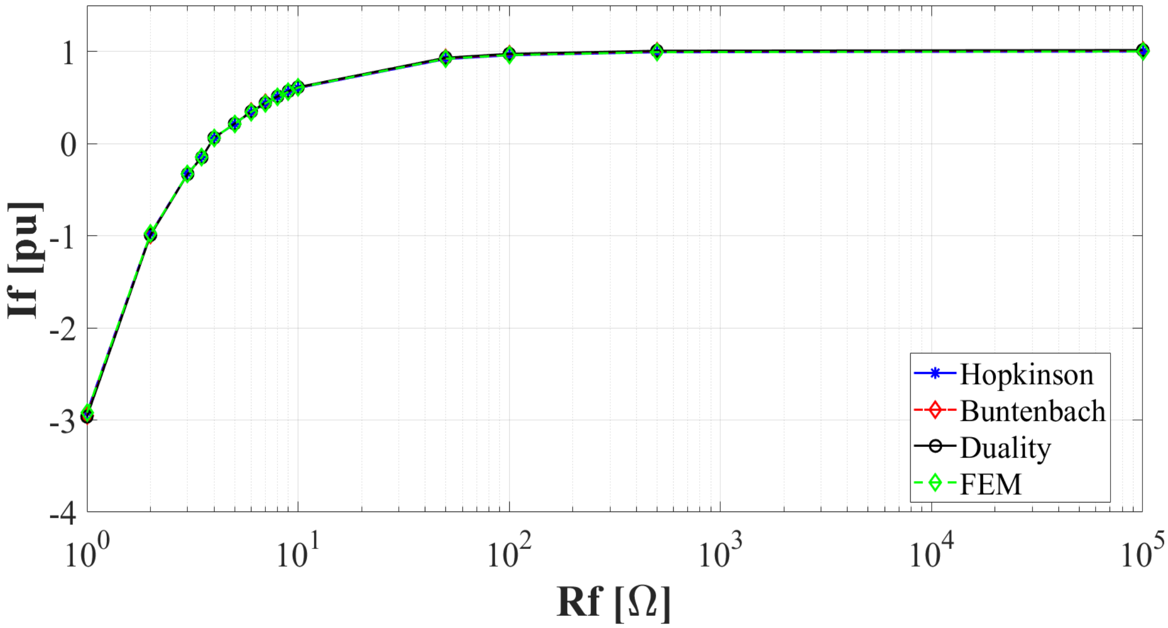

Figure 3.37 Per unit current of the affected winding for different fault resistances

The computational speed of HBD-circuits is a significant characteristic that should be compared to FEM. This was accomplished by running simulations for 32 ms with a 1 μs time step and using a mesh size of 2848 for HBD-circuits and 3292 for FEM. As shown in Figure 3.38, HBD-circuits are about seven to eight times faster than FEM under linear operation conditions. Furthermore, it can be seen that HBD-circuits are approximately three times faster than FEM in saturated operation conditions with a significant degree of nonlinearity. HBD-circuits are computationally faster than

FEM because they solve equations that are simpler, as HBD-circuits consider the flux path in two directions instead of several directions as FEM does. Furthermore, unlike HBD-circuits, where the direction of the flux path is known prior to application, the direction of the flux path is one of the unknowns in FEM. Additionally, it can be observed that Hopkinson is the fastest HBD-circuit, which is primarily due to the fact that the number of ordinary differential equations (ODEs) in Hopkinson is significantly less than in Buntenbach and duality, owing to the use of resistors rather than capacitors and inductors. It is worth noting that the speed advantage of HBD-circuits over FEM is most noticeable when modelling transformers in large electric power systems.

Table 3.7 Accuracy Analysis for HBD-circuits for representing faults, FEM is the reference

Model	Hopkinson	Buntenbach	Duality
RMS (%)	1.87	1.94	2.08

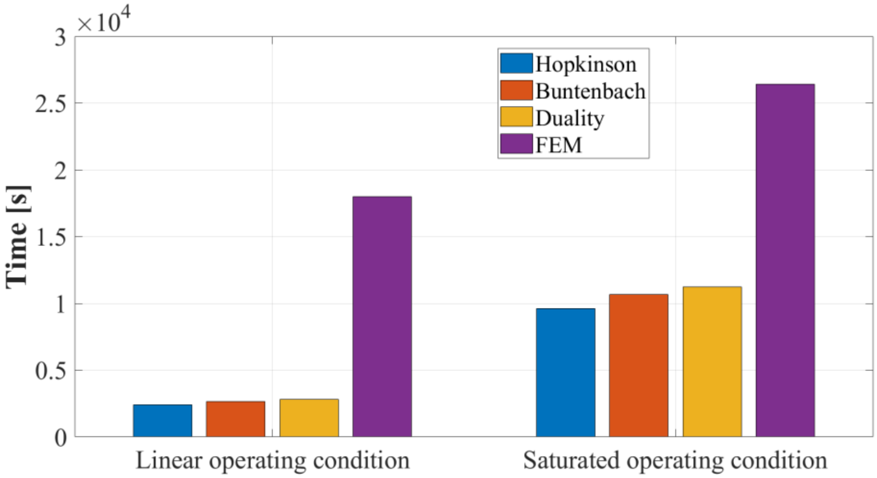

Figure 3.38 HBD-circuits vs. FEM in terms of computation time

3.5 Conclusion

In this chapter, HBD-circuits were improved to represent transformers. The creation of three HBD-circuits for a simple single-phase transformer with two windings were first explained, and the number of meshes was set to a small, fixed number in this part. Then HBD-circuits for a three-phase transformer and a customizable number of meshes were improved. It was described in detail how elements are defined, their values are determined, and how they are connected to each another. We have also shown how HBD-circuits can be used to simulate transformer internal faults. To achieve this purpose, the faulty winding was split into distinct sections based on the type of fault, and each section was treated as a separate winding. In the case of the faulty transformer, it was also outlined how new element types are defined, their values are determined, and how they are connected to each another. Different cases were studied in order to verify the accuracy of HBD-circuits in depicting both internal and external transformer behaviour. First, the models were tested for their ability to represent open-circuit and short-circuit transformer characteristics. They were then shown to be capable of accurately depicting magnetic flux distributions in transformers.

HBD-circuits were used to replicate the energization of a transformer, demonstrating that they can present transformer behaviour not only in steady-state, but also in transient conditions. It was also shown that the proposed method can be utilized to represent internal faults in transformers in such a way that not only can leakage flux path be accurately represented, but also the effect of the core can be considered. The derived results were validated using FEM. The error of less than 4% in most situations.

CHAPTER 4 DOUBLE-2D DISTRIBUTED CIRCUIT-BASED METHODS

4.1 Introduction to 3D methods

4.1.1 Motivation

In Chapter 2 and Chapter 3, distributed circuit-based methods were investigated in the 2D dimension, and they demonstrated good accuracy when compared to 2D FEM. However, when compared to 3D FEM, there are major differences in how they represent certain behaviours. Here, the results obtained using the Hopkinson technique, 2D FEM, and 3D FEM are compared for both the open-circuit and short-circuit for the transformer shown in Figure 3.5. For open-circuit, the circuit shown in Figure 3.18 is used and the curves shown in Figure 4.1 are derived. And for short-circuit, the circuit shown in Figure 3.23 is used and the curves shown in Figure 4.2 are derived. Figure 4.1 shows that the open-circuit findings for Hopkinson 2D, FEM 2D, and FEM 3D are nearly identical, especially when the transformer does not go into deep saturation. This is mainly due to this fact that in open-circuit condition, the majority of the flux goes into the core, and due to the core-type structure of the transformer, the magnetic flux paths in the core can approximately been covered in 2D models (FEM 2D and Hopkinson 2D). The higher differences seen for deeply saturated operating conditions are due to 2D models' failure to represent fluxes straying into the air under these operating conditions. According to the short-circuit curves in Figure 4.2, Hopkinson 2D results, which are substantially identical to FEM 2D results, are significantly different from FEM 3D results. Because the majority of the magnetic flux is restricted to the area between the HV and LV windings during the short-circuit, 2D models cannot account for this. It is observed that the 2D circuit-based methods proposed in Chapter 2 and Chapter 3 can consider only 2D effects of magnetic fields, even though the magnetic field in many magnetic components, such as transformers, is distributed in three dimensions (3D), and for some studies, it is vital to consider 3D effects for these components, and as a result, 3D approaches should be applied. In this chapter, an approach is presented to improve proposed circuit-based methods in earlier chapters by taking into account 3D effects. Because all three HBD-circuits provide identical results and are equal, the proposed approach is only discussed for Hopkinson Analogy.

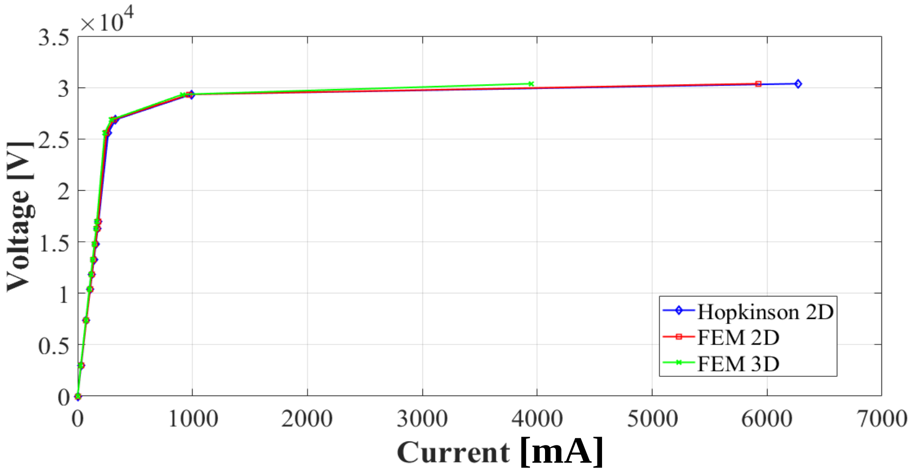

Figure 4.1 V-I characteristic for open-circuit achieved by Hopkinson 2D model, FEM 2D, and FEM 3D

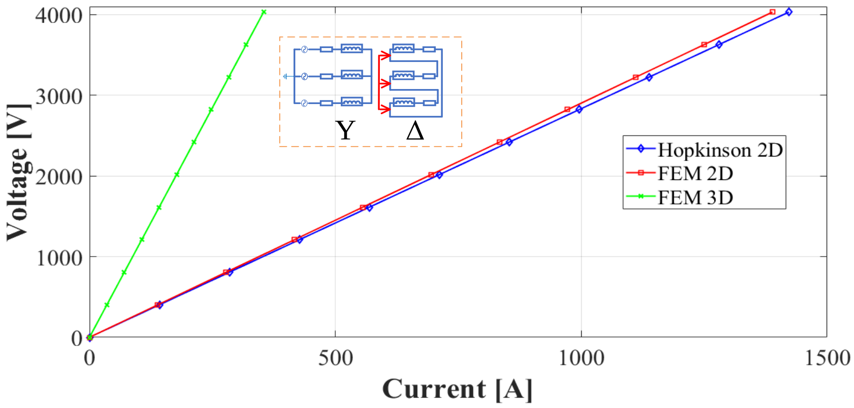

Figure 4.2 V-I characteristic while short-circuiting the secondary side achieved by Hopkinson 2D model, FEM 2D, and FEM 3D

4.1.2 Double-2D concept

In power system applications, 3D FEM has not been interested due to the following reasons: first, the geometry can be complex in some circumstances; second, they can be time demanding; and third, they require fast computer sources. [80] presented a method, dubbed "Double 2D," for calculating energy and losses in 3D structures using 2D FEM solvers while accounting for 3D effects. They planned to reduce simulation time while also simplifying problem definitions, which involve defining geometry, assigning boundary conditions, and the solving technique. They used 2D FEM to solve two 2D problems (Double-2D) in order to account for field effects in 3D structures. On EE cores, the "Double 2D" approach divides the magnetic component's windings into two parts. Because the magnetic field of each part is distributed in one different plane, 2D FEA solvers can be utilized to analyze it. Figure 4.3 shows how a 3D structure in (a) can be divided into two parts in (b), each of which can be implemented using double 2D simulations in (c). The assumption behind the Double-2D technique is that the field distribution in the part of the structure depicted on the left side of (b) is primarily stored in the core. However, the field distribution in the right side of (b) is mostly stored in the air. Because both planes illustrated in (c) are perpendicular, the dotted product of the fields distribution in each of them is zero, and therefore the interaction of both simulations is null. However, in this method, the influence of the conductor corners is ignored, which is a legitimate assumption in some instances.

They showed that when the problem is only presented in a single 2D space and the axisymmetric condition is assumed, the accuracy is poor. The accuracy of the solution improved dramatically when they used a Double-2D technique to address the problem. They showed that the error caused by a single 2D axisymmetric simulation to compute the magnetic energy in an EE core is rather large (34 percent), but that the error produced by the "Double 2D" technique is little (1.6 percent).

4.2 Explanation of the double 2D methodology

In this study, circuit-based methods are applied for the first time to implement double 2D approaches. Single-phase and three-phase transformers are used as case studies for the proposed double-2D circuit-based approach. The main purpose of this method is to create a quasi-3D detailed model of the transformer in EMT-type software by utilizing existing elements in this software.

Double 2D circuit-based approach divides the 3D structure into two 2D structures in two 2D perpendicular planes, each of which is modelled using circuit-based methods, similar to double-2D FEM. Figure 4.4 shows two cross sections of these two 2D structures, one referred to as the inside transformer window (IW) and the other as the outside transformer window (OW). This method creates a circuit-based model for each of these main cross-sections. Creation of models is only explained for the right half of the cross-sections due to vertical symmetry. The two models are coupled after meshing, indexing, determining parameters, and establishing internal connections.

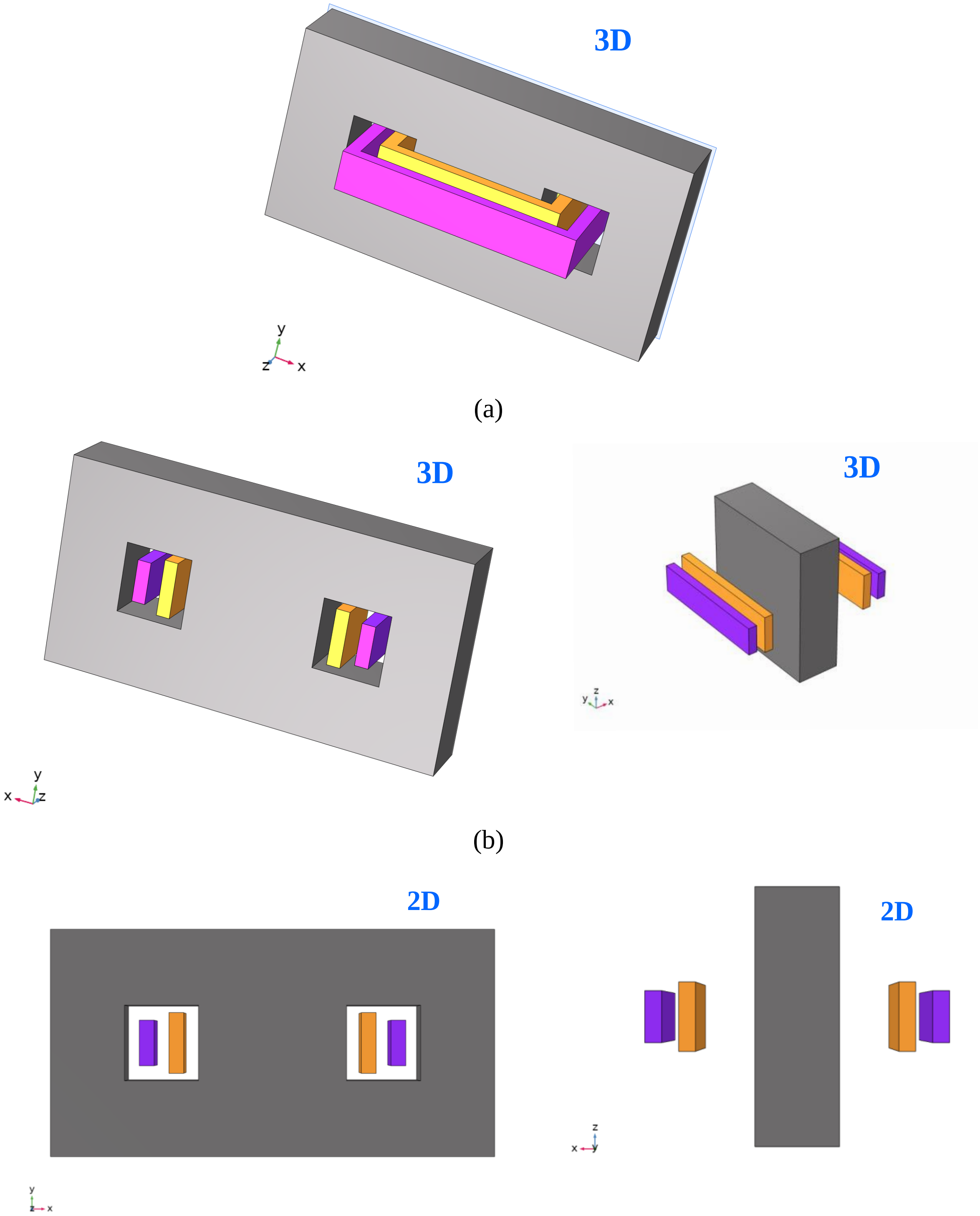

(a)

(b)

(c)

Figure 4.3 Study of transformer with 3D EE structure by means of double 2D. (a) 3D EE structure, (b) Division of the windings, (c) 2D simulations related to the divided parts

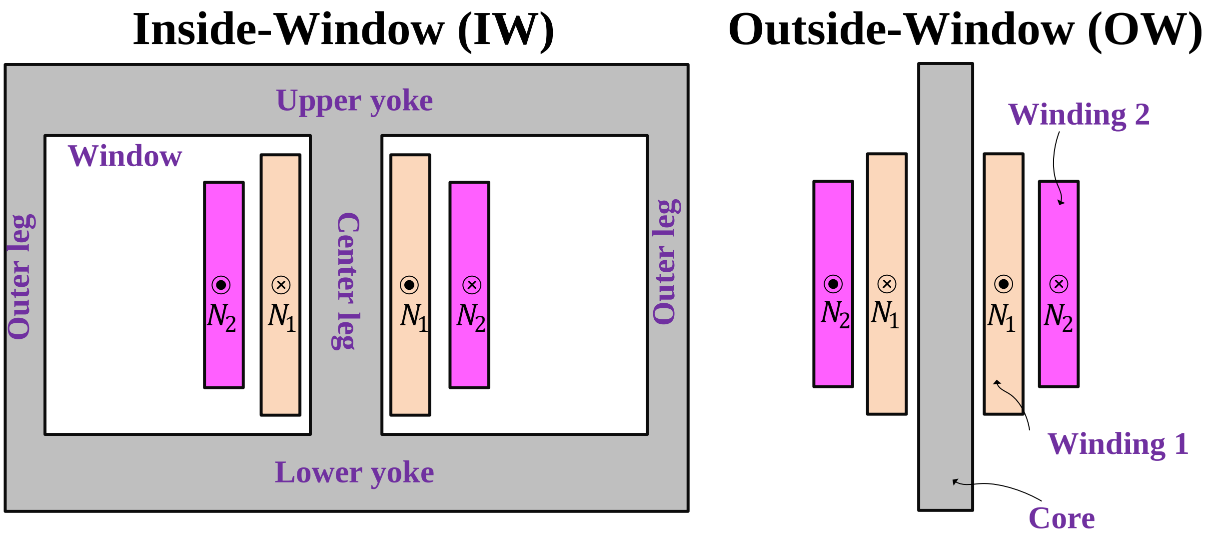
Inside-Window (IW)

Outside-Window (OW)

(a) (b)

Figure 4.4 Cross sections of "Double-2D" model for a single-phase transformer (a) Inside window (IW). (b) Outside window (OW)

4.2.1 Meshing

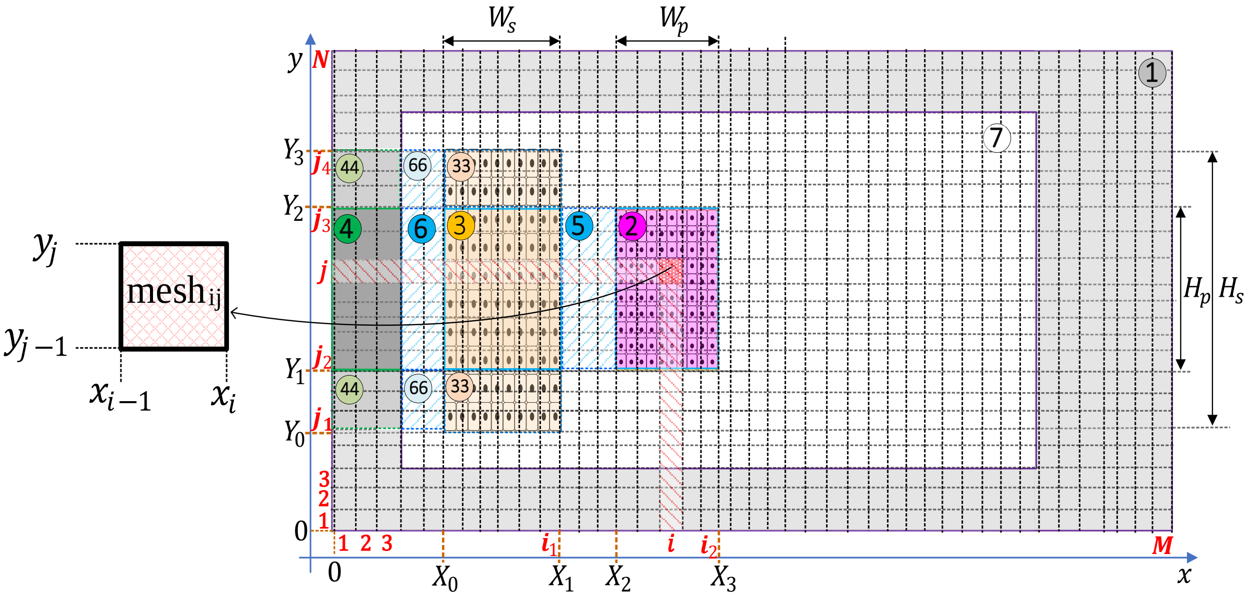

Figure 4.5 Cross-section of left half of the core on IW plane

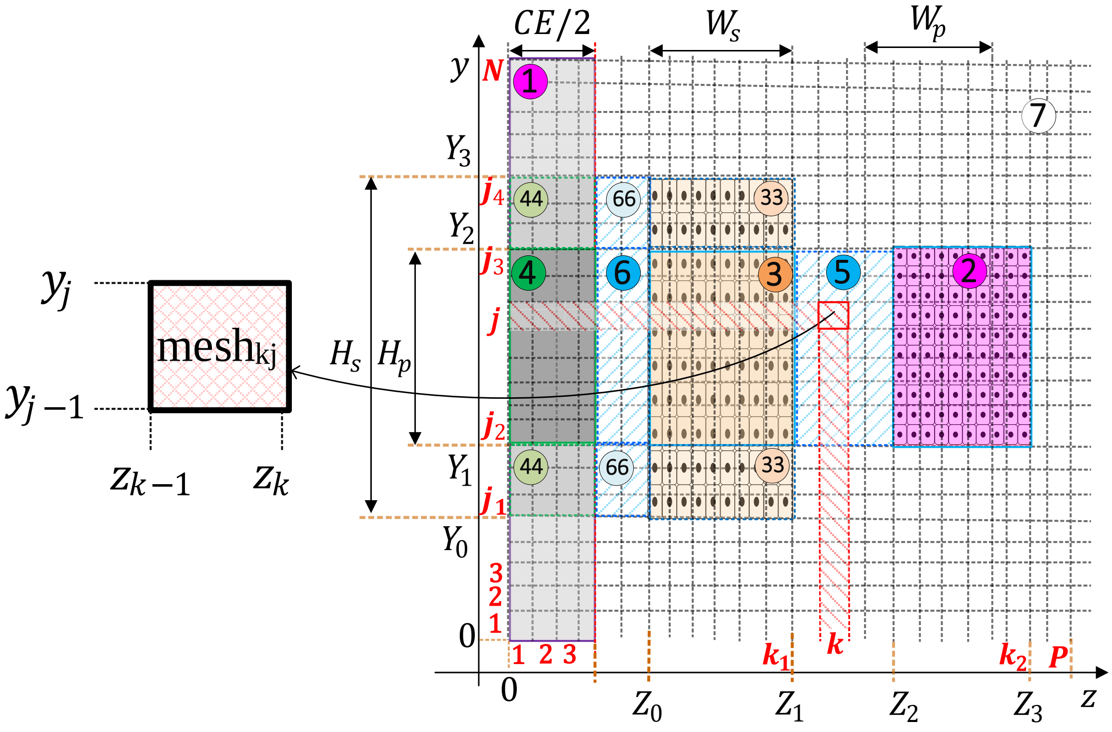

Figure 4.6 Cross-section of left half of the core on OW plane (y-z)

To begin, for each cross section, the space is subdivided into meshes based on the required accuracy. Figure 4.5 shows the mesh created for IW and Figure 4.6 shows the mesh created for OW. Then, the equivalent electric circuits are generated for each mesh. As noted in section 3.2.1, all elements of both IW and OW meshes are categorized into four general types (Type-A, Type-B, Type-C, and Type-D). The equivalent circuits of elements of IW cross section mesh are the circuits which have been shown in Figure 4.7. But for the elements of OW cross section mesh, the circuits shown in Figure 4.8 are derived. The meshed cross-sections in Figure 4.5 and Figure 4.6 have been divided into regions, each of which contains one of these element types. In Figure 4.5 and Figure 4.6, parts 1 and 7 are made up of Type-A elements, parts 2 and 5 are made up of Type-B elements, parts 3, 4, and 6 are made up of Type-C elements, and parts 33, 44, and 66 are made up of Type-D elements.

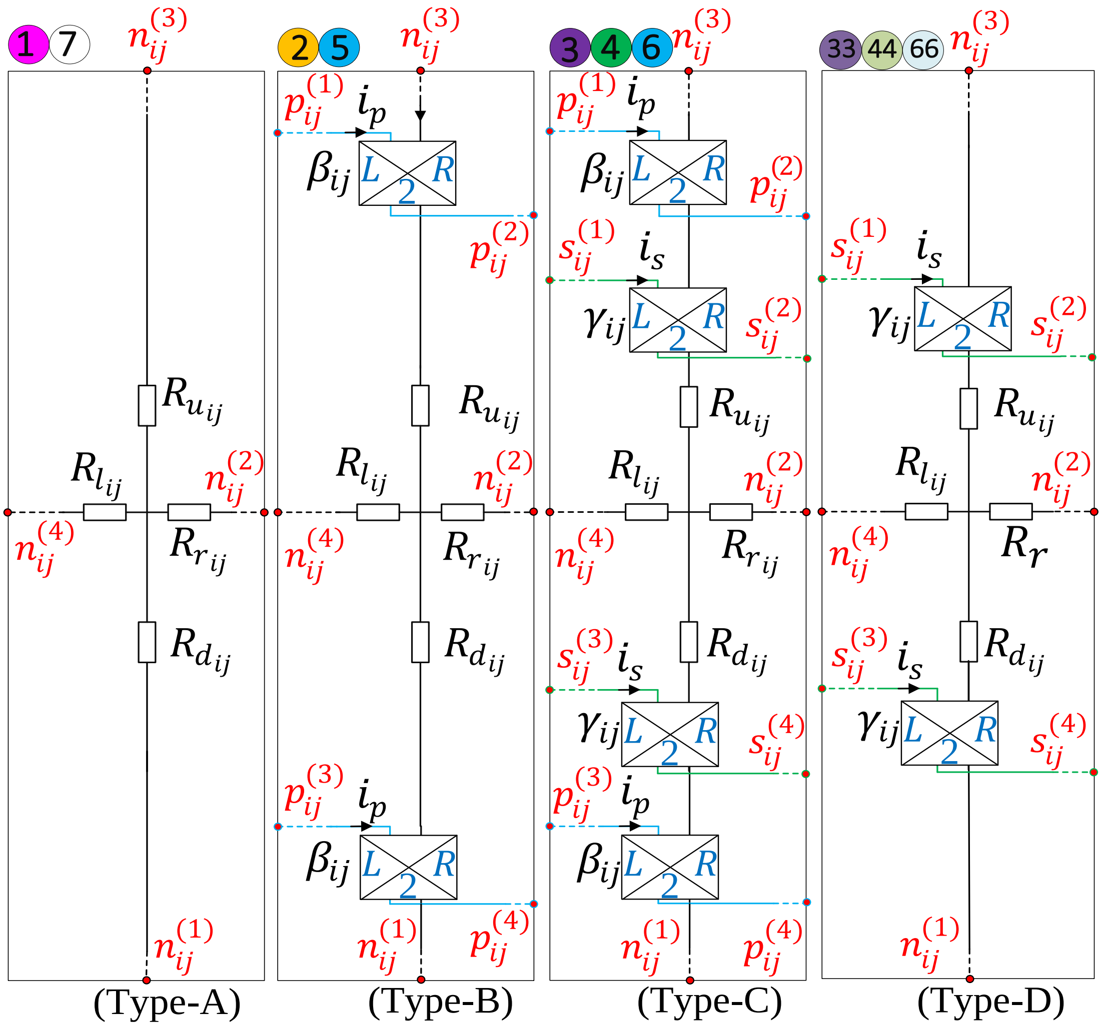

Figure 4.7 Circuits based on Hopkinson Analogy for four cell types (A, B, C, and D) related to mesh of IW cross section shown in Figure 4.5

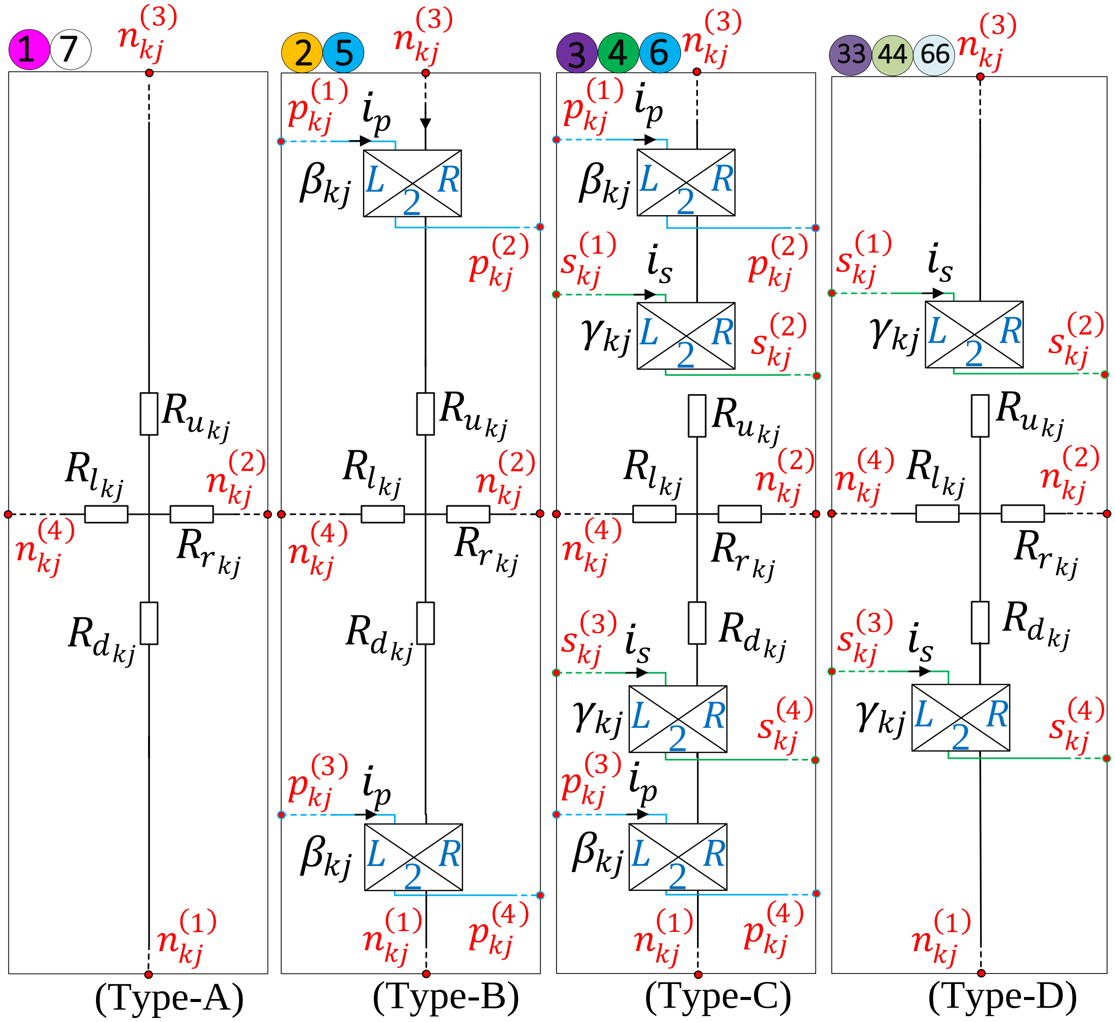

Figure 4.8 Circuits based on Hopkinson Analogy for four cell types (A, B, C, and D) related to mesh of OW cross section shown in Figure 4.6

4.2.2 Determination of circuit parameters

As it was mentioned in section 3.2.2, the circuit parameters for each element of both meshes are determined by applying distributed Ampere’s and Faraday's laws. The coupling factors β_{ij} and γ_{ij}, which are related to the mutators of the HV and LV windings of the element in i^{th} column and j^{th} row of the mesh presented in Figure 4.5, are given by (4.1) and (4.2) respectively. The coupling factors β_{kj} and γ_{kj}, which are related to the mutators of the HV and LV windings of the element in k^{th} column and j^{th} row of the mesh presented in Figure 4.6, are given by (4.3) and (4.4), respectively. Where N_p and N_s represent the number of turns in HV and LV winding, respectively. W_p and W_s are the widths of the HV and LV windings, respectively, and H_p and H_s are the heights of the HV and LV windings. x_{i-1}, x_i, y_{j-1} and y_j are the horizontal and vertical coordinates of the cell placed in i^{th} column and j^{th} row of the mesh presented in Figure 4.5. z_{k-1}, z_k, y_{j-1}, and y_j are the horizontal and vertical coordinates of the cell placed in k^{th} column and j^{th} row of the mesh presented in Figure 4.6. X_2, X_3, Y_1, and Y_2 are the horizontal and vertical coordinates of the HV winding in mesh of Figure 4.5 and X_0, X_1, Y_0 and Y_3 are the horizontal and vertical coordinates of the LV winding in mesh of Figure 4.5. Z_2, Z_3, Y_1 and Y_2 are the horizontal and vertical coordinates of the HV winding in mesh of Figure 4.6 and X_0, X_1, Y_0 and Y_3 are the horizontal and vertical coordinates of the LV winding in mesh of Figure 4.6.

$$\beta_{ij} = \begin{cases} \dfrac{N_p\left(y_j - y_{j-1}\right)}{2W_pH_p}\left(\dfrac{x_{i-1}+x_i}{2} - X_0\right) & x_{i-1} \geq X_2, x_i \leq X_3, y_{j-1} \geq Y_1, y_j \leq Y_2 \\ \dfrac{N_p\left(y_j - y_{j-1}\right)}{2H_p} & x_{i-1} \geq 0,\ x_i \leq X_2,\ y_{j-1} \geq Y_1,\ y_j \leq Y_2 \end{cases} \tag{4.1}$$

$$\gamma_{ij} = \begin{cases} \dfrac{N_s\left(y_j - y_{j-1}\right)}{2W_sH_s}\left(\dfrac{x_{i-1}+x_i}{2} - X_2\right) & x_{i-1} \geq X_0,\ x_i \leq X_1,\ y_{j-1} \geq Y_0,\ y_j \leq Y_3 \\ \dfrac{N_s\left(y_j - y_{j-1}\right)}{2H_s} & x_{i-1} \geq 0,\ x_i \leq X_0,\ y_{j-1} \geq Y_0,\ y_j \leq Y_3 \end{cases} \tag{4.2}$$

$$\beta_{kj} = \begin{cases} \dfrac{N_p(z_k - z_{k-1})}{2W_pH_p}\left(\dfrac{z_{k-1}+z_k}{2} - Z_0\right) & z_{k-1} \geq Z_2, z_k \leq Z_3, y_{j-1} \geq Y_1, y_j \leq Y_2 \\ \dfrac{N_p\left(y_j - y_{j-1}\right)}{2H_p} & z_{k-1} \geq 0,\ z_k \leq Z_2,\ y_{j-1} \geq Y_1,\ y_j \leq Y_2 \end{cases} \tag{4.3}$$

$$\gamma_{kj} = \begin{cases} \dfrac{N_s\left(y_j - y_{j-1}\right)}{2W_sH_s}\left(\dfrac{z_{k-1}+z_k}{2} - Z_2\right) & z_{k-1} \geq Z_0,\ z_k \leq Z_1,\ y_{j-1} \geq Y_0,\ y_j \leq Y_3 \\ \dfrac{N_s\left(y_j - y_{j-1}\right)}{2H_s} & z_{k-1} \geq 0,\ z_k \leq Z_0,\ y_{j-1} \geq Y_0,\ y_j \leq Y_3 \end{cases} \tag{4.4}$$

The horizontal reluctances ($R_{r_{ij}}$ and $R_{l_{ij}}$) and vertical reluctances ($R_{u_{ij}}$ and $R_{d_{ij}}$) of elements forming mesh of Figure 4.5 are calculated by

$$R_{r_{ij}} = R_{l_{ij}} = \frac{l}{\mu S} = \frac{\frac{x_i - x_{i-1}}{2}}{\mu_0\left(y_j - y_{j-1}\right) * D_{ij}{}^{(IW)}} \tag{4.5}$$

$$R_{u_{ij}} = R_{d_{ij}} = \frac{l}{\mu_0 S} = \frac{\frac{y_j - y_{j-1}}{2}}{\mu\,(x_i - x_{i-1}) * D_{ij}{}^{(IW)}} \tag{4.6}$$

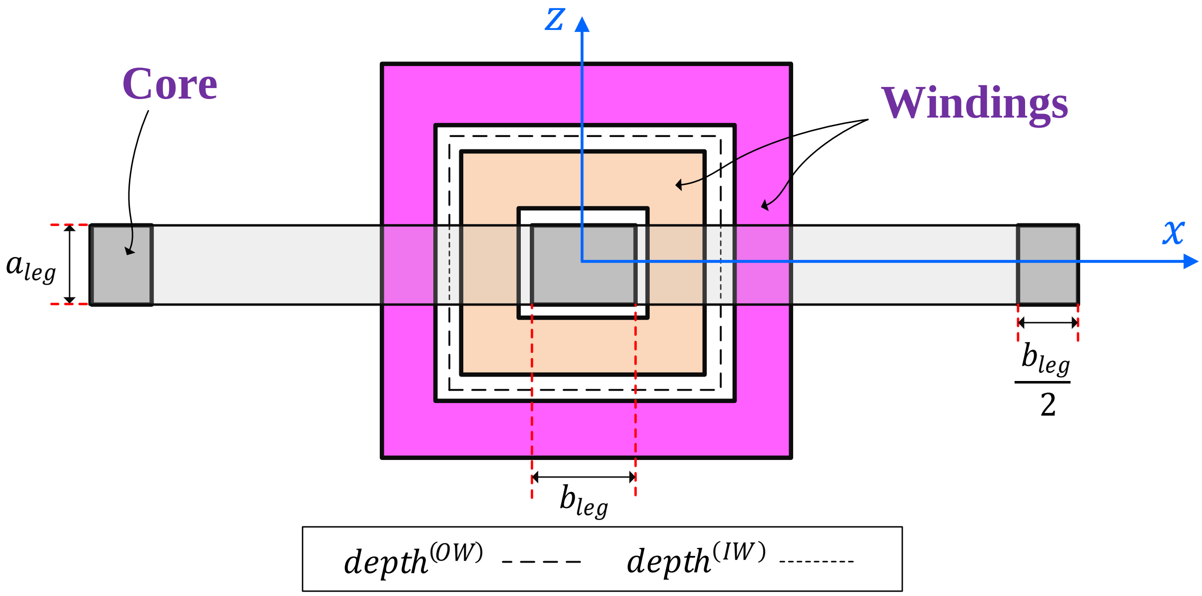

Figure 4.9 The depths of the magnetic flux paths for IW and OW models ($depth_{ij}^{(IW)}$, $depth_{ij}^{(OW)}$)

where μ is the magnetic permeability of the mesh material, and if the material is air or copper, it equals μ_0, but if the material is iron (core), it equals μ_p, which is the slope of the p^{th} segment of the piecewise linear function describing the material's magnetising curve. x_{i-1}, x_i, y_{j-1} and y_j are the horizontal and vertical coordinates of the cell placed in i^{th} column and j^{th} row of the mesh presented in Figure 4.5 and $D_{ij}{}^{(IW)}$ denotes the depth of the flux path represented by that cell. The depth of each mesh $D_{ij}{}^{(IW)}$ is determined using the schematic presented in Figure 4.9, which shows the depth of each cross section.

$$D_{ij}^{(IW)} = \frac{depth^{(IW)}}{2} = \frac{2 \times a_{leg}}{2} = a_{leg} \tag{4.7}$$

where $depth^{(IW)}$ is the length of the magnetic flux path for IW model which has been shown in Figure 4.9. $depth^{(IW)}$ for all meshes equals $2 \times a_{leg}$, where a_{leg} is the z-direction depth of the core. The horizontal reluctances ($R_{r_{kj}}$ and $R_{l_{kj}}$) and vertical reluctances ($R_{u_{kj}}$ and $R_{d_{kj}}$) of elements forming mesh of Figure 4.6 are calculated by

$$R_{r_{kj}} = R_{l_{kj}} = \frac{l}{\mu S} = \frac{\frac{z_k - z_{k-1}}{2}}{\mu \left(y_j - y_{j-1}\right) * D_{kj}{}^{(OW)}} \tag{4.8}$$

$$R_{u_{kj}} = R_{d_{kj}} = \frac{l}{\mu_0 S} = \frac{\frac{y_j - y_{j-1}}{2}}{\mu \left(z_k - z_{k-1}\right) * D_{kj}{}^{(OW)}} \tag{4.9}$$

where μ is the magnetic permeability of the mesh material. z_{k-1}, z_k, y_{j-1} and y_j are the horizontal and vertical coordinates of the cell placed in k^{th} column and j^{th} row of the mesh presented in Figure 4.6 and $D_{kj}{}^{(OW)}$ denotes the depth of the flux path represented by that cell. The depth of each mesh $D_{kj}{}^{(OW)}$ is determined using the schematic presented in Figure 4.9.

$$D_{kj}^{(OW)} = \frac{depth_{kj}^{(OW)}}{2} = \begin{cases} \frac{2b_{leg}}{2} = b_{leg} & z_{k-1} \geq 0, z_k \leq a_{leg}/2 \\ \frac{2b_{leg} + 8\left(\frac{z_k + z_{k-1}}{2} - \frac{a_{leg}}{2}\right)}{2} & z_{k-1} \geq a_{leg}/2 \end{cases} \tag{4.10}$$

where $depth_{kj}^{(OW)}$ is the length of the magnetic flux path for OW model and b_{leg} is the width of the middle column of the transformer which have been shown in Figure 4.9.

4.2.3 Connection of model elements

Following the derivation and assignment of parameters for each element of both the OW and IW models, the elements of each model must now be connected internally before being coupled to the other model and external circuit. Internal connections between IW mesh elements are explained first, then internal connections between elements of the OW mesh.

4.2.3.1 Connection of IW model elements

As it can be observed in the Hopkinson model of the IW element presented in Figure 4.7, nodes $n_{ij}^{(1)}$, $n_{ij}^{(2)}$, $n_{ij}^{(3)}$, and $n_{ij}^{(4)}$ are associated to the magnetic part of the element placed in the i^{th} column and j^{th} row of mesh depicted in Figure 4.5. In Algorithm 4.1, it has been shown how magnetic parts of the IW elements are connected through these nodes.

Algorithm 4.1 Internal Magnetic Connections for IW elements

```
for $j^{*} \leftarrow 1$ to $N^{**}$ do
    for $i^{***} \leftarrow 1$ to $(M^{****})$ do
        if $j < N$ & $i < M$
            connect $(n_{ij}^{(2)}, n_{(i+1)j}^{(4)})$
            connect $(n_{ij}^{(3)}, n_{i(j+1)}^{(1)})$
        elseif $j = N$ & $i < M$
            connect $(n_{ij}^{(2)}, n_{(i+1)j}^{(4)})$
        elseif $j < N$ & $i = M$
            connect $(n_{ij}^{(3)}, n_{i(j+1)}^{(1)})$
        End
    End
end
```

*: j is the row number of the cell.	***: i is the column number of the cell.
**: N is the total number of rows in Figure 4.5.	****: M is total number of columns in Figure 4.5.

To build internal electrical connections between the elements of the IW mesh shown in Figure 4.5, Algorithm 4.2 and Algorithm 4.3 are used. Nodes $p_{ij}^{(1)}$, $p_{ij}^{(2)}$, $p_{ij}^{(3)}$, and $p_{ij}^{(4)}$ are related to the HV winding of the element in the i^{th} column and j^{th} row of Figure 4.5, and they are connected using the approach provided in Algorithm 4.2. The approach given in Algorithm 4.3 is used to connect the nodes $s_{ij}^{(1)}$, $s_{ij}^{(2)}$, $s_{ij}^{(3)}$, and $s_{ij}^{(4)}$ that are related to the LV winding of those elements.

Algorithm 4.2 Electric connections for HV windings in IW model

```
for $j \leftarrow j_2^{*}$ to $j_3^{**}$ do
    for $i \leftarrow (-i_2)^{***}$ to $(i_2^{****} - 1)$ do
        connect $(p_{ij}^{(2)}, p_{(i+1)j}^{(1)})$
        connect $(p_{ij}^{(4)}, p_{(i+1)j}^{(3)})$
    end
    connect $(p_{(i_2)^{****}j}^{(2)}, p_{(-i_2)j}^{(3)})$
    if $j > j_2$ then
        connect $(p_{(i_2)j}^{(4)}, p_{(-i_2)(j-1)}^{(1)})$
    end
end
```

*: j_2 is the row number of the lowest cells related to HV winding in Figure 4.5.

**: j_3 is the row number of the highest cells related to HV winding in Figure 4.5.

***: $-i_2$ is the column number of the leftmost cells related to left part of HV winding which due to the symmetry has not been shown in Figure 4.5.

****: i_2 is the column number of the rightmost cells related to HV winding in Figure 4.5.

Algorithm 4.3. Electric connections for LV winding in IW model

```
for $j \leftarrow j_1^{*}$ to $j_4^{**}$ do
for $i \leftarrow (-i_1)^{***}$ to $(i_1^{****} - 1)$ do
    connect $(s_{ij}^{(2)}, s_{(i+1)j}^{(1)})$
    connect $(s_{ij}^{(4)}, s_{(i+1)j}^{(3)})$
end
connect $(s_{(i_1)^{****}j}^{(2)}, s_{(-i_1)j}^{(3)})$
if $j > j_1$ then
    connect $(s_{(i_1)j}^{(4)}, s_{(-i_1)(j-1)}^{(1)})$
end
```

*: j_1 is the row number of the lowest cells related to LV winding in Figure 4.5.

**: j_4 is the row number of the highest cells related to LV winding in Figure 4.5.

***: $-i_1$ is the column number of the leftmost cells related to left part of LV winding which due to the symmetry has not been shown in Figure 4.5.

****: i_1 is the column number of the rightmost cells related to LV winding in Figure 4.5.

4.2.3.2 Connection of IW model elements

The magnetic parts of the OW elements are connected in Algorithm 4.4 through nodes $n_{kj}^{(1)}$, $n_{kj}^{(2)}$, $n_{kj}^{(3)}$, and $n_{kj}^{(4)}$, which are associated with the magnetic component of the element in the k^{th} column and j^{th} row of the mesh illustrated in Figure 4.6.

Algorithm 4.4 Internal Magnetic Connections for OW elements

```
for $j^{*} \leftarrow 1$ to $N^{**}$ do
    for $k^{***} \leftarrow 1$ to $(P^{****})$ do
        if $j < N$ & $k < P$
            connect $(n_{kj}^{(2)}, n_{(k+1)j}^{(4)})$
            connect $(n_{kj}^{(3)}, n_{k(j+1)}^{(1)})$
        elseif $j = N$ & $k < P$
            connect $(n_{kj}^{(2)}, n_{(k+1)j}^{(4)})$
        elseif $j < N$ & $k = P$
            connect $(n_{kj}^{(3)}, n_{k(j+1)}^{(1)})$
        end
    End
end
```

*: j is the row number of the cell.	***: k is the column number of the cell.
**: N is the total number of rows in Figure 4.6.	****: M is total number of columns in Figure 4.6.

Algorithm 4.5 and Algorithm 4.6 are used to establish internal electrical connections between the parts of the OW mesh depicted in Figure 4.6. The connections between parts related to HV winding of the elements in Figure 4.6 is connected using the approach described in Algorithm 4.5. Nodes $p_{kj}^{(1)}$, $p_{kj}^{(2)}$, $p_{kj}^{(3)}$, and $p_{kj}^{(4)}$ shown in elements of Figure 4.8 are associated to the HV winding of the element in the k^{th} column and j^{th} row of Figure 4.6. The nodes $s_{kj}^{(1)}$, $s_{kj}^{(2)}$, $s_{kj}^{(3)}$, and $s_{kj}^{(4)}$ indicated in elements of Figure 4.8 that are related to the LV winding of those elements are connected using the approach described in Algorithm 4.6.

Algorithm 4.5 Electric connections for HV windings in OW model

```
for $j \leftarrow j_2^{*}$ to $j_3^{**}$ do
    for $k \leftarrow (-k_2)^{***}$ to $(k_2^{****} - 1)$ do
        connect $(p_{kj}^{(2)}, p_{(k+1)j}^{(1)})$
        connect $(p_{kj}^{(4)}, p_{(k+1)j}^{(3)})$
    end
    connect $(p_{(k_2)^{****}j}^{(2)}, p_{(-k_2)j}^{(3)})$
    if $j > j_2$ then
        connect $(p_{(k_2)j}^{(4)}, p_{(-k_2)(j-1)}^{(1)})$
    end
end
```

*: j_2 is the row number of the lowest cells related to HV winding in Figure 4.6.
**: j_3 is the row number of the highest cells related to HV winding in Figure 4.6.
***: $-k_2$ is the column number of the leftmost cells related to left part of HV winding which due to the symmetry has not been shown in Figure 4.6.
****: k_2 is the column number of the rightmost cells related to HV winding in Figure 4.6.

Algorithm 4.6 Electric connections for LV winding in OW model

```
for $j \leftarrow j_1^{*}$ to $j_4^{**}$ do
for $k \leftarrow (-k_1)^{***}$ to $(k_1^{****} - 1)$ do
    connect $(s_{kj}^{(2)}, s_{(k+1)j}^{(1)})$
    connect $(s_{kj}^{(4)}, s_{(k+1)j}^{(3)})$
end
connect $(s_{(k_1)^{****}j}^{(2)}, s_{(-k_1)j}^{(3)})$
if $j > j_1$ then
    connect $(s_{(k_1)j}^{(4)}, s_{(-k_1)(j-1)}^{(1)})$
end
```

*: j_1 is the row number of the lowest cells related to LV winding in Figure 4.6.
**: j_4 is the row number of the highest cells related to LV winding in Figure 4.6.
***: $-k_1$ is the column number of the leftmost cells related to left part of LV winding which due to the symmetry has not been shown in Figure 4.6.
****: k_1 is the column number of the rightmost cells related to LV winding in Figure 4.6.

4.2.3.3 Connection of IW model and OW model

Both IW and OW models should be connected to each other after their internal connections have been established. In the Double-2D approach, linearity in the conductors is assumed to be applicable. Because the two portions of the conductors that are being studied in each simulation are perpendicular to one another, the dotted product of the fields that are being generated by these portions is zero, and as a result, there is no interaction between the simulations. Thus, both portions of each winding are linearly connected. In fact, IW portion of HV winding and IW portion of LV winding have a linear relationship with OW portion of HV winding and OW portion of LV winding. Furthermore, the following relationships exist between the circuit parameters (voltages and currents) of the two portions of each winding.

$$I_{HV} = \mathrm{I}_{\mathrm{HV}}^{(\mathrm{IW})} = \mathrm{I}_{\mathrm{H}V}^{(\mathrm{OW})} \tag{4.11}$$

$$I_{LV} = \mathrm{I}_{L\mathrm{V}}^{(\mathrm{IW})} = \mathrm{I}_{L\mathrm{V}}^{(\mathrm{OW})} \tag{4.12}$$

$$V_{HV} = V_{HV}^{(IW)} + V_{HV}^{(OW)} \tag{4.13}$$

$$V_{LV} = V_{LV}^{(IW)} + V_{LV}^{(OW)} \tag{4.14}$$

where I_{HV}, $I_{HV}^{(IW)}$, and $I_{HV}^{(OW)}$denote currents passing through the HV winding and its IW and OW portions, respectively, while I_{LV}, $I_{LV}^{(IW)}$, and $I_{LV}^{(OW)}$denote currents passing through the LV winding and its IW and OW portions, respectively. And V_{HV}, $V_{HV}^{(IW)}$, and $V_{HV}^{(OW)}$ denote voltages across the HV winding and its IW and OW portions, respectively, whereas V_{LV}, $V_{LV}^{(IW)}$, and $V_{LV}^{(OW)}$ denote voltages across the LV winding and its IW and OW portions, respectively.

Based on the linear relationship between the simulations of two planes and the relations (4.11)-(4.14), it can be concluded that IW and OW models are connected to one another in such a way that their primary sides are connected in series, as well as their secondary sides, as seen in Figure 4.10. The HV winding parts of both models are connected by connecting nodes $p_{i_2 j_2}^{(4)}$ and $p_{(-k_2) j_3}^{(1)}$ which are related to the element placed in the i_2^{th} column and j_2^{th} row of the IW mesh illustrated in Figure 4.5, and the element placed in the $-k_2^{th}$ column and j_3^{th} row of the OW mesh, which due to symmetry only its symmetric element has been shown in Figure 4.6, respectively. The LV winding parts of both models are connected by connecting nodes $s_{i_1 j_1}^{(4)}$ and $s_{(-k_1) j_4}^{(1)}$ which are associated to the element in the i_1^{th} column and j_1^{th} row of the IW mesh shown in Figure 4.5, and the element in the $-k_1^{th}$ column and j_4^{th} row of the OW mesh, which is not displayed in Figure 4.6 due to symmetry. In the circuit shown in Figure 4.10, the HV side of the transformer is connected to a voltage source U_{in}, while the LV side is connected to a resistive load R_{load}. To connect the HV side of the modeled transformer to the voltage source U_{in}, the positive node of U_{in} is connected to the node $p^{(1)}_{-i_2 j_3}$, which is related to the element placed in the $(-i_2)^{th}$ column and j_3^{th} row of the IW mesh, and the negative node of U_{in} in is connected to the node $p^{(4)}_{k_2 j_2}$, which is related to the element placed in k_2^{th} column and j_2^{th} row of the OW mesh. To connect the LV side of the modeled transformer to R_{load}, the positive node of R_{load} is connected to the node $s^{(1)}_{-i_1 j_4}$, which is related to the element placed in the $(-i_1)^{th}$ column and j_4^{th} row of the IW mesh, and the negative node of R_{load} is connected to the node $s^{(4)}_{k_1 j_1}$, which is related to the element placed in k_1^{th} column and j_1^{th} row of the OW mesh.

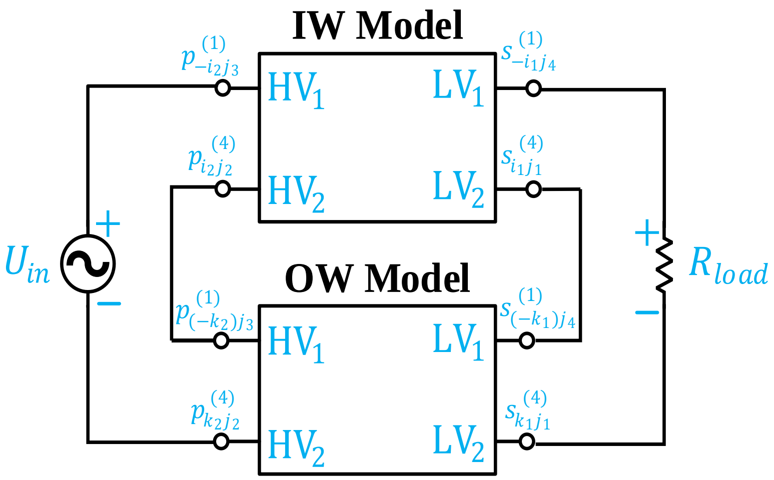

Figure 4.10 Diagram of double 2D model, electrical connections

4.3 Leakage inductance calculation by double-2D circuit-based method

As it was observed in Figure 4.1 and Figure 4.2, Single-2D circuit-based approaches are nearly accurate for representing open-circuit characteristics, but they are not accurate when it comes to short-circuit characteristics. Leakage inductances play important role in the behaviour of transformers under short-circuit conditions, this part explains how to derive leakage inductances using proposed double-2D approach.

The circuit shown in Figure 4.11, in which the HV side of the transformer is energized, and the secondary side is short circuited, is used to compute leakage inductance seen from the HV side of the transformer.

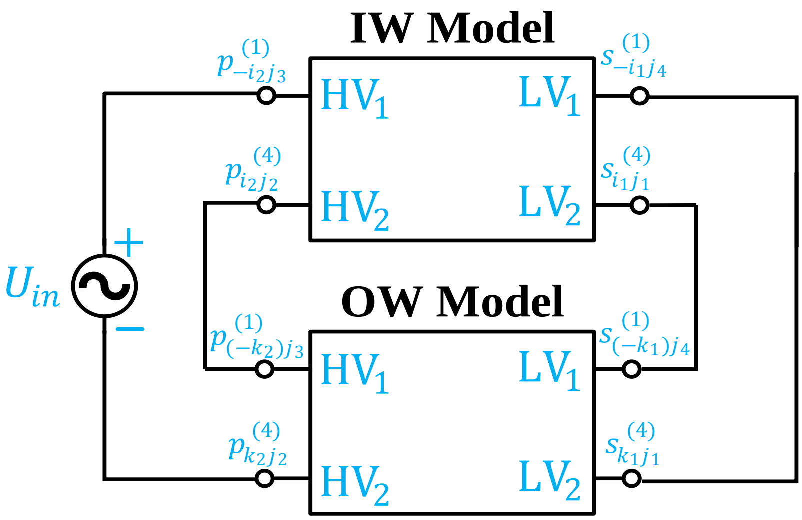

Figure 4.11 Diagram of double 2D model to calculate leakage inductance observed from HV side

4.3.1 Comparison of analytical and double-2D circuit-based models of transformer leakage inductance

4.3.1.1 General view

Numerical methods and analytical approaches can all be used to compute the transformer leakage inductance. Despite the fact that numerical methods such as the finite element method (FEM) are the most accurate ways for estimating leakage inductances, analytical approaches are preferred for calculating leakage inductances since numerical methods are complex and computationally expensive. There are a variety of analytical approaches for calculating leakage inductances, the majority of which are constrained to specified geometries and rely on simplifying assumptions, making them neither adaptive nor accurate enough for particular applications as we are going to describe hereafter.

Mostly, analytical approaches which are mostly considered as 2D methods have been utilised to compute leakage inductances, which are typically done in two steps: first, the leakage inductance per unit length is computed in a 2D transformer cross section, and then the result is scaled by the mean length of the turn. Recently, various attempts have been made in the literature [81-85] to enhance analytical approaches for accounting for 3d effects when calculating leakage inductance. To accomplish this, a technique known as Double-2D [81-85] was employed, in which two cross sections, one inside the transformer window (IW) and the other outside the transformer window (OW), were used in the calculations.

4.3.1.2 Definition of problem of calculating leakage inductances by analytical methods

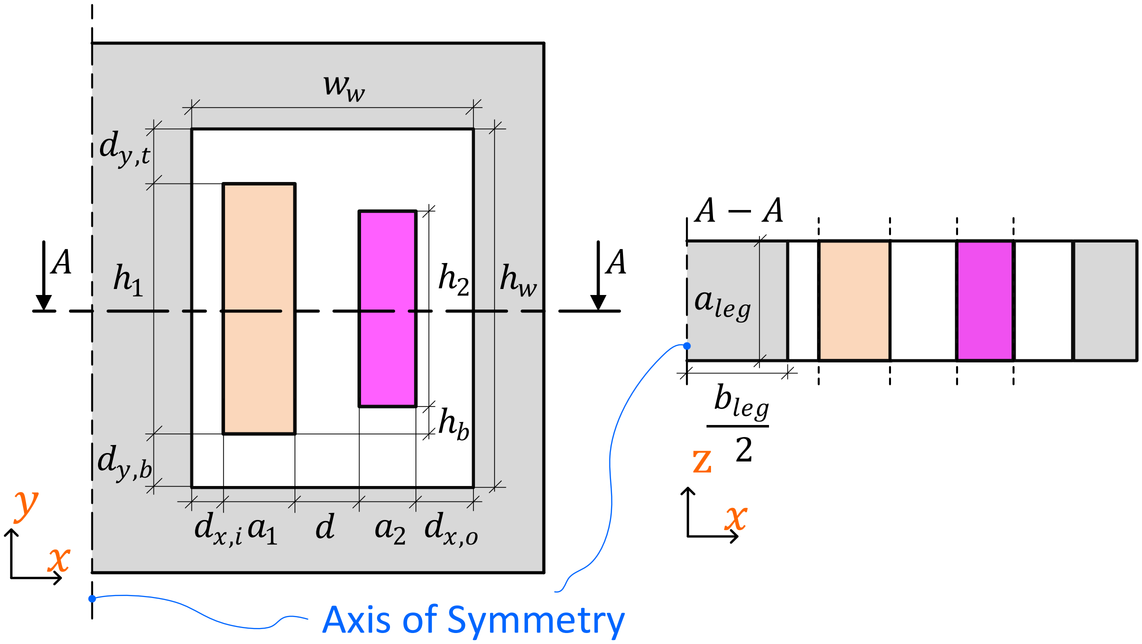

Figure 4.12 Definition of geometrical parameters of single-phase transformer [78]

To begin, the analytical methods for calculating leakage inductance for inside-window cross-sections are described, as well as their assumptions and restrictions. Figure 4.12 shows a representation of a transformer for which leakage inductances will been estimated using various approaches. To measure the leakage inductance between two windings, magnetomotive forces of equal magnitude but opposing direction must be applied to each. There will be no flux linking the two windings in this case; instead, just leaking flux will exist. In practice, this is accomplished by energizing one transformer winding while short-circuiting the other. To compute leakage inductance from geometrical data, the resulting magnetic field $\vec{B}$ during short-circuit must be computed. The magnetic field outside the core during short-circuit is given by

$$\vec{\nabla} \times \vec{B} = \mu_0 \vec{J} \tag{4.15}$$

where μ_0 is the permeability of vacuum. Because $\vec{B}$ is a solenoidal vector field, it can be represented as the curl of another vector field $\vec{B} = \vec{\nabla} \times \vec{A}$, which $\vec{A}$ is magnetic vector potential. Using Coulomb gauge, (4.15) is transformed into a new relationship known as Poisson's equation

$$\vec{\nabla}^{2} \vec{A} = -\mu_0 \vec{J} \tag{4.16}$$

Because short-circuits are low-frequency transients, the current density J can be considered to be uniform throughout each winding's cross-section. Furthermore, each winding is treated as if it were solid, with only one equivalent turn, and the current density J is calculated by

$$I = \iint_S \vec{J} \,.\, d\vec{s} = JS, \tag{4.17}$$

where S is the cross-sectional area of the conducting surface.

The magnetomotive forces of two windings in a transformer short-circuit are almost equal in size and opposite in direction, meaning that the magnetomotive force required to magnetise the core is negligible. In other words, the permeability of the core may be assumed to be infinite. The tangential component of flux and the normal component of the magnetic vector potential are both zero when the permeability of the core is infinite. As a result, the homogeneous Neumann boundary condition is applied to solve the problem.

$$\frac{\partial A_z}{\partial \vec{n}} = 0 \text{ on } \Lambda \tag{4.18}$$

where $\vec{n}$ is the normal vector of the boundary Λ.

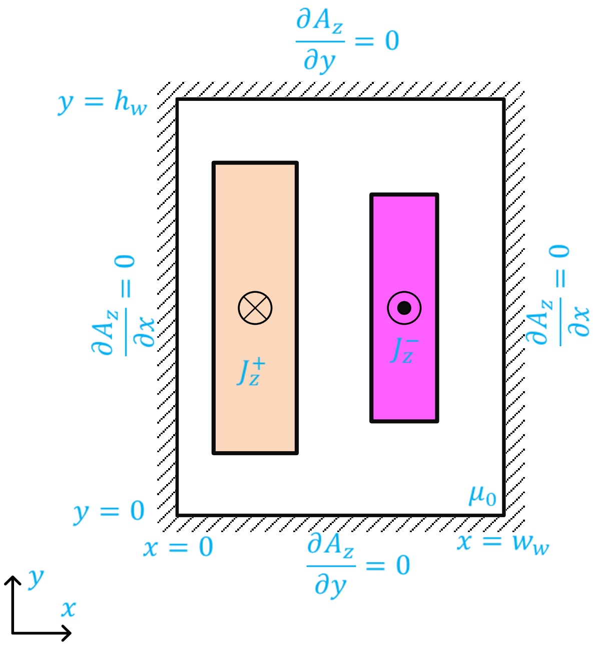

Figure 4.13 Definition of geometrical parameters of single-phase transformer

When all of the aforementioned considerations are taken into account, the problem becomes the one presented in Figure 4.13. The HV and LV coils carry positive and negative currents in the z direction, with densities of J_z^+ and J_z^-, respectively. Also, the magnetic vector potential will be in the z direction, due to the uniform permeability in the transformer window. The analytical approaches are aimed at determining the magnetic vector potential which is then used to determine the magnetic energy per length according to inductances.

$$W'_{mag} = \frac{1}{2}\iint_A A_z . J_z dA \tag{4.19}$$

After that, using the computed magnetic energy, the leakage inductance per unit length is calculated according to

$$L'_{in} = \frac{2W'_{mag}}{I^2} \tag{4.20}$$

4.3.1.3 One-dimensional methods

The classical approaches are one-dimensional approaches, meaning they assume that leakage flux is only a function of one space coordinate and not a function of the second for example in Figure

4.12, it is only supposed that leakage flux is a function of x coordinate and does not depend on the y coordinate. The most well-known classical formula for calculating leakage inductance, derived from a one-dimensional assumption known as Kapp [86], is

$$L_{Kapp} = \mu_0 N^2 \left(d + \frac{a_1 + a_2}{3}\right)\frac{1}{h} \tag{4.21}$$

where L_{Kapp} is the leakage inductances per unit length. a_1, a_2, and d represent the widths of the primary winding, secondary winding, and gap between them. h represents the average height of the primary and secondary windings ($h = (h_1 + h_2)/2$), and N represents the number of excited windings. One-dimensional approaches ignore fringing effects and are only used when the distance between the windings and the yokes is small, and the heights of both windings are equal.

4.3.1.4 Two-dimensional methods

Two-dimensional approaches, which consider the leakage flux functions of two space coordinates x and y, are the more accurate ways to calculate leakage inductances.

The Rogowski approach [87] is the most widely used 2D method, and it yields an equation that is similar to Kapp's equation (4.21), but with an additional correction factor K to account for fringing effects at the top and bottom of the windings.

$$L_{\text{Rogowski}} = K L_{Kapp} \tag{4.22}$$

$$K = 1 - \frac{1 - e^{-kh}}{kh}\left[1 - \frac{1}{2} e^{-2kd_{y,b}\left(1 - e^{-kh}\right)} \times \left(1 + e^{-k\left(d_{y,t} - d_{y,b}\right)} - e^{-k\left(2d_{y,b} + 2d_{y,t} + h\right)}\right)\right] \tag{4.23}$$

$$k = \frac{\pi}{a_1 + d + a_2}$$

where $d_{y,b}$ and $d_{y,t}$ are the heights of the gaps between the primary winding and the upper yoke and lower yoke, as depicted in Figure 4.12, and all other parameters are those defined in (4.21). Even though this method is more accurate than Kapp method, this method is only applicable in cases in which the windings are of equal height and there are no gaps between the windings and the legs, as well as cases in which the distance between the windings is constant and the windings are of constant width.

Roth [88, 89] proposed a 2D method for calculating leakage inductance, in which the current density of each single winding is expressed using a double Fourier series function. The method is known as double space harmonics because the double Fourier series is dependent on both the x and y coordinates. The magnetic vector potential for each winding $A_{z,k}(x,y)$ is then determined using Poisson's equation as a double Fourier series function, which can then be summed for all windings (is the total number of windings has been denoted by N) to yield the total magnetic vector potential $A_z(x,y)$.

$$A_z(x,y) = \sum_{k=1}^{N} A_{z,k}(x,y) \tag{4.24}$$

Although this approach, unlike the Rogowski method, can be used for windings of different heights and has no spatial limits, it is assumed that the permeability of the core is infinite $\mu_{r,c} = \infty$. In fact, Roth's method can’t solve problems involving regions that are confined by materials having finite permeability.

Margueron [72, 73] proposed and developed a more accurate approach that works by superposing magnetic potentials from single windings. To impose the boundary conditions, this method uses the method of images to mirror the windings one by one. This is the only analytical method that takes into account the finite permeability of the core. Figure 4.14 shows how the method of images is applied to the IW cross section of the window shown in Figure 4.13. Four image layers result in an infinite number of image windings; however, only a limited number of layers are considered, with their numbers set by the required accuracy and computation time constraints. To account for the permeability of the plane, the current carried by the image conductor in each layer is multiplied by k^n, where k is the image coefficient, which is equal to $\frac{\mu_{r,c}-1}{\mu_{r,c}+1}$, and n denotes the image layer number. The effect of the core in estimating leakage inductance becomes crucial when the permeability of the core is low.

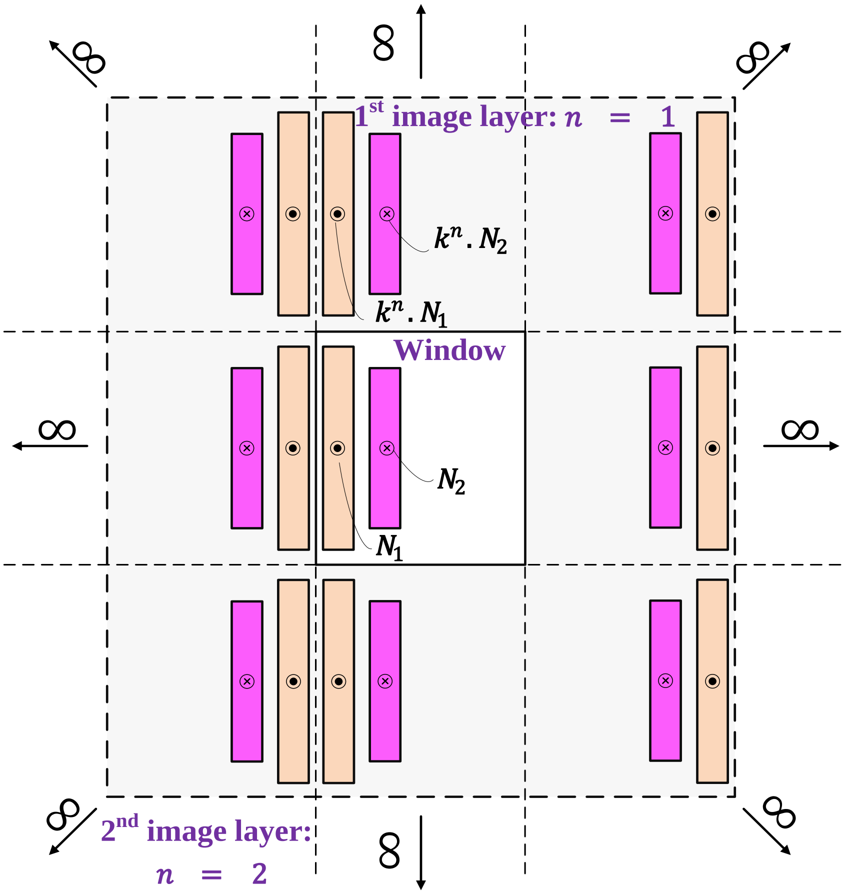

Figure 4.14 Transformer window with two winding layers: the original and an image one

4.3.1.5 Single-2D and double-2D analytical models

The leakage inductance per unit length of IW cross section L'_{in} obtained by analytical methods is multiplied by the mean turn length MTL to obtain the total leakage inductance using the traditional Single-2D model according to

$$L_{Singlw-2D} = L'_{in}. MTL \tag{4.25}$$

However, the traditional Single-2D model for calculating leakage inductances is not accurate since it applies the axisymmetric assumption to the EE cores which is not correct for this type of cores. As a result, Double-2D approaches have been proven to be more accurate in the literature, in which the transformer is investigated in two cross-sections: IW and OW. Until far, the weaknesses and strengths of analytical methods were only reviewed for IW cross sections. In the following, it will be determined whether each analytical approach can determine leakage inductances of OW cross sections, and for those that do, the assumptions used will be addressed. To begin with, leakage inductances for OW sections cannot be calculated using Kapp's, Dowell's, or Rogowski's models. Roth's model and Margueron's model may all be used to compute the leakage inductance for OW cross sections. However, because of the various simplifying assumptions and geometrical restrictions, they are not applicable in all cases.

Roth's method is fundamentally applied to an IW cross section. To apply Roth's approach to OW cross sections, an IW cross section is utilized, with the yokes and outer leg placed far enough away from the windings. To meet this condition, the distances $d_{y,b}$, $d_{y,t}$, and $d_{x,o}$ in the IW cross section illustrated in Figure 4.12 can all be set to $10 \times \frac{h_w+w_w}{2}$. However, for the OW cross section, like for the IW cross section, the magnetic permeability of the core is assumed to be infinite [78].

Despite the fact that Margueron's model can account for the core's finite permeability, it makes simplifying assumptions in order to give ideal boundary conditions for mirroring. In fact, the OW cross section depicts two current carrying windings next to a ferromagnetic material having finite height and thickness, as illustrated in Figure 4.15(a). This constellation isn't well suited the method of images. To make the method of images work, the thickness and height of the ferromagnetic material be assumed to be infinite as shown in Figure 4.15(b). and Figure 4.15(c) shows a mathematical representation of this ideal mirror constellation. When the relative permeability value of the core is greater than 100, Margueron et al. determined that the thickness of the core can be neglected [78]. Also, in [78], for a restricted number of transformer cases, it has been proven that treating the height of the ferromagnetic material as infinite has small effect on the value of leakage inductance.

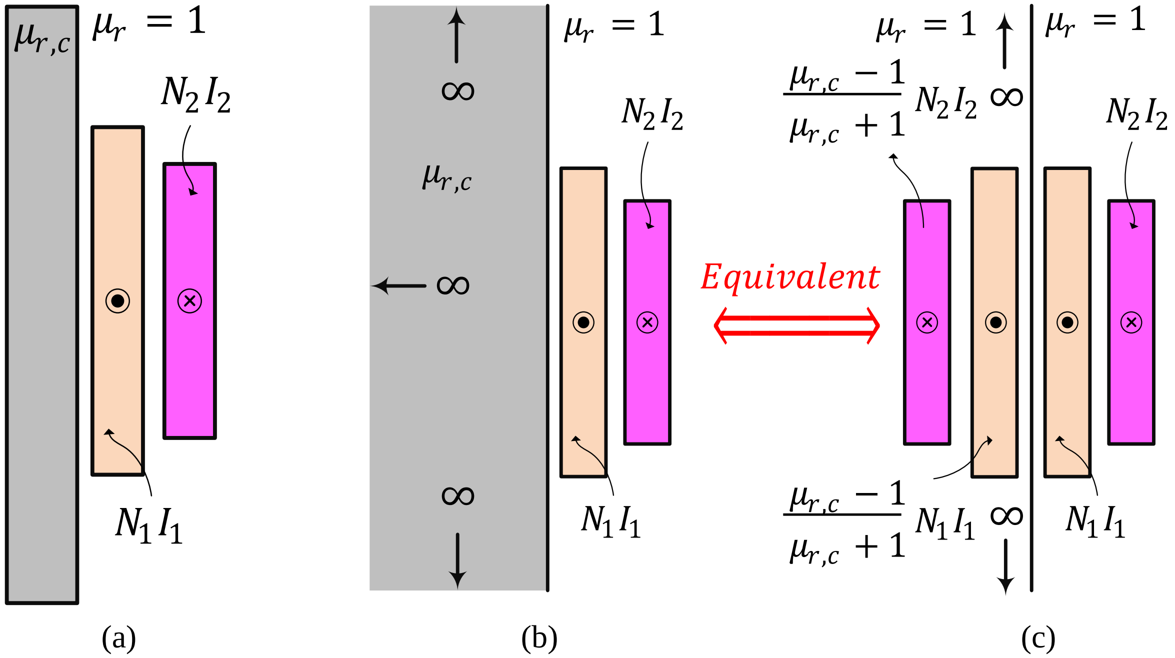

Figure 4.15 The method of image applied to the OW cross section. (a) Actual OW cross-section that isn't suited the method of images. (b) Assumed OW cross-section that is suited the method of images. (c) Mathematical equivalent of (b) using the method of images

In the existing analytical approaches to calculate leakage inductance using Double-2D approach, first, for both cross sections, the leakage inductances are calculated per unit length, which are indicated by L'_{in} for IW cross sections and L'_{out} for OW cross sections. Then, the per-unit length values are multiplied by the corresponding partial winding lengths, which are represented as MTL_{in} for IW cross sections and MTL_{out} for OW cross sections, and the total leakage inductance is obtained by

$$L_{Double-2D} = L'_{in}.MTL_{in} + L'_{out}.MTL_{out} \tag{4.26}$$

MTL_{in} and MTL_{out} are portions of the perimeter of a hypothetical rectangle with sides in the middle of the air gap between two windings, as shown in Figure 4.9, and are given by the following equation, which was proposed in [78] and is based on the parameters defined in Figure 4.12.

$$MTL_{in} = 2a_{leg} \tag{4.27}$$

$$MTL_{out} = 2b_{leg} + 4\left(d_{x,i} + a_1 + d + a_2\right) \tag{4.28}$$

4.3.1.6 Double-2D circuit-based method vs Double-2D analytical methods

Because the models must first be created in EMT-type software, the Double-2D circuit-based method proposed in this chapter is slower than analytical methods for calculating leakage inductance, and thus it cannot be used for design applications requiring a high number of computations. However, in some transient studies where accurate determination of leakage inductance of transformer is important it can be used. This part compares the accuracy of the Double-2D circuit-based approach proposed in this chapter to the accuracy of Double-2D analytic-based approaches (Roth and Margueron) and 3D-FEM. The measurement results, as well as the Double-2D Roth and Double-2D Margueron results, and the 3D-FEM results, are taken from [78]. Table 4.1 shows the results of the comparisons for three transformers which their geometrical parameters are listed in Table 4.2.

Table 4.1 Comparison of the accuracy of the proposed model to that of analytical and FEM models

	L_σ	**Relative Error**			
Tr.	**Measurement**	**Margueron Double-2D**	**Roth Double-2D**	**3D-FEM**	**Circuit-based Double-2D**
No. 1	27 μH	11.3%	10.4%	2.3%	2.2%
No. 2	10.7 μH	6.6%	5.53%	-2.7%	3.5%
No. 3	13.4 μH	15%	10.61%	3.3%	7.2%
nRMSE	Ref.	11.5%	9.1%	2.8%	4.8%

Table 4.2 Parameters of considered transformers, see Figure 4.13 for parameter definitions [78]

	Transformer geometry parameters (mm)												Turns	
	a_1	a_2	d	h_1	h_2	h_b	$d_{y,b}$	$d_{y,t}$	$d_{x,i}$	$d_{x,o}$	b_{leg}	a_{leg}	N_1	N_2
No. 1	4.9	4.9	17.5	90	80.0	5.0	3.0	0.0	0.0	7.0	56.0	30.0	20	20
No. 2	4.2	4.6	4.0	52.0	44.0	4.0	1.9	0.0	0.0	8.5	26.0	28.1	23	26
No. 3	4.2	4.6	4.0	52.0	44.0	4.0	1.9	0.0	0.0	8.5	26.0	28.1	23	26

As it can be observed in Table 4.1, the Double-2D circuit-based method proposed in this chapter is more accurate than two Doubel-2D analytical methods (Roth and Margueron). In simulation applications, an inaccuracy of less than 5% derived by Double-2D method is considered acceptable.

The improved accuracy seen with Double-2D circuit-based approach compared to Double-2D analytical methods can be attributed to three key factors. First, although analytical methods are nearly as accurate as 2D FEM in calculating leakage inductances per length on IW or OW cross sections, they are less accurate in calculating total leakage inductances using Double-2D models than 3D FEM since their estimates for determining MTLs are rough. However, in the proposed Double-2D circuit-based method, determining the depth of the flux tube, which is comparable to the MTL for that mesh, is more accurate and dependent on the mesh's position. Second, it was previously said that the Margueron approach is the only analytical method that can account for the effect of core permeability; nevertheless, this method can also account for the effect of core permeability. Also, the Margueron method can only account for the core's effect with linear relative permeability, but our method can account for the core's effect with both linear and nonlinear relative permeability. As a result, this method is superior to all analytical methods in accounting the effect of the core. This ability is useful when the permeability of the core is low, as previously stated. In addition, various geometrical assumptions are made in analytical approaches to calculate the transformer's leakage inductance. For example, as illustrated in Figure 4.15, the Margueron approach makes an assumption about the OW cross-section to make it suitable for the method of images. The Double-2D circuit-based technique, on the other hand, requires no geometrical assumptions. For example, in contrast to the Margueron technique, Double-2D circuit-based models can accurately represent OW cross-section without any assumed change in the geometry. Also, for transformers with more than two windings (multi-winding or three-phase transformers) the proposed method has a significant advantage over analytical methods. Analytical approaches for these types of transformers can only offer an inductance matrix representation referred to each winding couple, which is not geometrically valid, especially when there are more than three windings. For these types of transformers, however, the Double-2D circuit-based models can simultaneously see the effects of all windings as well as the effect of the core, resulting in a more geometrically and physically meaningful representation.

4.4 Double-2D circuit-based model for three phase transformers

4.4.1 Division of 3D structure into 2D sections

In this section, proposed Double-2D circuit-based method is used to model three phase transformers. In order to account for 3D field effects of three-phase transformers, the circuit-based method derived from Hopkinson Analogy is utilised to solve four 2D problems (Double-2D). This method divides the 3D structure of the transformer into four 2D substructures, each with its own magnetic field distributed across a unique plane that can be studied using 2D circuit-based models.

Figure 4.16 depicts four cross sections of these four 2D substructures: an inside transformer window (IW), an outside window (OW) of phase U, an outside window (OW) of phase V, and an outside window (OW) of phase W. The field distribution in the part of the structure depicted on Figure 4.16(a) is primarily stored in the core. However, the field distributions in the parts of the structure depicted on Figure 4.16(b)-(d) are mostly stored in the air. It's also worth noting that the models of planes shown in Figure 4.16(a)-(d) have no interactions with each other because, first, the magnetic field distributions in three planes related to the OW of three phases ((b)-(d)) don't cross each other, and second, even though the magnetic field distribution in plane related to IW ((a)) crosses the magnetic field distributions related to the OW cross sections of three phases ((b)-(d)), it's perpendicular to them, and thus the dotted product between their field distributions is zero.

After that the 3D structure is divided into four 2D substructures, each of which is subdivided into meshes similar to the mesh model shown in Figure 4.5 for IW substructures and similar to the mesh model shown in Figure 4.6 for OW substructures. After that, for elements of the IW mesh, equivalent circuits similar to the circuit types shown in Figure 4.7 are built, and the equivalent circuits similar to the circuit types shown in Figure 4.8 are built for elements of the three OW meshes. The techniques for finding the parameters of equivalent circuits of elements are the same as those given in section 4.2.2.

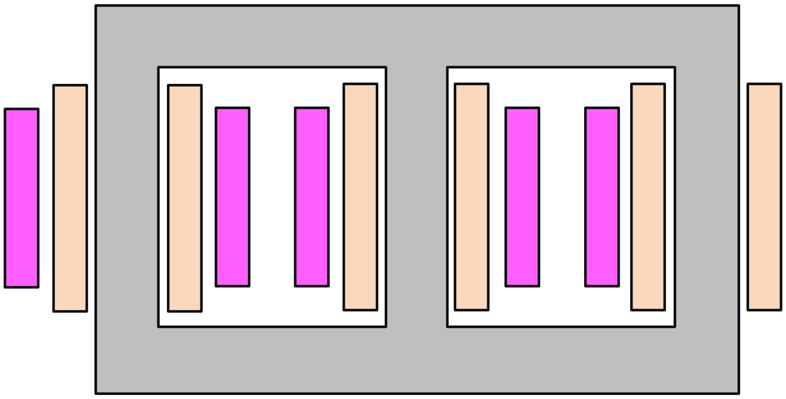

IW Model
(a)

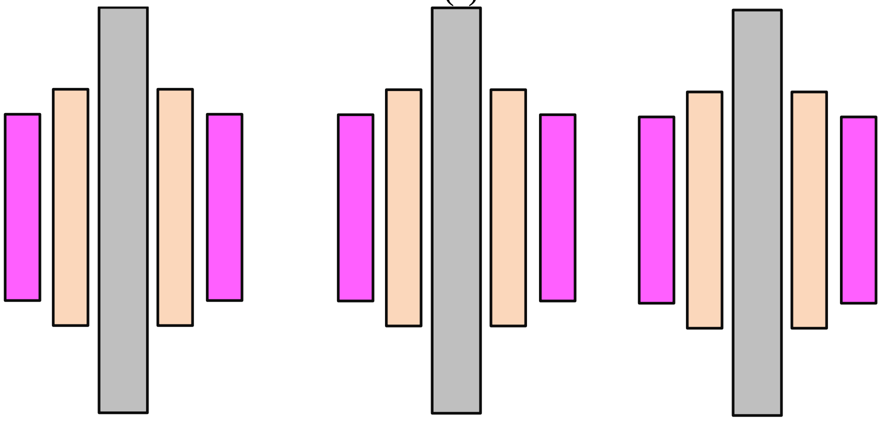

OW Model of Phase U (b)　**OW Model of Phase V** (c)　**OW Model of Phase W** (d)

Figure 4.16 Division of a three-phase three-legged transformer into four 2D sections

4.4.2 Connection of 2D models

The procedures for internally connecting the elements of each cross-section model are similar to those detailed in section 3.2.3. Then to connect the IW model to the OW models, the HV sides of the IW and OW models are connected in series with each other, and their LV sides are likewise connected in series. In fact, as shown in Figure 4.17, the HV sides of phases U, V, and W from the IW model are connected in series to the HV sides of the OW models of phases U, V, and W, respectively, and the LV sides of phases U, V, and W from the IW model are connected in series to the LV sides of the OW models of phases U, V, and W, respectively. The external connections between the transformer nodes are then constructed depending on the transformer windings arrangement, which for the transformer depicted in Figure 4.17 is star delta.

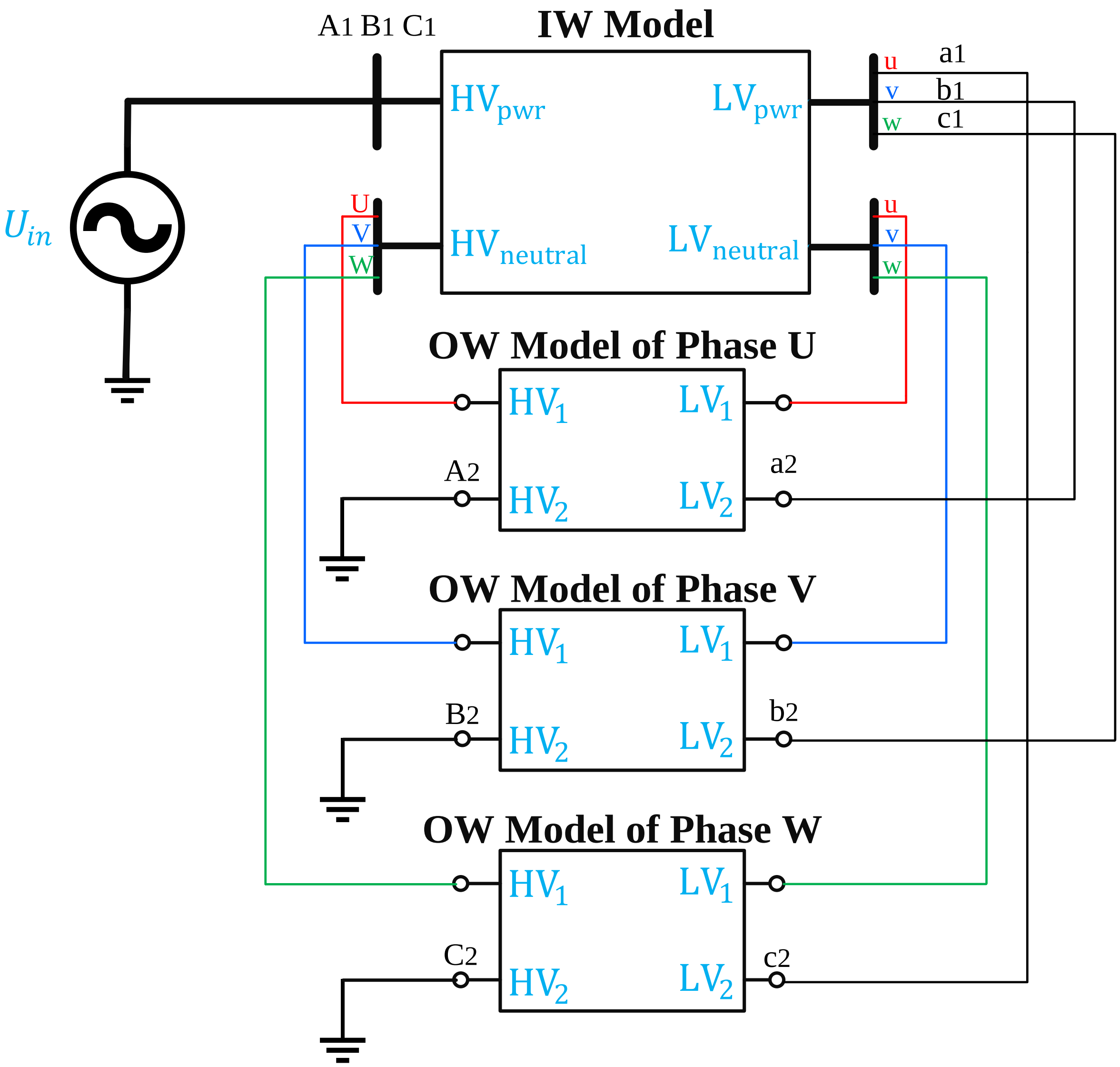

Figure 4.17 Diagram of double 2D model for three phase transformer with star-delta connection

4.4.3 Validation

In this section, the open-circuit and short-circuit results that were acquired using the Single-2D circuit-based approach, 2D-FEM, and 3D-FEM in section 4.1.1 are derived using the Double-2D circuit-based technique. To accomplish this, the circuits illustrated in Figure 3.18 and Figure 3.23 are implemented by double-2D circuit-based method in EMTP, resulting in the new open-circuit and short-circuit curves shown in Figure 4.18 and Figure 4.19, respectively. The open-circuit results for Single-2D circuit-based, FEM 2D, Double-2D circuit-based, and FEM 3D are substantially similar, especially when the transformer does not go into deep saturation, as shown in Figure 4.18. Because the magnetic flux under open-circuit conditions largely passes through the core and can be substantially covered in 2D models, there is no need for a 3D representation of the transformer. However, in comparison to 2D FEM and Single-2D circuit-based methods, the Double-2D circuit-based method produces less error under highly saturated operating conditions. The reason for this is the ability of the Double-2D circuit-based technique to more accurately represent fluxes leaking into the air under these operating conditions. As previously stated, going from a single-2D model to a double-2D model was motivated by the fact that single-2D models were inaccurate in representing transformer behaviour under short-circuit conditions. Leakage inductances, it was also mentioned, have a significant impact on transformer behaviour under short-circuit conditions. Table 4.1 showed that for estimating leakage inductances for a single-phase transformer, the Double-2D technique has an acceptable error of less than 5%. Here, Figure 4.19 shows how the Double-2D circuit-based method accurately represents the 3D effects of magnetic fields for a three-phase transformer in short-circuit. Finally, accuracy values for Hopkinson Single-2D, FEM 2D, and Hopkinson Double-2D methods are calculated by applying nRMSE to curves shown in Figure 4.18 and Figure 4.19, and using 3D FEM results as the reference values.

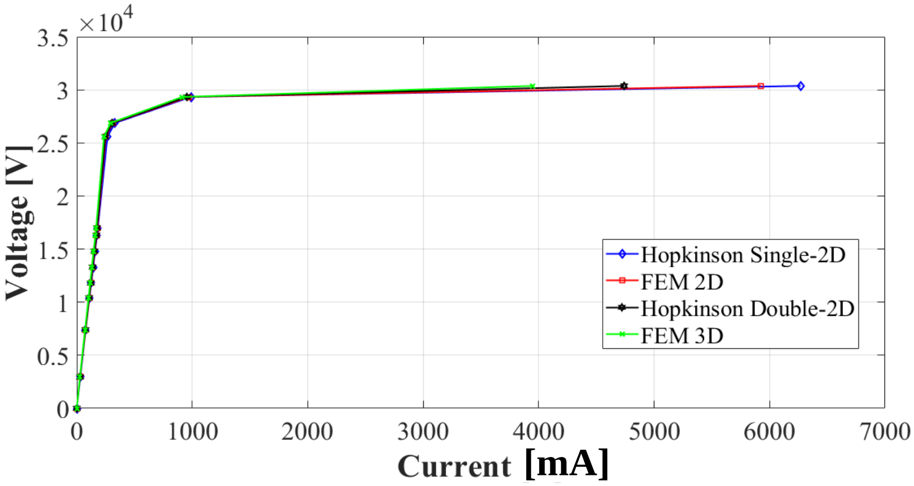

Figure 4.18 V-I characteristic for open-circuit achieved by Hopkinson Single-2D model, FEM 2D, Hopkinson Double-2D model, and FEM 3D

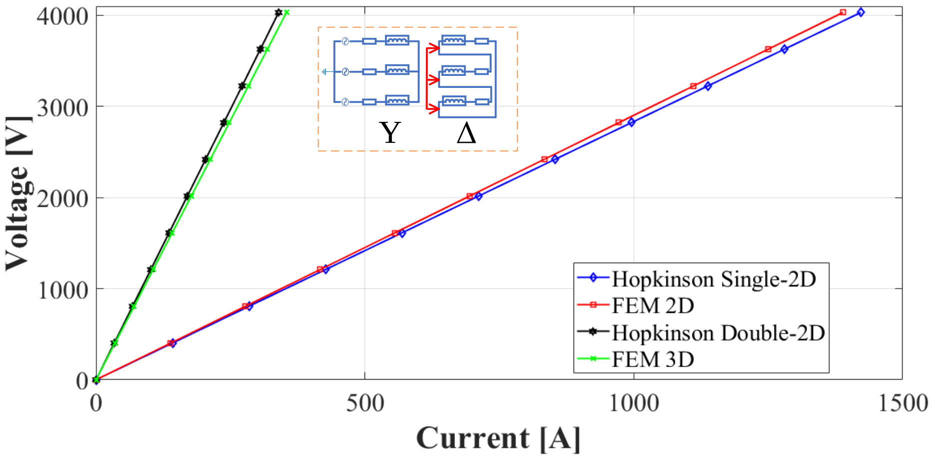

Figure 4.19 V-I characteristic while short-circuiting the secondary side achieved by Hopkinson Single-2D model, FEM 2D, Hopkinson Double-2D model, and FEM 3D

Table 4.3 Error derived by Hopkinson Single-2D, FEM 2D, and Hopkinson Double-2D for open-circuit and short-circuit conditions

Model	Operation-condition	Hopkinson Single-2D	FEM 2D	Hopkinson Double-2D
nRMSE (%)	Open-circuit	7.40	6.39	4.50
	Short-circuit	301.69	292.31	4.06

4.5 Conclusion

This chapter improved the proposed distributed circuit-based methods to account for the 3D effects of magnetic fields in transformers. To begin, the limits of single-2D methods for modelling 3D effects of magnetic fields are discussed, as well as why moving from 2D to quasi-3D models is so important. Following that, the history of Double-2D FEM is explained. The concept of the proposed Double-2D circuit-based method is then discussed, as well as how to implement it for a simple single-phase transformer with two windings. The ability of the proposed Double-2D method to accurately compute leakage inductances is also highlighted. The proposed method is compared to existing analytical methods for computing leakage inductances. The limitations and assumptions of existing analytical approaches are reviewed, and it is explained how the suggested method resolves them. Finally, the proposed Double-2D circuit-based technique is implemented for a three-phase transformer, and its high accuracy in representing 3D effects of magnetic fields is demonstrated by comparing the findings to 3D FEM.

CHAPTER 5 CONCLUSION

5.1 Summary

The main focus of this research was the electromagnetic modeling of magnetic devices including inductors and transformers in EMT-type software by circuit-based methods. Indeed, this thesis provided a distributed model of magnetic devices using circuit-based methods. This approach made use of meshing in such a way that space was discretized into electric and magnetic circuits. This thesis attempted to bridge the gap between circuit-based approaches and finite element modelling. Proposed models in this thesis similar to FEM could provide a complete geometrical description of magnetic flux paths, including leakage and fringing flux paths, in addition to modelling non-homogeneous materials and magnetic saturation. Additionally, the thesis intended to provide models that may be implemented in the EMT-type software using currently available components. To do this, distributed models were created using three rules that are commonly used to link magnetic and electric circuits: the Hopkinson analogy, the Buntenbach analogy, and the duality principle.

In Chapter 2, three distributed circuit-based approaches (HBD-circuits) for accurately modelling inductors in EMT-type software were proposed. Many significant features of the FEM could be provided by the proposed models, including detailed geometrical representation and incorporation of magnetic saturation. Both in terms of accuracy and computation time, HBD-circuits were compared to one another as well as to the 2D FEM. High levels of accuracy were reached in depicting both the external and internal behaviours of inductors using HBD-circuits. HBD-circuits also demonstrated excellent computational performance in such a way that, even when the number of elements is enormous, HBD-circuits surpass FEM in terms of computational speed. Additionally, it was proved that HBD-circuits are just as accurate as FEM models in capturing the correct behaviour of inductors in a circuit during the occurrence of electromagnetic transient phenomena. Ferroresonance, a nonlinear phenomenon in power systems, was studied to demonstrate the HBD-circuits' ability to represent electromagnetic transient events. In this example, the inductor was modelled using HBD-circuits, and the results were compared to those obtained using FEM, with a good agreement found between the two.

Chapter 3 improved the HBD-circuits to model transformers, which are key components of the power system. This chapter presented each step of the process of creating HBD-circuits for transformers in EMTP, including meshing, deriving equivalent circuits for individual elements, connecting elements to establish the final model, and deriving and assigning values to the equivalent circuit parameters. Additionally, this chapter discussed how to model transformer internal faults using HBD-circuits. To do this, a faulty winding was divided into distinct sections according to the type of fault and each section was regarded as a distinct winding. Additionally, it was demonstrated how new element types are established, their values are determined, and how they are connected to one another. Finally, when compared to 2D FEM results, it was shown that HBD-circuits accurately describe the internal behaviour of transformers as well as the behaviour observed at their terminals. The behaviours of the transformer during open-circuit and short-circuit as steady state phenomena and energization as a transient phenomenon were accurately reproduced using HBD-circuits. Additionally, it was demonstrated that HBD-circuits can accurately model internal faults in transformers and, in comparison to other analytical methods and lumped parameter models, they could not only represent leakage inductances, which are necessary for modelling internal faults, but also the effect of the core on internal fault modelling.

As illustrated in Chapter 4, the distributed circuit-based approaches established in the preceding chapters can be improved to account for the three-dimensional effects of magnetic fields in transformers through the use of a technique called Double-2D. It was demonstrated that Double-2D circuit-based approaches are significantly accurate in modeling leakage inductances, even more so than analytical methods, and are very near to the 3D FEM. Additionally, it was proved that the Double-2D approach can reproduce the results of 3D FEM for a three-phase transformer under open- and short-circuit conditions.

As a final summary, the methods proposed in this thesis can be used to equip EMT-type software tools with certain features of 2D and 3D FEM modelling, such as accurate geometry modelling, consideration of iron core saturation, and consideration of all magnetic flux paths, including leakage flux paths through the air during saturated operating conditions.

5.2 Future works

On the few opportunities to continue and improve on this work, first, other features, such as iron losses and capacitive effects, can be incorporated to the proposed distributed models to enhance their application potential.

Second, because the meshing approach used in this paper was not intelligent, the meshing procedure can be adjusted to ensure that the mesh sizes are selected intelligently.

Third, these new methodologies are applied to real electromagnetic transient cases seen in power networks in order to gain a better understanding of their capabilities in power system analysis.

Fourth, the ability of the Double-2D approach provided in Chapter 4 to accurately characterize leakage flux paths can be used to estimate air-core leakage inductances for the transformer while accounting for the tank effect.

Fifth, while this thesis focuses on low and mid-frequency transients, it may be worthwhile to propose new distributed circuit-based models for high-frequency transients.

Sixth, thermal equivalent circuits based on basic electrical-thermal analogous equations can be derived in distributed form and coupled with the magnetic-electric circuit-based models proposed in this thesis to predict temperature distribution and localise hot spot temperatures in magnetic devices.

REFERENCES

[1] J. Hopkinson, "Magnetisation of iron," *Phil. Trans. Roy. Soc. London,* vol. 176, pp. 455-469, 1885.

[2] J. Hopkinson and E. Hopkinson, "Dynamo - electric machinery," *Phil. Trans. Roy. Soc. London,* vol. 177, pp. 331-358, 1886.

[3] R. W. Buntenbach, "Improved circuit models for inductors wound on dissipative magnetic cores," in *Proc. 2nd Asilomar Conf. Circuits Syst.*, Pacific Grove, GA, USA, 1968, pp. 229–236.

[4] W. Cauer, "Topologische Dualitätssätze und Reziprozitätstheoreme der Schaltungtheorie," *Zeitschrift für Angewandte Mathematik und Mechanik,* vol. 14, pp. 349-350, 1934.

[5] E. C. Cherry, "The Duality between Interlinked Electric and Magnetic Circuits and the Formation of Transformer Equivalent Circuits," in *Proceedings of the Physical Society. Section B*, 1949, vol. 62, no. 2, pp. 101-111.

[6] H. Sire and d. Vilar, "La Dualité en électrotechnique," *L'éclairage électrique*, vol. XXVII, pp. 252–259, 1901.

[7] A. Russell, *A Treatise on the Theory of Alternating Currents*. Cambridge, U.K.: Cambridge University Press, 1914.

[8] G. Kron, "Steady-State Equivalent Circuits of Synchronous and Induction Machines," *Transactions of the American Institute of Electrical Engineers*, vol. 67, no. 1, pp. 175-181, 1948.

[9] A. Magdziarz and Z. Zagan, "Mathematical simulation model of power transformer for electrical power system protective schemes," in *System Modelling and Optimization*: Springer, 1986, pp. 567-576.

[10] M. Lambert, "Transformer modeling for low- and mid-frequency electromagnetic transients simulation," Ph.D. Thesis, 2014.

[11] M. Lambert, J. Mahseredjian, M. Martı´nez-Duró, and F. Sirois, "Magnetic Circuits Within Electric Circuits: Critical Review of Existing Methods and New Mutator Implementations," *IEEE Transactions on Power Delivery,* vol. 30, no. 6, pp. 2427-2434, 2015.

[12] C. J. Carpenter, "Magnetic equivalent circuits," *Proceedings of the Institution of Electrical Engineers,* vol. 115, no. 10, pp. 1503-1511

[13] E. R. Lwithwaite, "Magnetic equivalent circuits for electrical machines," *Proceedings of the Institution of Electrical Engineers*, vol. 114, no. 11, pp. 1805-1809

[14] B. D. H. Tellegen, "The gyrator, a new electric network element," *Philips Res. Rep,* vol. 3, no. 2, pp. 81-101, Apr. 1948 1948.

[15] L. O. Chua, "Synthesis of new nonlinear network elements," *Proceedings of the IEEE*, vol. 56, no. 8, pp. 1325-1340, 1968.

[16] L. Chua, "Memristor-The missing circuit element," *IEEE Transactions on Circuit Theory,* vol. 18, no. 5, pp. 507-519, 1971.

[17] M. Young, A. Dimitrovski, Z. Li, and Y. Liu, "Gyrator-Capacitor Approach to Modeling a Continuously Variable Series Reactor," *IEEE Transactions on Power Delivery*, vol. 31, no. 3, pp. 1223-1232, 2016.

[18] M. Luo, D. Dujic, and J. Allmeling, "Leakage Flux Modeling of Multiwinding Transformers for System-Level Simulations," *IEEE Transactions on Power Electronics*, vol. 33, no. 3, pp. 2471-2483, 2018.

[19] M. Luo, D. Dujic, and J. Allmeling, "Leakage Flux Modeling of Medium-Voltage Phase-Shift Transformers for System-Level Simulations," *IEEE Transactions on Power Electronics*, vol. 34, no. 3, pp. 2635-2654, 2019.

[20] G. R. Slemon, "Equivalent circuits for transformers and machines including non-linear effects," *Proceedings of the IEE - Part IV: Institution Monographs*, vol. 100, no. 5, pp. 129-143Available: https://digital-library.theiet.org/content/journals/10.1049/pi-4.1953.0015

[21] N. Chiesa, "Power transformer modeling for inrush current calculation," 2010.

[22] N. Bracikowski, "Multi-Physical modelling lumped models; application to a synchronous machine with permanent magnets for the sizing," Ph.D. Thesis, Ecole Centrale de Lille, 2012.

[23] P. P. Silvester and R. L. Ferrari, *Finite Elements for Electrical Engineers*, 3 ed. Cambridge: Cambridge University Press, 1996.

[24] V. Fachbereich, "Numerical Methods for Transient Field-Circuit Coupled Simulations Based on the Finite Integration Technique and a Mixed Circuit Formulation," 2007.

[25] S. Dennetière, Y. Guillot, J. Mahseredjian, and M. Rioual, "A link between EMTP-RV and FLUX3D for transformer energization studies," *Electric Power Systems Research*, vol. 79, no. 3, pp. 498-503, 2009/03/01/ 2009.

[26] V. Ostovic, *Dynamics of saturated electric machines*. New York, NY: Springer, 2012, pp. XIII, 445.

[27] J. Cale, S. D. Sudhoff, and T. Li-Quan, "Accurately modeling EI core inductors using a high-fidelity magnetic equivalent circuit approach," *IEEE Transactions on Magnetics*, vol. 42, no. 1, pp. 40-46, 2006.

[28] S. Jazebi and F. d. León, "Experimentally Validated Reversible Single-Phase Multiwinding Transformer Model for the Accurate Calculation of Low-Frequency Transients," *IEEE Transactions on Power Delivery*, vol. 30, no. 1, pp. 193-201, 2015.

[29] S. Jazebi and F. d. León, "Duality-Based Transformer Model Including Eddy Current Effects in the Windings," *IEEE Transactions on Power Delivery*, vol. 30, no. 5, pp. 2312-2320, 2015.

[30] S. Jazebi, F. d. León, A. Farazmand, and D. Deswal, "Dual Reversible Transformer Model for the Calculation of Low-Frequency Transients," *IEEE Transactions on Power Delivery*, vol. 28, no. 4, pp. 2509-2517, 2013.

[31] C. Alvarez-Marino, F. d. Leon, and X. M. Lopez-Fernandez, "Equivalent Circuit for the Leakage Inductance of Multiwinding Transformers: Unification of Terminal and Duality Models," *IEEE Transactions on Power Delivery*, vol. 27, no. 1, pp. 353-361, 2012.

[32] J. A. Martinez-Velasco, *Power system transients: parameter determination*. Boca Raton: CRC press, 2017.

[33] F. d. Leon and J. A. Martinez, "Dual Three-Winding Transformer Equivalent Circuit Matching Leakage Measurements," *IEEE Transactions on Power Delivery,* vol. 24, no. 1, pp. 160-168, 2009.

[34] J. Mahseredjian, S. Dennetière, L. Dubé, B. Khodabakhchian, and L. Gérin-Lajoie, "On a new approach for the simulation of transients in power systems," *Electric Power Systems Research*, vol. 77, no. 11, pp. 1514-1520, 2007/09/01/ 2007.

[35] H. W. Dommel, *Electromagnetic Transients Program Reference Manual:(EMTP) Theory Book*. Bonneville Power Administration, 1986.

[36] C. Xusheng, "Negative inductance and numerical instability of the Saturable Transformer Component in EMTP," *IEEE Transactions on Power Delivery,* vol. 15, no. 4, pp. 1199-1204, 2000.

[37] J. A. Martinez and B. A. Mork, "Transformer modeling for low- and mid-frequency transients - a review," *IEEE Transactions on Power Delivery,* vol. 20, no. 2, pp. 1625-1632, 2005.

[38] T. Henriksen, "How to avoid unstable time domain responses caused by transformer models," *IEEE Transactions on Power Delivery,* vol. 17, no. 2, pp. 516-522, 2002.

[39] V. Brandwajn, H. W. Donnel, and I. I. Dommel, "Matrix Representation of Three-Phase N-Winding Transformers for Steady-State and Transient Studies," *IEEE Transactions on Power Apparatus and Systems,* vol. PAS-101, no. 6, pp. 1369-1378, 1982.

[40] W. G. Enright, "Transformer models for electromagnetic transient studies with particular reference to HVdc transmission," Doctor of Philosophy, University of Canterbury, Christchurch, New Zealand, 1996.

[41] W. Enright, O. Nayak, G. Irwin, and J. Arrillaga, "An electromagnetic transients model of multi-limb transformers using normalized core concept," in *IPST'97-International Conference on Power System Transients*, 1997, pp. 93-98.

[42] W. Enright, "Transformer models for electromagnetic transient studies with particular reference to HVdc transmission," 1996.

[43] F. Gonzalez-Molina, D. Ishchenko, and B. Mork, "Parameter estimation and advancements in transformer models for EMTP simulations, MTU6: Parameter Estimation," USA: Bonneville Power Administration.2003.

[44] B. A. Mork, F. Gonzalez, D. Ishchenko, D. L. Stuehm, and J. Mitra, "Hybrid Transformer Model for Transient Simulation—Part I: Development and Parameters," *IEEE Transactions on Power Delivery,* vol. 22, no. 1, pp. 248-255, 2007.

[45] B. A. Mork, F. Gonzalez, D. Ishchenko, D. L. Stuehm, and J. Mitra, "Hybrid Transformer Model for Transient Simulation—Part II: Laboratory Measurements and Benchmarking," *IEEE Transactions on Power Delivery,* vol. 22, no. 1, pp. 256-262, 2007.

[46] J. A. Martinez, R. Walling, B. A. Mork, J. Martin-Arnedo, and D. Durbak, "Parameter determination for modeling system transients-Part III: Transformers," *IEEE Transactions on Power Delivery,* vol. 20, no. 3, pp. 2051-2062, 2005.

[47] F. d. Leon and A. Semlyen, "Complete transformer model for electromagnetic transients," *IEEE Transactions on Power Delivery,* vol. 9, no. 1, pp. 231-239, 1994.

[48] A. Narang and R. H. Brierley, "Topology based magnetic model for steady-state and transient studies for three-phase core type transformers," *IEEE Transactions on Power Systems,* vol. 9, no. 3, pp. 1337-1349, 1994.

[49] C. M. Arturi, "Transient simulation and analysis of a three-phase five-limb step-up transformer following an out-of-phase synchronization," *IEEE Transactions on Power Delivery,* vol. 6, no. 1, pp. 196-207, 1991.

[50] C. Xusheng, "A three-phase multi-legged transformer model in ATP using the directly-formed inverse inductance matrix," *IEEE Transactions on Power Delivery,* vol. 11, no. 3, pp. 1554-1562, 1996.

[51] B. A. Mork, "Five-legged wound-core transformer model: derivation, parameters, implementation and evaluation," *IEEE Transactions on Power Delivery,* vol. 14, no. 4, pp. 1519-1526, 1999.

[52] N. Chiesa, B. A. Mork, and H. K. Høidalen, "Transformer Model for Inrush Current Calculations: Simulations, Measurements and Sensitivity Analysis," *IEEE Transactions on Power Delivery,* vol. 25, no. 4, pp. 2599-2608, 2010.

[53] A. Rezaei-Zare, "Enhanced Transformer Model for Low- and Mid-Frequency Transients—Part I: Model Development," *IEEE Transactions on Power Delivery,* vol. 30, no. 1, pp. 307-315, 2015.

[54] A. Rezaei-Zare, "Enhanced Transformer Model for Low- and Mid-Frequency Transients—Part II: Validation and Simulation Results," *IEEE Transactions on Power Delivery,* vol. 30, no. 1, pp. 316-325, 2015.

[55] S. E. Zirka, Y. I. Moroz, C. M. Arturi, N. Chiesa, and H. K. Hoidalen, "Topology-Correct Reversible Transformer Model," *IEEE Transactions on Power Delivery,* vol. 27, no. 4, pp. 2037-2045, 2012.

[56] S. Jazebi *et al.*, "Duality-Derived Transformer Models for Low-Frequency Electromagnetic Transients—Part II: Complementary Modeling Guidelines," *IEEE Transactions on Power Delivery,* vol. 31, no. 5, pp. 2420-2430, 2016.

[57] S. Jazebi *et al.*, "Duality Derived Transformer Models for Low-Frequency Electromagnetic Transients—Part I: Topological Models," *IEEE Transactions on Power Delivery,* vol. 31, no. 5, pp. 2410-2419, 2016.

[58] H. K. Høidalen, B. A. Mork, F. Gonzalez, D. Ishchenko, and N. Chiesa, "Implementation and verification of the Hybrid Transformer model in ATPDraw," *Electric Power Systems Research*, vol. 79, no. 3, pp. 454-459, 2009/03/01/ 2009.

[59] F. De Leon, "Transformer model for the study of electromagnetic transients," Ph.D. dissertation, Univ. Toronto, Toronto, ON, 1993.

[60] F. d. Leon and A. Semlyen, "Reduced order model for transformer transients," *IEEE Transactions on Power Delivery,* vol. 7, no. 1, pp. 361-369, 1992.

[61] F. d. Leon and A. Semlyen, "Efficient calculation of elementary parameters of transformers," *IEEE Transactions on Power Delivery,* vol. 7, no. 1, pp. 376-383, 1992.

[62] F. d. Leon and A. Semlyen, "Time domain modeling of eddy current effects for transformer transients," *IEEE Transactions on Power Delivery,* vol. 8, no. 1, pp. 271-280, 1993.

[63] J. Turowski, M. Turowski, and M. Kopec, "Method of three-dimensional network solution of leakage field of three-phase transformers," *IEEE Transactions on Magnetics,* vol. 26, no. 5, pp. 2911-2919, 1990.

[64] K. Pawluk, R. Sikora, R. L. Stoll, J. Sykulski, J. Turowski, and K. Zakrzewski, *Computational magnetics*. Chapman and Hall, London, UK, 1995.

[65] X. Lopez, C. Alvarez, P. Penabad, and J. Turowski, "RNM2D_0 Fast stray losses hazard evaluation on transformer tank wall and cover due to zero sequence," in *ARWtr2010 – 3rd International Advanced Research Workshop on Transformers,* Spain, 2010, pp. 338-343.

[66] J. Turowski, "Fast computation of coupled fields in complex, 3-D, industrial electromagnetic structures," *COMPEL - The international journal for computation and mathematics in electrical and electronic engineering,* vol. 17, no. 4, pp. 489-505, 1998.

[67] M. Naïdjate, N. Bracikowski, M. Hecquet, M. Fratila, M. M. Duro, and J. P. Ducreux, "An intelligent reluctance network model for the study of large power and distribution transformers," in *2019 6th International Advanced Research Workshop on Transformers (ARWtr),* 2019, pp. 89-92.

[68] A. H. D. Cheng and D. T. Cheng, "Heritage and early history of the boundary element method," *Engineering Analysis with Boundary Elements,* vol. 29, no. 3, pp. 268-302, 2005/03/01/ 2005.

[69] H. Whitney, "Non-separable and planar graphs," in *Hassler Whitney Collected Papers*: Springer, 1992, pp. 37-59.

[70] M. Soleimani, J. Faiz, P. S. Nasab, and M. Moallem, "Temperature Measuring-Based Decision-Making Prognostic Approach in Electric Power Transformers Winding Failures," *IEEE Transactions on Instrumentation and Measurement,* vol. 69, no. 9, pp. 6995-7003, 2020.

[71] M. Lambert, M. Martínez-Duró, J. Mahseredjian, F. d. León, and F. Sirois, "Transformer Leakage Flux Models for Electromagnetic Transients: Critical Review and Validation of a New Model," *IEEE Transactions on Power Delivery,* vol. 29, no. 5, pp. 2180-2188, 2014.

[72] X. Margueron, A. Besri, P. Jeannin, J. Keradec, and G. Parent, "Complete Analytical Calculation of Static Leakage Parameters: A Step Toward HF Transformer Optimization," *IEEE Transactions on Industry Applications,* vol. 46, no. 3, pp. 1055-1063, 2010.

[73] X. Margueron, J. Keradec, and D. Magot, "Analytical Calculation of Static Leakage Inductances of HF Transformers Using PEEC Formulas," *IEEE Transactions on Industry Applications,* vol. 43, no. 4, pp. 884-892, 2007.

[74] M. Akbari, A. Rezaei-Zare, M. A. M. Cheema, and T. Kalicki, "Air Gap Inductance Calculation for Transformer Transient Model," *IEEE Transactions on Power Delivery,* vol. 36, no. 1, pp. 492-494, 2021.

[75] A. Lotfi, H. K. Hoidalen, N. Chiesa, and E. Rahimpour, "Calculation of off-core inductance in dual-circuit model of transformer," in *2014 Power Systems Computation Conference,* 2014, pp. 1-7.

[76] L. M. R. Oliveira and A. J. M. Cardoso, "Leakage Inductances Calculation for Power Transformers Interturn Fault Studies," *IEEE Transactions on Power Delivery*, vol. 30, no. 3, pp. 1213-1220, 2015.

[77] A. Avendaño, B. Mork, and H. Høidalen, "Transformer internal fault modeling in ATP," in *Int. Conf. Power Systems Transients*, 2011.

[78] R. Schlesinger and J. Biela, "Comparison of Analytical Models of Transformer Leakage Inductance: Accuracy Versus Computational Effort," *IEEE Transactions on Power Electronics*, vol. 36, no. 1, pp. 146-156, 2021.

[79] R. Schlesinger and J. Biela, "Comparison of Analytical Transformer Leakage Inductance Models: Accuracy vs. Computational Effort," in *2019 21st European Conference on Power Electronics and Applications (EPE '19 ECCE Europe)*, 2019, pp. P.1-P.10.

[80] R. Prieto, J. A. Cobos, O. Garcia, P. Alou, and J. Uceda, "Model of integrated magnetics by means of "double 2D" finite element analysis techniques," in *30th Annual IEEE Power Electronics Specialists Conference. Record. (Cat. No.99CH36321)*, 1999, vol. 1, pp. 598-603 vol.1.

[81] M. Eslamian, M. Kharezy, and T. Thiringer, "Calculation of the Leakage Inductance of Medium Frequency Transformers with Rectangular-Shaped Windings using an Accurate Analytical Method," in *2019 21st European Conference on Power Electronics and Applications (EPE '19 ECCE Europe)*, 2019, pp. P.1-P.10.

[82] A. Fouineau, M. Raulet, B. Lefebvre, N. Burais, and F. Sixdenier, "Semi-Analytical Methods for Calculation of Leakage Inductance and Frequency-Dependent Resistance of Windings in Transformers," *IEEE Transactions on Magnetics*, vol. 54, no. 10, pp. 1-10, 2018.

[83] M. Mogorovic and D. Dujic, "100 kW, 10 kHz Medium-Frequency Transformer Design Optimization and Experimental Verification," *IEEE Transactions on Power Electronics*, vol. 34, no. 2, pp. 1696-1708, 2019.

[84] A. F. Hoke and C. R. Sullivan, "An improved two-dimensional numerical modeling method for E-core transformers," in *APEC. Seventeenth Annual IEEE Applied Power Electronics Conference and Exposition (Cat. No.02CH37335)*, 2002, vol. 1, pp. 151-157 vol.1.

[85] R. Prieto, J. A. Cobos, O. Garcia, P. Alou, and J. Uceda, "Study of 3-D magnetic components by means of "double 2-D" methodology," *IEEE Transactions on Industrial Electronics*, vol. 50, no. 1, pp. 183-192, 2003.

[86] G. Kapp, *Transformatoren für Wechselstrom und Drehstrom*, 3rd ed. Berlin, Heidelberg: Springer, 1907, pp. VII, 328.

[87] W. Rogowski, "Ueber das Streufeld und den Streuinduktionskoeffizienten eines Transformators mit Scheibenwicklung und geteilten Endspulen: Die Aenderung der Umlaufzahl und des Wirkungsgrades von Schiffschrauben mit der Fahrgeschwindigkeit," Ph.D. dissertation, Technische Hochschule zu Danzig, Danzig, Berlin, 1908.

[88] E. Roth, "Étude analytique du champ de fuites des transformateurs et des efforts mécaniques exercés sur les enroulements," *Revue générale de l'électricité,* vol. 23, pp. 773-787, 1928.

[89] A. Boyajian, "Leakage Reactance of Irregular Distributions of Transformer Windings by the Method of Double Fourier Series [includes discussion]," *Transactions of the American Institute of Electrical Engineers. Part III: Power Apparatus and Systems*, vol. 73, no. 2, pp. 1078-1086, 1954.